Ocean-air N_2O trace gas fluxes in Halifax Harbour derived from Open-Path FTIR measurements

By

Martin Hellmich

A Thesis Submitted to

Saint Mary's University, Halifax, Nova Scotia

in Partial Fulfillment of the Requirements for

the Degree of Master of Science in Applied Science.

August 2022, Halifax, Nova Scotia

Approved: Dr. Aldona Wiacek

Supervisor

Approved: Dr. Thomas Flesch

Committee Member

Approved: Dr. Danika Van Proosdij

Committee Member

Approved: Dr. Brent Else

External Examiner

Date: August 30, 2022

Ocean-air N_2O trace gas fluxes in Halifax Harbour derived from Open-Path FTIR measurements

By Martin Hellmich

Abstract

Open-Path Fourier Transform Infrared (OP-FTIR) spectroscopy is an established technique for path-average measurements of atmospheric trace gas concentrations. We describe the novel application of OP-FTIR to measure ocean-air gas fluxes across 586 m of Halifax Harbour (northwest Atlantic coast), also using a 3-D sonic anemometer and two vertically separated retroreflector arrays. We present spectroscopic retrievals of nitrous oxide (N_2O) concentration, micrometeorological data characteristics, and flux-gradient method calculations of ocean-air N_2O flux. From Dec. 2020 to Apr. 2021 the calculated ocean sink of $-10.81\ \mathrm{kg_{N_2O}ha^{-1}}$ agreed broadly with a global model of thermal (solubility-driven) N_2O flux. A powerful short-term ocean source event observed on Dec. 15-17 ($+2.00\ \mathrm{kg_{N_2O}ha^{-1}}$) correlated with high winds and strong ocean cooling that plausibly caused surface overturning and the upwelling of N_2O-rich deeper waters. The method presented is well suited to high frequency monitoring of coastal N_2O fluxes, necessary to resolve complex physical, chemical and biological processes.

August 30, 2022

Acknowledgments

Thank you to my family for support and sacrifices that allowed me to complete this work.

Thank you to the WARG research team for ongoing mentorship and support: Dr. Aldona Wiacek (Supervisor), Cameron Power (BSc), Dr. Ian Ashpole, Morgan Mitchell (BSc, MSc), Kyle Yeates (BSc) and Kagan Akiyama.

Thank you to the committee members Dr. Thomas Flesch and Dr. Danika Van Proosdij, and the external examiner Dr. Brent Else for guidance and inspiration.

Thank you to CFB Halifax for access to the DND Dockyards measurement location and generous on-site support.

Thank you to Dr. David Risk, Chelsie Hall (PMP), Mark Argento (MSc), and the Flux Lab team at Saint Francis Xavier University for loaning the 3-D sonic anemometer used in this study.

Thank you to Dr. David Wallace and Adriana Reitano (BSc) for useful discussion and advice on oceanographic processes and Bedford Basin ocean-side measurements.

Thank you to Jessica Morena, the Bedford Institute of Oceanography and the Canadian Hydrographic Service for access to high resolution tidal data.

Thank you to Tom King, Mike Campbell, and the METeorology and Oceanography Centre (METOC) Halifax for access to Halifax Harbour weather station data.

Thank you to Dr. Li for previous contributions to N_2O retrieval parameters for the OP-FTIR instrument and MATLAB scripting for retrieval processing.

Thank you to Campbell Scientific Support for help with customizing the CRBASIC code.

Table of contents

1. Introduction

1.1. N_2O and the environment

1.1.1. N_2O emissions and climate change

Due to an increasing concentration of greenhouse gases (GHG's) the earth has been in radiative imbalance, with global heat content increasing since 1970 (Allen et al., 2014). Present day concentrations of carbon dioxide (CO_2), methane (CH_4), and nitrous oxide (N_2O) are greater than the past 800,000 years of measurements based on ice cores analysis (Allen et al., 2014). Atmospheric GHG and trace gas composition is influenced by biological, anthropogenic and physical mechanisms. People cause emissions through industrial, agricultural and transportation activities. Changes in atmospheric composition and global heat content affect biogeochemical cycles. Our understanding of the feedbacks between climate and biogeochemical cycles has large uncertainties, driven both by a lack of observations and by incomplete process knowledge. More local measurements can uncover detailed mechanisms that give us a better understanding of the interconnection between systems.

N_2O is the third most potent greenhouse gas but has not been studied as thoroughly as CO_2 and CH_4. N_2O is a long-lived greenhouse gas emitted by human activities such as fertilizer use and fossil fuel burning as well as natural process in soils and oceans. N_2O only accounts for around 0.03 per cent of total GHG emissions by concentration (IPCC, 2007). Given its lifetime and radiative efficiency the global warming potential of N_2O is 300 times that of CO_2 (IPCC, 2007). The impact of individual GHGs on global warming can be expressed in CO_2 equivalents, which is when N_2O accounts for approximately 10 per cent of total emissions (Bates et al., 2008). The atmospheric lifetime of N_2O is 114 years with the main sink being stratospheric processes.

The ocean and coastal ecosystems are thought to play an important role in global budgets of atmospheric N_2O. The magnitude of surface to air emissions are estimated at 18 Tg N_2O yr^{-1} with a large uncertainty of 8-31 Tg N_2O yr^{-1}, of which 4 [2-9] Tg N_2O yr^{-1} is from the ocean (IPCC, 2013). Approximately 62% of total global N_2O emissions are emitted from natural and agricultural soils (Thomson et al., 2012). A third of N_2O emissions comes from the ocean via nitrification and denitrification (Bange et al., 2010), making the ocean the second largest source of N_2O. In the ocean N_2O is involved in many biological, chemical and physical interactions which affect its flux to and from the atmosphere. These complex interactions make N_2O transfer hard to predict and lead to uncertainties in climate models. Regular emissions monitoring in a variety of environments

around the world could improve predictions of global budgets when measurements are incorporated into models. This work explores a new measurement technique that could increase the accessibility of emission monitoring in coastal areas.

Oceanic N_2O emissions affect and are affected by various biogenic cycles. For example, N_2O production in the ocean depends on microbial decay of organic matter which depends on oxygen content. High N_2O productive regions are associated with low oxygen waters, and these regions have been expanding over the last 50 years (Arévalo-Martínez et al., 2019). This will have an impact on the production of N_2O, and the resulting effect on N_2O emissions should be monitored. How oceanic N_2O emissions will evolve is unclear since mechanisms such as denitrification are not fully understood and are highly heterogenous (Freing et al., 2012; Thomson et al., 2012). Many processes are not yet represented in climate-biogeochemistry models. For processes that are represented, the nonlinear interactions are not well quantified. More emission measurement data is needed to resolve N_2O sources and sinks which may vary spatially and temporally. Therefore, additional local monitoring of N_2O will give insights into these biological mechanisms and as a result put better constraints on climate models.

An example of changing physical processes affecting N_2O emissions is ocean warming. The estimated global heating rate between 1971 and 2010 was 213×10^{12} W annually. Ocean warming accounts for about 93% of that total (Allen et al., 2014). Ocean warming might result in changes in the bacterial community which produces N_2O (Thomson et al., 2012). Increases in ocean temperature decrease the solubility of N_2O. As a result the storage capacity of N_2O in the ocean is most likely being reduced (Thomson et al., 2012). Temperature change may also affect the path of currents, changing the location and size of upwelling and downwelling regions (Capone & Hutchins, 2013). The processes behind oceanic N_2O sources are likely to vary as the ocean environment changes. To track these changes long term continuous measurements are needed.

1.1.2. N_2O sources in coastal ecosystems

Coastal regions have recently been shown to be disproportionately significant to global N_2O emissions given the small surface area they cover. Emission models of N_2O underestimate the quantity of N_2O ocean-air exchange in coastal regions (Freing et al., 2012; Arévalo-Martínez et al., 2019). Coastal regions and estuaries account for 10% of anthropogenic and 60% oceanic N_2O emissions to the atmosphere (IPCC, 2013). Coastal ecosystems also help mitigate the impact of coastal erosion and flooding (Cao et al., 2018), and coastal ecosystems such as mangroves,

seagrass, and salt marshes are strong carbon sinks (McLeod et al., 2011). These systems are at the interface between land, ocean and atmosphere. They are sensitive to environmental influences such as fertilizer run-off from land, upwelling currents from the deep ocean, and the ocean-atmosphere interface conditions. The conditions affecting coastal waters vary greatly depending on location requiring dense measurement networks. While continental shelf areas account for a negligible fraction of N_2O emissions, coastal regions such as estuaries, river plumes and upwelling zones are significant sources (Freing et al., 2012; Thomson et al., 2012). Emission models may have underestimated the potential of coastal regions due to data scarcity (Arévalo-Martínez et al., 2019). Further survey and continual monitoring of N_2O emissions in a variety of coastal environments will no doubt lead to refinements of emission models through higher resolution measurements and better understanding of processes.

Coastal ecosystems, due to their interface with land, deep ocean and atmosphere have multiple sources of organic matter which means the average ocean composition is perturbed. There are uncertainties in how the nitrogen cycle is affected by anthropogenic sources such as pollution from fossil fuel combustion and run-off of artificial fertilizers (Voss et al., 2013). It is clear that the natural amount of nitrogen entering coastal waters is being enhanced (Diaz & Rosenberg, 2008). For example, a large fraction of nitrogen in estuaries comes from sedimentary sources. Estuaries are fertilized to an increasing degree by river run-off carrying high amounts of organic nitrogen (Freing et al., 2012). Fertilizer run-off leads to increased production and oxygen depleted areas in coastal waters. Unlike in the open ocean the shallow depths of coastal regions allow for N_2O produced in the sediments to reach the atmosphere (Freing et al., 2012). Our impact on N_2O emissions through these interactions has not been measured for many coastal settlements, estuaries or river mouths.

The changes humans have made to the ocean environment are starting to emerge in coastal areas. Feedback effects from seemingly unrelated changes could start to cause changes in N_2O emissions. For example, increasing atmospheric CO_2 is changing ocean chemistry in a way that could increase N_2O emissions. The ocean is becoming more acidic from CO_2 directly and more stratified due to heating, leading to reduced oxygen content in the water (Capone & Hutchins, 2013). Microbial processes such as nitrification and denitrification that produce N_2O are increased by low oxygen levels and increasing ocean acidity (Capone & Hutchins, 2013). Improving

understanding of how GHG's interact in coastal environments is important for predicting secondary effects and decisions regarding climate change mitigation strategies.

1.1.3. Ocean-air Flux of N_2O

This work has produced novel N_2O ocean-air flux data for the coastal location of Halifax Harbour. Flux measurements can be influenced by physical, chemical or biological processes (Wanninkhof et al., 2009). Flux measurements can be used to characterize emission sources and sinks. Identification of negative fluxes (the ocean is a sink for atmospheric N_2O) or positive fluxes (the ocean is a source of atmospheric N_2O) as well as the seasonal rate of change can be directly compared to the global biogeochemical models that predict GHG budgets. Satellite technology is improving to give better space-based measurements, like the MIN2OS project that will fly in 2032 and will provide emission estimates of N_2O on a 10 x 10km^2 scale (Ricaud et al., 2021). Ground based measurement will be important to provide finer scale measurements, calibrate biases in satellite measurements and investigate sources within the satellite footprint. Only a few such measurements have been carried out for N_2O, especially in coastal areas.

Surface based ocean-air flux measurements of N_2O have involved vertical profiling of the ocean surface layer. This had been used in conjunction with atmospheric concentrations and ocean biogeochemical modelling to extrapolate globally from limited measurements. Some of the largest measurement campaigns consist of periodic samples from research vessels on cruise tracks spanning the north and south hemispheres in the Atlantic and Pacific. Figure 1-1 shows the sample points from two research vessel expeditions in the Atlantic (Forster et al., 2009). Similar expeditions have recently been completed in the Pacific (Zhan et al., 2017). These have provided a foundation for how oceanic N_2O flux might vary with latitude. In general, in the northern hemisphere positive N_2O fluxes were observed with some exceptions, so N_2O is emitted from the ocean to the atmosphere. The magnitude of the flux tends to decrease with latitude, though it is hard to be sure as the measurements are collected at different times over the course of two months for each expedition. A single point measurement does not characterize the sources of the flux well. For example, extensive subsurface production at (100-500m depth) may not coincide with areas of large fluxes because of the effects of advection (Freing et al., 2012). There are too few measurements to account for all variables such as seasonal variation, wind and currents (Zhan et al., 2017). Long term continuous observation in specific locations of interest, such as a harbour,

could help compensate for the weaknesses of the cruise type observations by measuring the temporal variability of N_2O fluxes.

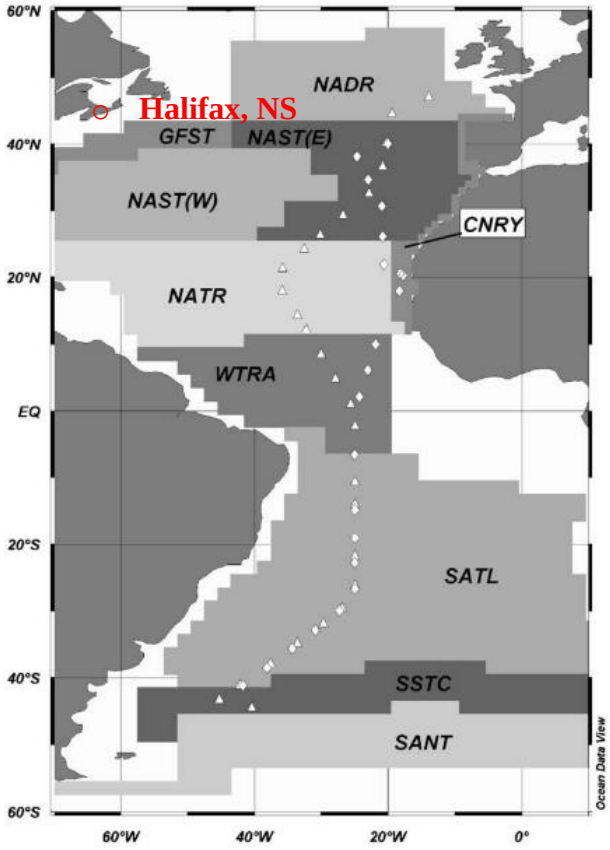

Figure 1-1: Modified from Forster et al. (2009). Halifax (red circle) in relation to a previous cruise track measuring N_2O flux. N_2O flux sample points from research expeditions AMT12 and AMT13 in 2003.

In addition to cruise tracks there have recently been notable measurements in coastal areas in India and in Maryland USA (Hershey et al., 2019; Laperriere et al., 2019). In Chesapeake Bay a research vessel mounted ocean surface layer profiling method was used to measure N_2O flux. The physical processes in the Bay have been shown to affect production of N_2O making the Bay a highly variable source (into atmosphere) of N_2O (Laperriere et al., 2019). Both the studies in Chesapeake Bay, US and to a greater extent in the Cochin estuary, India found large variation in N_2O flux depending on location. In Cochin estuary N_2O flux was higher in locations with increased organic matter due to anthropogenic disturbances (Hershey et al., 2019). Our current understanding is limited by sparse sampling with too few measurement locations being observed in the open ocean and in heterogenous coastal areas. Bedford Basin in Halifax has been identified as an ideal location for campaigns to understand environmental processes concerning ocean-air flux and to

improve representation in models (Shi & Wallace, 2018). Our project has provided an additional observation location to further elucidate the drivers of N_2O flux on the Atlantic coast.

While the ocean is a net source of N_2O emissions, variable environmental conditions can result in areas acting as sinks for parts of the year. A biogeochemical model has been developed utilizing measurements to parameterize the prediction of total fluxes on a global scale (Manizza et al., 2012). Figure 1-2 shows a world map of annual mean N_2O flux from that study. Their model combines an ocean circulation model with a biogeochemical module that represents the full cycles of O_2 and N_2O. Also included are thermal mixing, solubility changes, ventilation from subsurface mixing and biological production. It can be seen from the figure that North America's eastern coast is an area of N_2O emission from the ocean. The accuracy of models like this could be improved with more local measurements that capture the processes in unique areas and during seasonal changes. For example, hurricane season could be an important factor to consider for the Northwest Atlantic. When tropical cyclone Hudhud made landfall in 2014 in India, analysis of waters on the east coast of India showed that the ocean changed from a source of N_2O before the storm to a sink which lasted for weeks post-storm (Kumari et al., 2019). Different locations could have unexpected responses to seasonal variation, anthropogenic forcing and weather patterns. Local flux measurements can provide the detail needed to identify and quantify sources and to parameterize the processes that modify them.

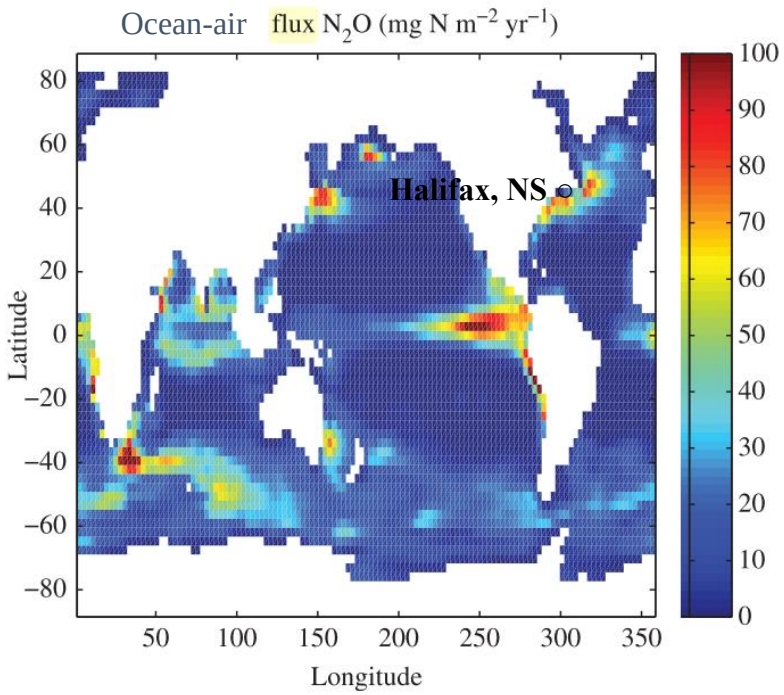

Figure 1-2: Modified from Manizza et al. (2012). Halifax location (black circle) in comparison to the annual mean of modelled N_2O flux from the global ocean. Positive values are sources, from the ocean to the atmosphere.

1.1.4. Frequency and scale of observable processes

Figure 3 is a useful diagram for understanding and contextualizing this project's N_2O flux measurements in Halifax Harbour in relation to possible underlying processes. The figure is modified from Wilson et al. (2020) and shows the spatial and temporal scales of physical, biological, and climatological processes that could be influencing our measurements on the spatial scale of 500 meters, based on the approximate size of the OP-FTIR measurement footprint. Wind and concentration observations are made on 1- and 4-minute intervals, respectively, which are then averaged over 30 minutes for flux calculations. Fluxes were observed for a period of 5 months, so any scale up to that could potentially be investigated. This suggests that processes in the "high resolution" coastal and shallow waters box could be observed, with groundwater discharge and inertial and solitary waves being closest to our spatial scale of 500 m. Moreover, with data for a longer period our measurements cross over into the "low resolution" box, where mesoscale phenomena and phytoplankton blooms could be observable. It could also be argued that the observations must also include some average result of processes on scales smaller than 500 m.

Likewise scales larger than our measurement will be present but under sampled and could result in an undetectable bias in the results when compared to other similar scale measurements at different locations or different times. This diagram helps illustrate the benefits of having a variety of methods to compare different scales and the flexibility that comes from continuous observations for longer periods. This is where open-path spectroscopy and flux gradient method could excel in a coastal environment as the geometry and continual operation is very feasible compared to research vessel-mounted instruments or sample collecting devices.

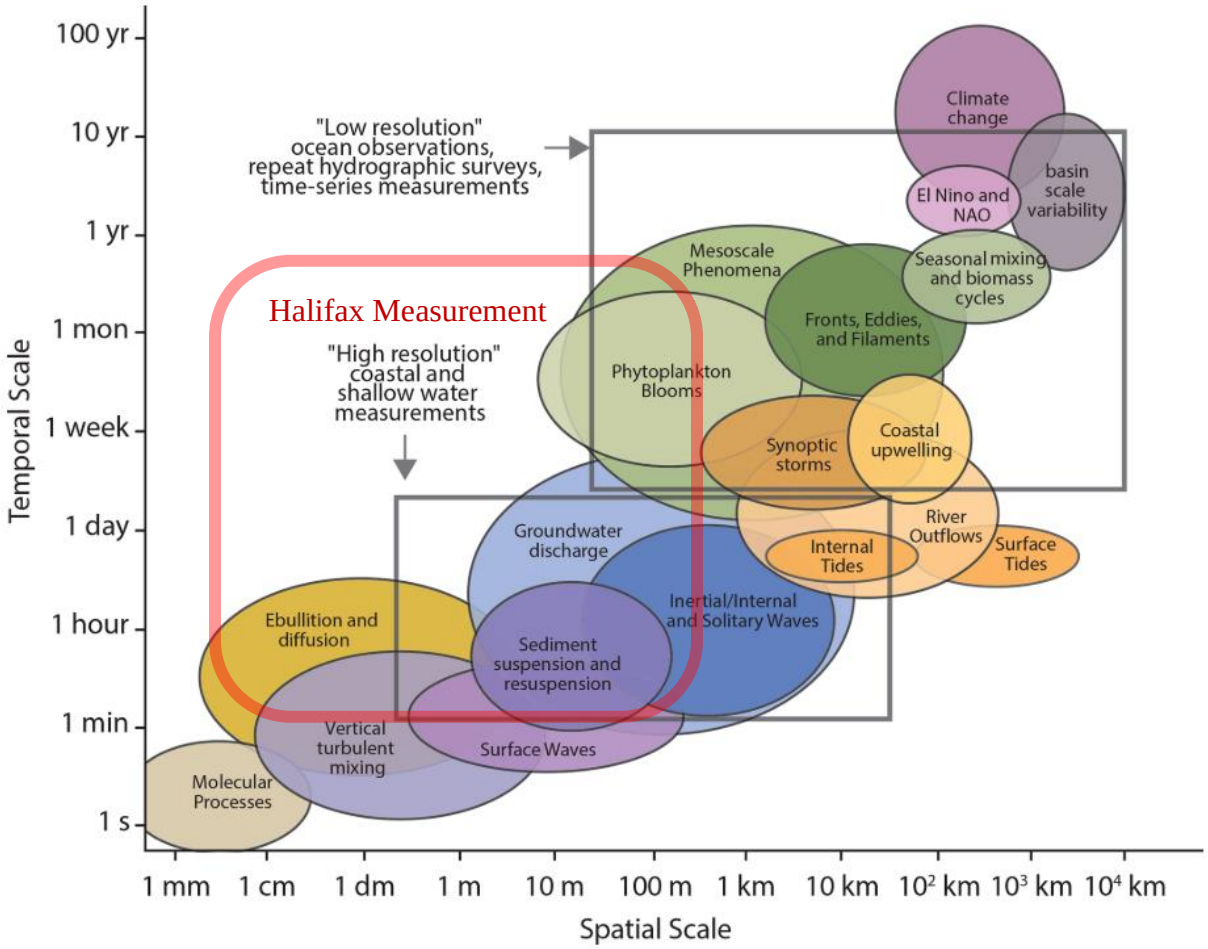

Figure 1-3: Modified from Wilson et al. (2020). Time-space scale diagram for various physical processes involving marine CH_4 and N_2O. Measurements in this work lie in the 1-minute to 5-month time range and the <500 m spatial scale (represented by the red box).

1.2. Overview of N_2O flux measurement methods

1.2.1. Previous flux measurement methods

Concentration surveys are often used to indicate source locations, i.e., locations having elevated gas concentrations (compared to other locations) are assumed to correlate to locations of high gas fluxes. An example of this is found in the use of drones with laser-based spectroscopy to survey the Arctic coastline (Oberle et al., 2019). This method was able to identify hot spots of gas concentration in the laser path below the drone flight track, which then identified likely gas fluxes. The hot spots corresponded to areas of coastal erosion and accelerated melting of permafrost, i.e., CH_4 production hotspots. Satellite observations have also been able to identify areas of elevated gas concentration while covering more ground than drones, but they are limited in spatial resolution and gas sensitivity (Oberle et al., 2019). Moreover, the whole air column is measured, making unambiguous surface attribution often impossible, and sources must be traced by also modelling transport in the atmosphere. These methods are complemented by vertical flux-gradient methods, as described in this project, which can observe the flux over time at locations of interest identified by a drone or a satellite survey.

Local ocean-air fluxes have typically been estimated by 1) measuring the vertical gradient of gas concentration in the water in combination with some model of gas transfer velocity across the ocean surface, i.e., the flux-gradient (FG) method, or by 2) measuring the vertical flux of gas in the atmosphere immediately above the water or shore from combined high-frequency point measurements of concentration and vertical wind speed, i.e., the eddy covariance (EC) technique (Wanninkhof et al., 2009). An example of FG method vertical profiling of dissolved N_2O concentrations in the ocean is described by Laperriere et al. (2019), where water samples were taken from 9 locations spanning 21 km x 6 km of Chesapeake Bay (northeast USA) at 3-4 depths ranging from the surface to 25 m. The samples were collected twice via research vessel, about two weeks apart (August and September 2013). N_2O flux was calculated using a flux-gradient method like what is used in this work except for requiring a treatment of gas diffusivity specific to these ocean-side measurements. The main advantage of our air-side method (Section 1.2.2) when compared to this vertical concentration profile method is that deployment into the ocean is not required, which removes many logistical considerations and allows more easily for long-term and continuous observations.

In the EC technique the measured flux corresponds to the ocean-air flux within a "footprint" upwind of the measurement. While eddy covariance has been used in Nova Scotia to measure ocean-air CO_2 flux as early as 1977 (Jones & Smith, 1977), its use for gases such as N_2O is limited by the lack of fast-response sensors for these species. The experiment setup is also a limiting factor for ocean-air flux as the equipment ideally needs to be over the source, whereas measurements can only be taken a short distance from shore or from a boat; the variable footprint of the equipment further complicates the use of this method in complex environments. One benefit of our method (Section 1.2.2) when compared to eddy covariance is the ability to have more control of the measured area with a larger and arguably more customizable footprint. The main benefit of our FG-based method over EC, however, is that the fast response of gas sensors is not required, and all FTIR-active gases can be measured together in principle, given the right signal conditions in practice.

1.2.2. Novel N_2O flux measurement method

This work applies an atmospheric concentration gradient method to measure the flux of N_2O above the water, which reflects the ocean-air flux underlying the measurement. The gas flux is calculated by combining measurements of the vertical gradient of gas concentration with wind and turbulence measurements in the atmospheric surface layer. A diagram summarizing the elements related to this measurement method is shown in Figure 1-4. Concentration is measured using Open Path Fourier Transform Infrared (OP-FTIR) spectroscopy, which measures path-average concentrations between an OP-FTIR source (and co-located detector) and a distant reflector (more details in Section 2.1). Two vertically separated concentrations (C_1, C_2) are measured at two heights (z_1, z_2) by aiming the OP-FTIR to reflectors at two heights. The gradient is proportional to the difference in concentration of these two paths and is used to calculate flux via the flux-gradient method,

$$\text{Flux} = -K\frac{C_2 - C_1}{z_2 - z_1},$$

where the constant K is a gas diffusivity that depends on wind speed and turbulence.

The foundation of the flux-gradient method is Monin-Obukhov Similarity Theory (MOST). This theory relates atmospheric fluxes to concentration gradients and wind statistics, through relatively simple, empirically derived functional forms from decades of theoretical research and field measurements (Chapter 11, Arya, 2001). This methodology for deriving fluxes in the surface

layer of the atmosphere is widely accepted, and the equations and instrument data used to calculate the flux are explained in detail in Section 2.3.

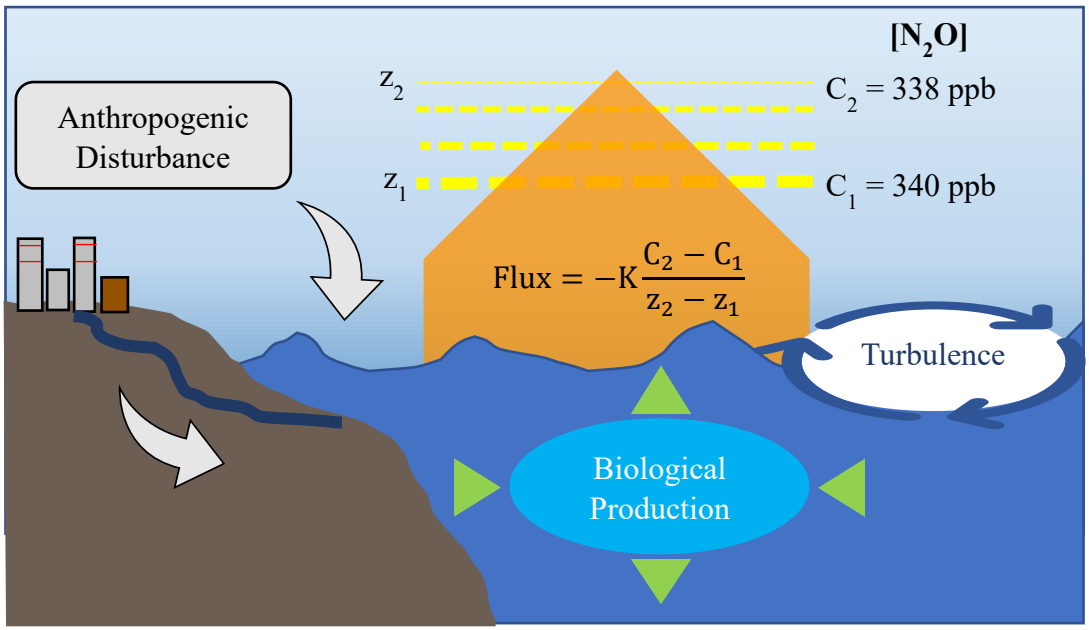

Figure 1-4: N_2O flux is found by measuring the vertical concentration gradient of the gas in the atmosphere. The constant K depends on meteorological factors, with the dominant factors being windspeed and turbulence. In this example lower concentrations at higher altitude correspond to flux out of the ocean and into the atmosphere.

1.2.2.1. Infrared spectroscopic N_2O concentration measurements

Open-Path Fourier Transform Infrared (OP-FTIR) spectroscopy is an established technique used to measure path-average atmospheric trace gas concentrations. It is useful for spanning over inaccessible areas, for example fence-line monitoring for refineries and factories or more recently to measure pollutant concentration changes due to shipping emissions from vessels passing through Halifax Harbor (Wiacek et al., 2018).

The OP-FTIR measurement method is used in this research to obtain the gas concentrations at two heights to find the concentration difference required to calculate flux. As mentioned previously, the high sensor response rate of EC methods is not required. Many molecules that interact with infrared light, including N_2O, are detectable simultaneously with FTIR spectroscopy (Wiacek et al., 2018). The open-path descriptor refers to the physical path along which spectral absorption measurements of actively emitted and transmitted IR light are made. A measurement path, see Figure 1-5 and Figure 1-6, unlike a measurement point, allows for the averaging of path-dependant environmental variables. Small variations in air-sea fluxes can cause variability in air concentrations, which complicate point measurement techniques (Wanninkhof, 1992). Our path-

average approach ensures that the N_2O flux over water is favoured over other factors such as rush hour traffic N_2O emissions that could overwhelm a point source measurement in an urban setting. Measurements in Halifax Harbour give a concentration average over the entire water surface producing a more representative sample. OP-FTIR works in most weather conditions, except during heavy rainfall or fog, which causes IR beam extinction. The experiment is setup on land to span over water, thus reducing the complications of making measurements on open water (see details in Section 2.1). The instruments can run continuously, which makes them ideal for time series measurements to capture short-term events and long-term evolution.

The OP-FTIR technique has been previously applied to derivations of trace gas emissions using a flux-gradient approach. Flesch et al. (2016) used this approach to simultaneously measure both N_2O and ammonia (NH_3) fluxes from cattle overwintering areas in Alberta, Canada. This work is the first application of the OP-FTIR flux-gradient technique to estimate ocean-air flux. Exploratory OP-FTIR vertical concentration gradient measurements were carried out by the Wiacek Atmospheric Research Group (WARG) in Halifax Harbour in 2018. These measurements included an upper and lower path in the atmosphere (Figure 1-7). The location of the setup, as was used in 2018, is shown in Figure 5 and 6, and this is also the location used for the main focus of this project in 2020-2021. While the exploratory 2018 measurements did not include a sonic anemometer, nearby 2-m and 10-m winds were used to make progress on an approximate quantification of flux from these 2018 data (Appendix B).

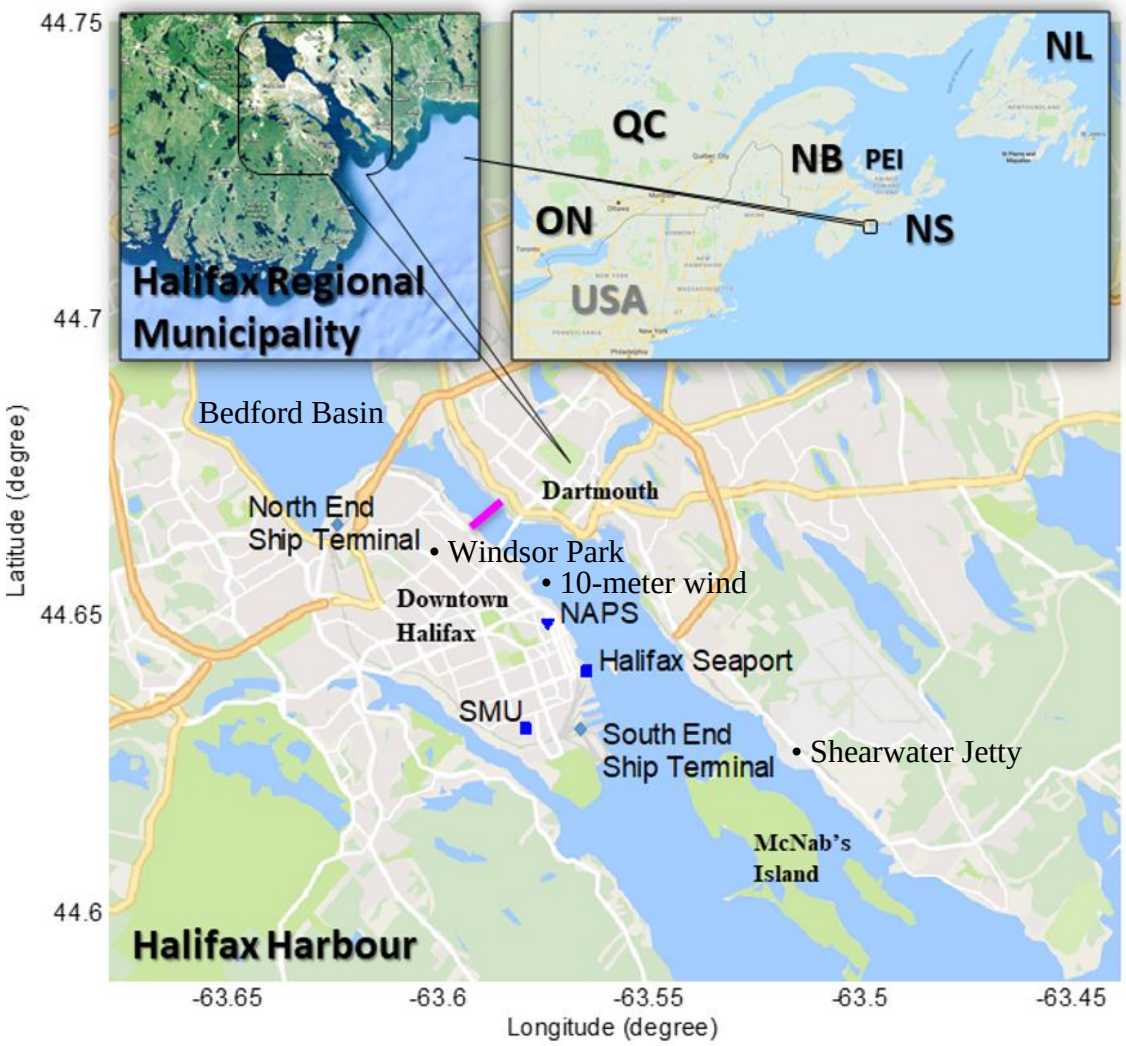

Figure 1-5: The measurement path location and length (magenta line) in Halifax Harbour, Nova Scotia. This was the location of both 2018 (no sonic) and 2020-2021 (sonic-instrumented) measurements. NAPS refers to a National Air Pollution Survey observation station.

Figure 1-6: The measurement path, looking across the harbour from the Halifax side towards Dartmouth, is 98% over the ocean surface.

Figures 5, 6, and 7 illustrate the experimental setup with the FTIR spectrometer on one side of the harbour (Halifax) and vertically separated retroreflectors on the other shore (Dartmouth). In summary, an IR beam makes a return trip between the spectrometer and alternating retroreflectors over the water of Halifax harbor (the detector is co-located with the IR source). The two-way path length of the IR beam is 1116 m. As it passes through the atmosphere, the energy spectrum of the beam captures the absorption signature of various gas molecules that make up the air, including N_2O. Gas concentrations were retrieved from the measured atmospheric absorption spectra using non-linear least squares fitting in MALT software (Griffith, 1996) and molecule spectroscopic data from the HITRAN database (Gordon et al., 2017). This setup allows measurements of gas concentrations at two average path heights, which is necessary for the flux-gradient approach.

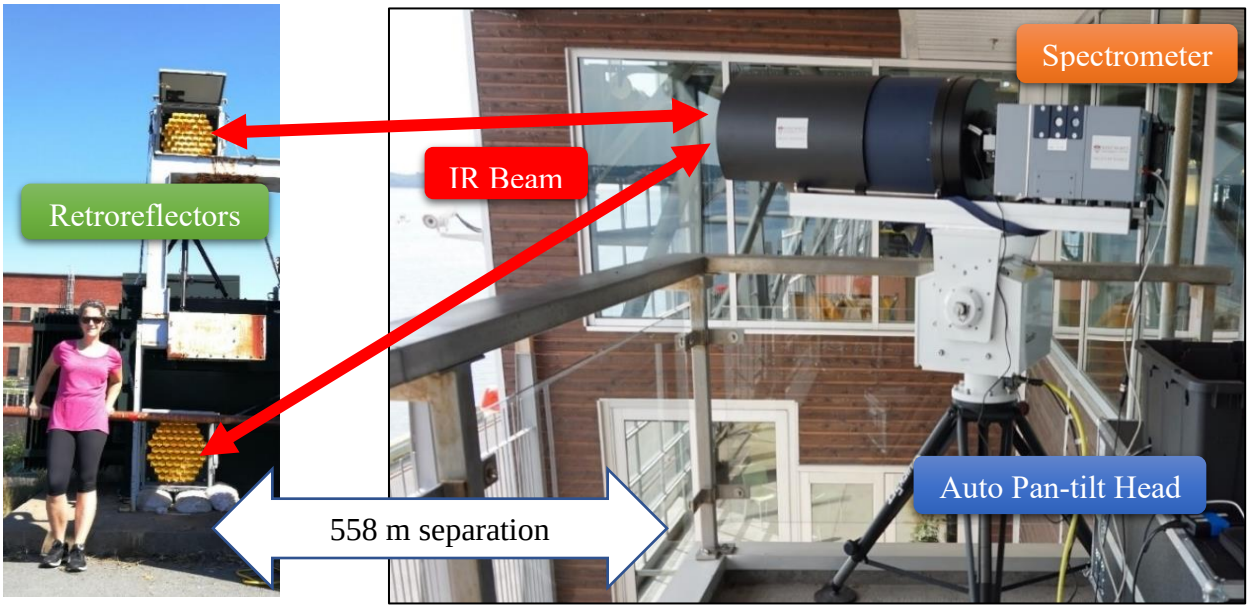

Figure 1-7: (Left) Two retroreflectors in a vertical configuration, with supervisor for scale. (Right) The OP-FTIR Spectrometer. These instruments are separated by the measurement path over water, which was 558 m (one way). The two-way absorption path length of the IR beam is thus 1116 m.

1.2.2.2. Sonic anemometer and micrometeorological theory

The flux-gradient method used to calculate N_2O fluxes is explained in chapter 2.3. Below is a summary of the relevant theory. A 3-D sonic anemometer uses pulsed acoustics and outputs wind speeds, Ux, Uy and Uz, and the sonic acoustic temperature, Ts. The covariance of the wind and temperature components provides the friction velocity (u*) and the Obukhov stability length, L (this measures the thermal stratification of the atmosphere). For the atmospheric surface layer the classic logarithmic wind profile is found from the similarity hypothesis that the velocity distribution, $\partial U/\partial z$ is only dependant on the height z above the surface, the surface drag, τ_0, and the fluid density, ρ (Arya, 2001). This leads to a logarithmic velocity profile law for neutrally buoyant conditions,

$$U(z) = \frac{u^*}{k_v} \ln\left(\frac{z}{z_0}\right).$$

z_0 is defined as the roughness length and is related to the surface roughness characteristics. k_v is the von Karman constant which is empirically derived. The characteristic velocity scale is defined as the friction velocity

$$u^* \equiv \left(\frac{\tau_0}{\rho}\right)^{\frac{1}{2}}.$$

Monin-Obukhov Similarity Theory (MOST) adds two additional variables to the similarity hypothesis described above. $\partial U/\partial z$ still depends on height z, with τ_0 and ρ, now represented as the kinematic momentum flux, $\frac{\tau_0}{\rho}$. Additionally $\partial U/\partial z$ must also depend on the kinematic heat flux ($\frac{H_0}{\rho C_p}$) and the buoyancy variable ($\frac{g}{T_0}$) (Arya, 2001). H_0 is the surface heat flux, C_p is the specific heat capacity of the atmosphere at constant pressure, T_0 is the temperature at the reference state, and g is the gravitational acceleration. This leads to the stability-corrected logarithmic velocity profile,

$$U(z) = \frac{u^*}{k_v}\left[\ln\left(\frac{z}{z_0}\right) - \psi_m\left(\frac{z}{L}\right)\right].$$

This is a modification of the log wind profile, adding an additional stability correction term, ψ_m , which is a correction for atmospheric stability (i.e., the vertical temperature stratification). The Obukhov Length, L, is a characteristic length scale which is interpreted as the height at which the production of turbulent kinetic energy from wind shear equals that due to buoyancy (Arya, 2001). It can be shown that its formula is:

$$L = \frac{-u_*^3}{k_v\left(\frac{g}{T_0}\right)\left(\frac{H_0}{\rho C_p}\right)} \qquad .$$

The magnitude of the dimensionless stability parameter $\frac{z}{L}$ indicates whether the production of turbulence is dominated by the effect of wind shear or by buoyancy. The stability parameter resulting from z << |L| (our case) means that turbulence production is dominated by wind shear. The sign of $\frac{z}{L}$ determines the status of that stability where positive $\frac{z}{L}$ represents stable conditions (e.g., stable nighttime conditions where turbulence is suppressed) and negative $\frac{z}{L}$ represents unstable conditions (e.g., light wind daytime conditions with enhanced turbulence). A near-zero $\frac{z}{L}$ corresponds to well-mixed windy or cloudy conditions with moderate levels of turbulence. The calculation of the MOST stability correction function, ψ_m, is left for detailed explanation starting from measured data in Section 2.3. In Section 2.3 the stability corrected logarithmic velocity profile as well as a temperature profile of similar form are used to calculate the flux via the flux-gradient method and to determine input temperatures for the spectroscopic retrievals.

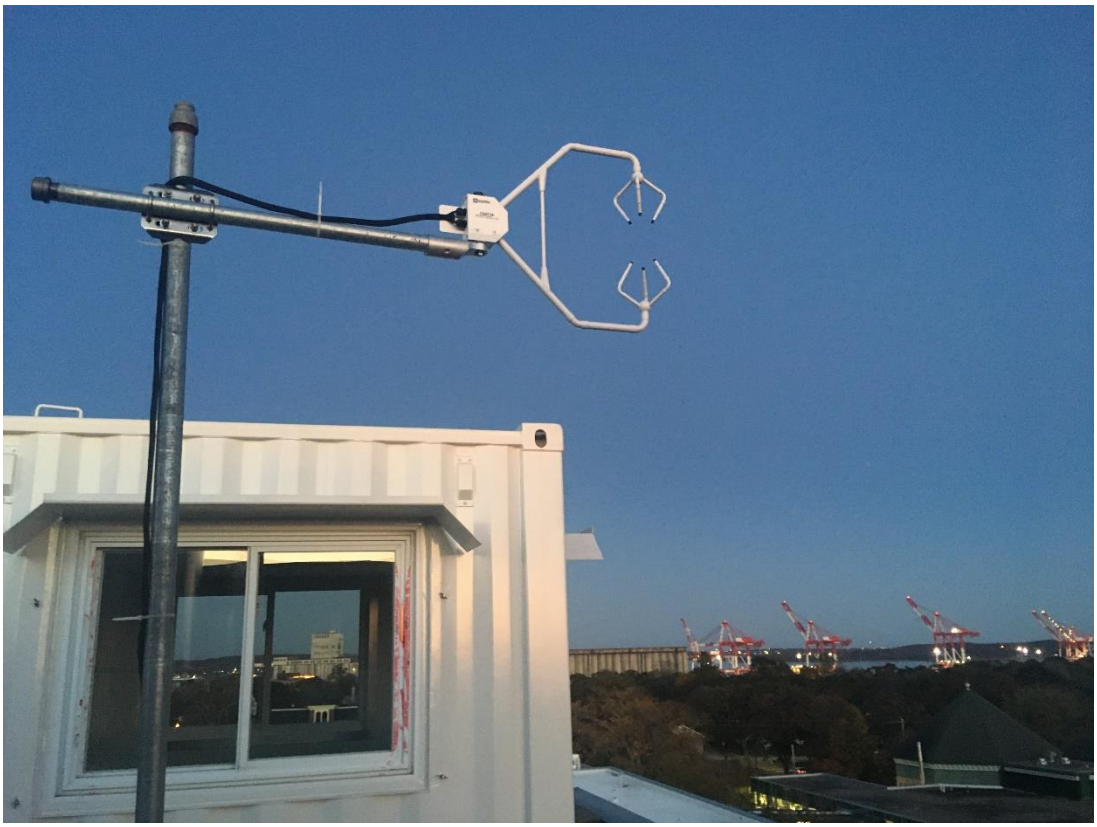

Figure 1-8: Testing the Campbell Scientific CSAT3B 3-D sonic anemometer at the Saint Mary's University (SMU) Atmospheric Observatory (SAO), pre-deployment in November 2020.

1.3. Scope of work

The goal of this work is to demonstrate a novel method for calculating gas fluxes that is advantageous for coastal ocean-air measurements. The method combines vertical concentration difference measurements by OP-FTIR spectroscopy with a flux-gradient calculation. Chapter 2 will outline the experiment design, give a summary of the measurement campaign in Halifax Harbour and review the method used to calculate ocean-air N_2O flux from concentration measurements of the spectrometer and 3-D wind measurements of the sonic anemometer. This will include an overview of the applicable micrometeorology and sonic measurement characteristics as well as some details of spectroscopic retrievals, which were both a significant "background learning" component in the course of this project. Chapter 3 discusses results from the sonic anemometer and spectrometer more broadly and shows how those results are useful in a detailed error analysis of the flux calculations. Finally, flux data are explored on long- and short-time scales. Section 3.3.4 presents a case study where we observed a physical process (strong ocean

surface cooling and possible overturning) corresponding to a clear signal in terms of ocean-air flux of N_2O. Finally, Chapter 4 summarizes the work and outcomes, reflects on successes and shortcomings of the experiment, and discusses possibilities for future study.

The author led all work related to the project (sonic deployment and field data collection, OP-FTIR data processing, sonic data processing, flux calculations and error analysis, as well as flux data interpretation) except for OP-FTIR field maintenance, which was performed by A. Wiacek. The author wrote all scripts to process data in Python, except for modifying existing MATLAB scripts for OP-FTIR data processing.

2. Methods and Analysis

2.1. Experiment Design

2.1.1. Location

Two retroreflectors, the OP-FTIR spectrometer and a 3-D sonic anemometer were deployed together in Halifax Harbour from Dec 6th, 2020, until April 28th 2021. The measurement path was 558 m one-way. Figure 2-1 shows the path, the jetty and the instruments on the jetty side (in Dartmouth) and the spectrometer in the Dockyards (in Halifax). The location has open water to the northwest and southeast of the measurement path and urban environments including docks, buildings and hills to the northeast and southwest. The surface area over which the gas flux is "sampled" (the footprint) will depend on the wind direction relative to the OP-FTIR paths. Therefore, wind direction should be considered when deciding which measurements are representative of ocean-air gas flux, and this relationship was examined in Section 3.3.3.

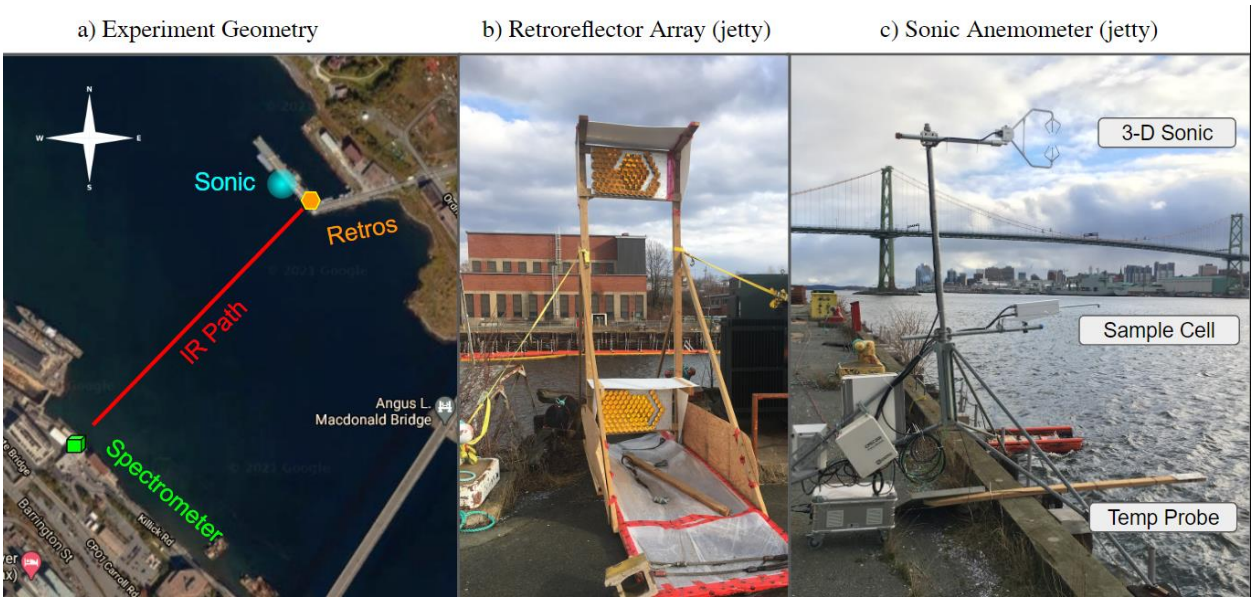

Figure 2-1: a) Layout of the experiment in Halifax Harbour. The OP-FTIR spectrometer and retroreflector arrays were connected by the 558 m IR light path. The 3-D sonic anemometer was 50 meters to the northwest of the retroreflectors on the L-shaped jetty. B) The retroreflector arrays included aluminum mounting plates for the cubes, which were fixed to a wooden structure that included plywood and plastic wind baffles, all tightly secured to anchor points that are part of the solid jetty structure c) The 3-D sonic anemometer was positioned as far over the edge of the jetty and as high as possible. The gas analyzer sample cell was used to measure barometric pressure and temperature (thermistor). A wooden beam had a temperature probe (Campbell Scientific 109; thermistor encapsulated in an epoxy-filled aluminum housing) mounted to the end out over the water.

2.1.2. Instrument deployment details

The sonic anemometer (referred to as the "sonic") was set up midway along the jetty (Figure 2-1a), which juts out into the water ~100 meters from the Dartmouth coastline. This geometry is not dissimilar from research vessels, on which sonic anemometers are also mounted routinely. This deployment represents a reasonable compromise for location in terms of minimizing the affects of turbulent eddies and nearby obstructions to the wind flow as well as providing the best exposure to the large-scale flow conditions representative of the open water. Turbulence along the jetty was investigated qualitatively during strong wind conditions by walking the length and noting where flow differed significantly from prevailing flow. The ends of the jetty had eddies coming off them, as expected from building wake theory (Arya, 2001), therefore the middle of the jetty was selected for deployment as this area had wind characteristics closely resembling the strong and steady wind conditions present during scouting. The anemometer location was at least three times the height

away from each of the surrounding structures. We also did our best to set up the tower and arm of the sonic as far over the water as possible and as high as possible, while remaining stable against vibration, to put the measuring point furthest into undisturbed flow (Figure 2-1c). This placement, while not perfect, is likely the best that could be achieved in the busy harbour at the time, also considering pandemic restrictions and constraints. The jetty juts out into the water ~100 meters from the Dartmouth coastline.

Figure 2-2 is a schematic of the experiment setup. Instruments were installed on two sides of the harbour. On the Halifax side the OP-FTIR spectrometer, telescope and electronic tripod mount was in a work trailer in the Dockyards, ~2m from the water's edge. On the Dartmouth side the retroreflector arrays and the sonic anemometer were on the jetty, which is 15m wide. The heights for all instruments were measured based on a common point on each side; W1 is the common point on the Halifax side and W2 is the point on the Dartmouth side. For example, on the diagram it shows R2, the top retroreflector, at a height of W2 + 303 cm. The center of the top retro is about 3 meters from ground level when standing on the jetty. To get the full height from the water surface, a value for W2 was found using data from a nearby ocean observation platform at the Bedford Institute of Oceanography (BIO), which is described further in Section 2.2.3.

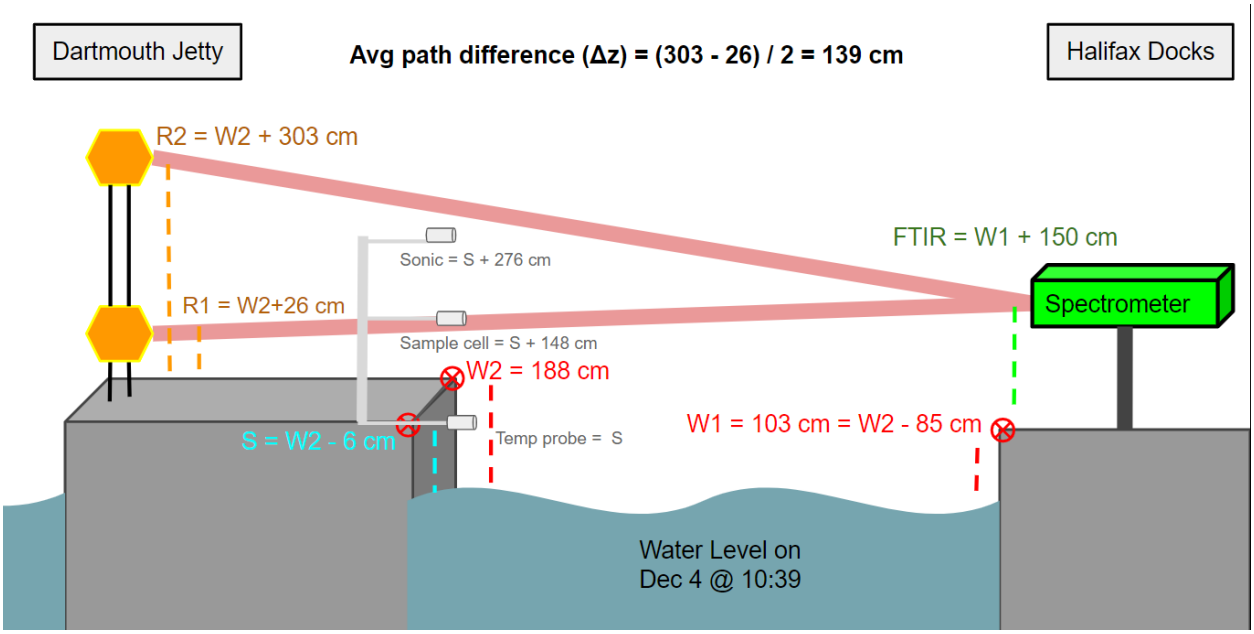

Figure 2-2: Schematic of the experiment setup. The heights for all instruments were measured based on a common point on each side. W1 is the common point on the Halifax side and W2 is the point on the Dartmouth side. S is the common point for the instruments

on the same tower as the sonic anemometer. The retroreflectors are located ~15m from the jetty edge nearest to the open ocean.

In order to directly use the height measurements from both locations in calculations, the offset between them is needed. To get the offset between the two locations, jetty (W2) and the dockyards (W1), the water level at each location was observed at the same time by two people. On Dec 4th at 10:39 W2 measured by the Hellmich on the Dartmouth jetty was 188 cm above water while at the same time W1 measured by Wiacek on the Halifax dock was 103 cm above water. Therefore, the height difference at the same time between reference points W2 and W1 was 85 cm.

From measurements of retroreflector heights, the mean vertical path separation is found. With the water level, offset and OP-FTIR height being approximately constant at any chosen time, the beam path mean height difference is the mean difference of the retroreflector heights. The average vertical separation between the IR beam paths in 2018 was 1.38 meters. In 2020 the average vertical path separation with a purpose-built mounting was 1.39 meters. The retroreflector arrays were upgraded with additional new cubes, increasing the reflector area by 50% and returning more of the IR beam that was previously lost due to smaller retros and beam divergence (Power, 2021). This change increased the signal to noise ratio and improves the accuracy of N_2O concentration retrievals. Part of the upgrade involved a stronger mounting, which also reduced shaking from wind and made array pointing adjustments easier to maximize the signal strength. Of note is the fact that we observed a greater sensitivity to non-orthogonal retroreflector array orientation towards the IR beam than what is expected from a cosine dependence of signal intensity; in other words, small adjustments to point the retros more directly at the IR beam resulted in larger than expected signal gains. The reason for this is likely related to the 3-D structure of individual reflector cubes, which begin to self-shade at beam angles that are not perpendicular to the effective cube apertures.

The mean heights of the top and bottom FTIR paths, as well as the instrument heights (required for calculation of the vertical temperature and wind profiles) vary with water level. All instrument heights were measured as height above the reference point W2. The total height is then calculated as a sum of the instrument height and the height of reference point W2 above the water surface, z_{w2}, shown in Table 1. We did infer a slight variation in these heights during measurements due to frost heave in the ground below the spectrometer (a gradual drift in the pointing of the IR beam was a symptom); however, this was not considered in the calculation of

heights as the change was likely of similar order as the uncertainty in the height measurements themselves, which was ~5 cm due to water wave motion and ground unevenness.

Table 1: Heights of instruments relevant to calculations. The height of reference point W2 above the water surface (z_{w2}) accounts for the variable height of the experiment over water as the tides ebb and flow.

Instrument	Height above water surface (meters)
OP-FTIR	0.65 + z_{w2}
Bottom retroreflector	0.26 + z_{w2}
Top retroreflector	3.03 + z_{w2}
Mean IR bottom path	0.46 + z_{w2}
Mean IR top path	1.84 + z_{w2}
Mean midpoint between paths	1.15 + z_{w2}
3-D sonic anemometer	2.70 + z_{w2}
Gas analyzer sample cell	1.42 + z_{w2}
Temperature probe	-0.06 + z_{w2}

2.2. Measurement Campaign Overview

The full campaign log in included is Appendix A. Some key events and observations are presented here. Figure 2-3 below shows an overview of when instruments were operating (and at what capacity) together with when flux calculations were possible and produced (green bands). All the instruments (the sonic anemometer, the retroreflector arrays and the OP-FTIR) experienced issues that we diagnosed and learned to correct in real time.

2.2.1. Sonic status and events

The sonic anemometer (blue bands in Figure 2-3) had four issues during the campaign. First and most frequent was that heavy rain would cause droplets to accumulate on the transducers that send the sound wave signal used to calculate the air velocity. This is unavoidable and only caused data loss in the heaviest rains at which point the OP-FTIR was also recording low quality spectra due to signal loss from all the water droplets in the beam path causing beam extinction. The second was an equipment limitation in the lack of a memory expansion add-on for the sonic data logger. This meant the data had to be downloaded every six days or records would begin to be over-written. Due to illness, weather and schedule conflicts, between a few hours and a couple days of

sonic data were missed at various times. The third issue was technically insignificant for us and did not affect the crucial u* measurement we require. It was that the EC155 gas analyzer sensor windows need to be cleaned occasionally as condensation in an ocean environment leads to salt build up and drops the signal below tolerance. This is important if the system is used in the future to also gather CO_2 and H_2O concentration data for flux calculations, which we were not doing due to various pandemic-related strains on our time and access to zero and span calibration gases. The final issue that resulted in data loss was unanticipated. Military work crews were moving heavy equipment on the jetty and severed our power cable. While the sonic was powered by a UPS with some battery backup power, it was days before the problem was noticed and the cable was replaced, so power was lost to the instrument for 4 days (outages shown on Figure 2-3). This might have been mitigated by better signage or communication with work crews with which we shared the site.

Filtering of the sonic data was performed to ensure a realistic temperature profile was being used for T(z) propagated to the N_2O retrieval process and the flux calculation. The amount of affected data was small and is also shown on Figure 2-3 in narrow yellow bands on top of the blue band. Further information about the sonic anemometer data filtering criteria is in Section 2.3.2.

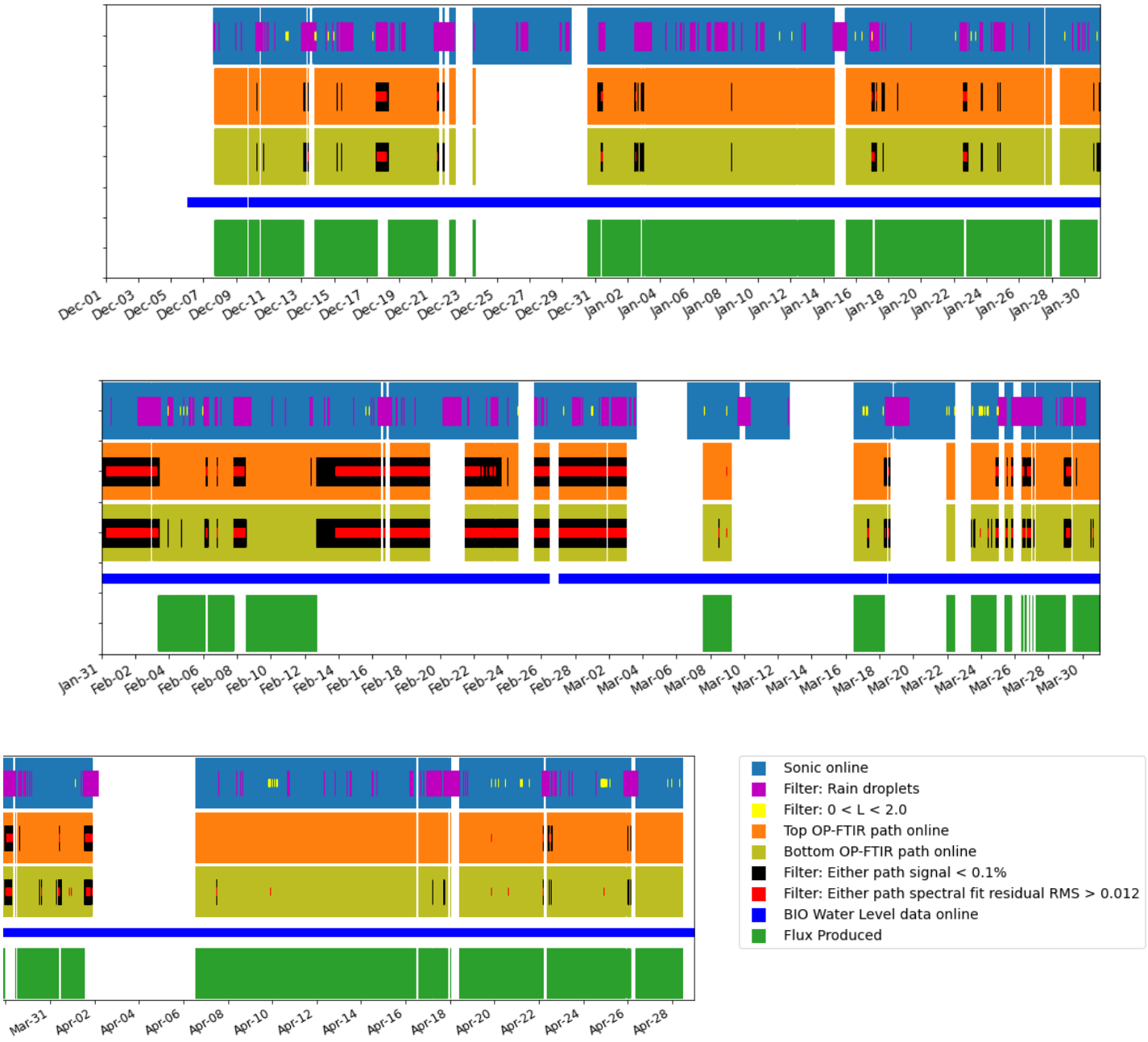

Figure 2-3: Instrumentation status during Dec 2020 – Apr 2021 field campaign, along with data status, filtering and flux calculation (green). OP-FTIR instrument status tracks signal level and retrieval quality separately in top and bottom path spectra, which are subject to different environmental factors at times. Note that since retrievals used sonic temperature data, when sonic data is missing the top and bottom paths also show as missing.

2.2.2. FTIR status and events

The FTIR encountered issues as well. During setup it took some time to get signal up to its best level as we adjusted the orientation of the retros to the telescope on the other side of the harbour. Signal refers to the IR peak level at 2500 cm^{-1}. This (arbitrary and unitless) signal value was 0-1.10 for the top path and 0-0.95 for the bottom path during this experiment. Later analysis of the data (Section 2.4.3) shows a signal of 0.1 is the minimum threshold for useable data. The retroreflectors were moved and rotated twice (Dec 11 and Dec 18) to get them pointing directly towards the FTIR as best as possible. While this did improve IR signal level from 0.60 to ~1.0, the data from before the adjustments is still very useable; in fact, Section 3.2 results show the variance of concentrations measured during 0.50 signal was not adversely affected. The biggest concern for the flux calculations was when one path had a very different condition than the other. When the signal drops very low (less than 0.10) the N_2O concentration retrieved tends to drift to unphysically low values (<< 330 ppb). There is more tolerance in the concentration difference if conditions are the same for both paths, but if only one path has issues affecting signal it can cause the appearance of a large spurious signal in the concentration difference, ΔC. The potential causes for false ΔC values are obstructions in the beam path or on the retroreflector surface as well as beam misalignment. Obstructions to the lower beam path included snow, traffic cones and parked vehicles that caused short-term issues. The mirror surface of the top and bottom retroreflector arrays encountered different rates of condensation, freezing and thawing but this was not seen to cause enough signal disagreement to be an issue. Similarly, fog/rain variation with height did not cause enough uneven obstruction between the two beam paths to be significant.

The major source of signal loss during this study proved difficult to understand. The issue turned out to be due to frost heave during the spring thaw that gradually (~12 hours) moved the structure sheltering the OP-FTIR telescope ever so slightly such that the beam did not fully fill the retroreflector area. By the time the issue was properly diagnosed and corrected this resulted in the largest period of missing data, almost a month from Feb 14th to Mar 7th, while we struggled to explain the continual degradation of signal in the spectrometer for both paths. Attempts were made for example to clean the retros (as some ice had built up on them) and heat the OP-FTIR telescope (as dew sometimes turned to frost on the internal mirrors). These are good practices in general but the improvement to signal was insignificant to the recurring loss of signal due to systematic pointing issues. Attempts were in fact made to re-point the beam, which improved the signal but

only temporarily, as the ground continued to shift. The OP-FTIR pan-tilt was in a movable commissionaire's shack on a paved dock next to a stable temperature ocean, so for ground freeze and thaw to have had this much effect was initially surprising but once this was discovered it became obvious. The area is shaded by buildings and thick sheets of ice were observed on the ground around the shack. As the ice melted the dock shifted, slowly but continually this changed the angle of our instrument with respect to the retroreflector arrays across the harbour. It is also possible that the shack itself was flexed out of shape by the freeze/thaw cycles; in 2018 it was observed that the floor stiffness was such that walking next to the spectrometer could significantly alter return signal levels from the retroreflectors 558 m away. Once identified as a freeze/thaw issues, this was compensated for by increasing the frequency of pointing calibration to once a week to ensure the OP-FITR telescope was centered on the retroreflectors for the remainder of the campaign, however the transition to spring temperatures also eliminated this problem. In future measurements, freeze/thaw pointing adjustments may be necessary on a daily basis.

2.2.3. Water level status and usage

Tidal water level measurements provided by the Canadian Hydrographic Service were located at the Bedford Institute of Oceanography (BIO). The tidal data was used to find the distance from the water surface to the instruments on the jetty. The data was available at a 1 min frequency (202359 total entries). The BIO is located 2.5 km NW from the measurement site further inside the harbour at the mouth of Bedford Basin. Additional observations were made for calibration of the water heights at BIO and W2 on the jetty. Periodic (~bi-weekly) water level measurements with respect to W2 were taken by tape measure at the jetty throughout the campaign. These measurements were used to calculate the height offset between our measurement reference point W2 and the one at BIO.

The total number of matched water level observations with the sonic data (not including missing observations) is 176832, while 4877 valid sonic data entries do not have water level data (2.7% or approximately 3.4 days worth of data). Each instrument's height (h_{ins}) was recorded with respect to a reference point on the jetty called W2 (previously discussed in section 2.1.2). The height of W2 above the water surface (z_{w2}) was measured 12 times during the observation period.

An offset was found from the mean sum of observed water levels at BIO (z_{BIO}) and z_{w2}. The offset was calculated as:

$$\text{offset} = \text{mean}(z'_{BIO}) + \text{mean}(z'_{w2}) ,$$

where z'_{w2} refers to the calibration measurements made using a tape measure (with an estimated precision of 5 cm due wave action) and z'_{bio} refers to BIO data at corresponding observation times. Figure 2-4 shows a comparison of the z'_{bio} and z'_{w2} data. The two data sets look like mirror images of each other; this is because they are very similar to each other apart from a constant offset and an x-axis reflection. The reflection about the x-axis is because the BIO measures water level above a reference point and the calibration measurements were from the reference point (above the water) to the water surface. The offset is applied to the BIO data to convert the observations to the reference point W2 as follows:

Equation 1 $$z_{w2} = \text{offset} - z_{BIO} ,$$

where z_{BIO} is the full data set available for the measurement period. Having used the offset to convert BIO minutely water level measurements into the equivalent height at W2, the instrument height above the water level can now be calculated as:

$$z_{ins} = h_{ins} + z_{w2} .$$

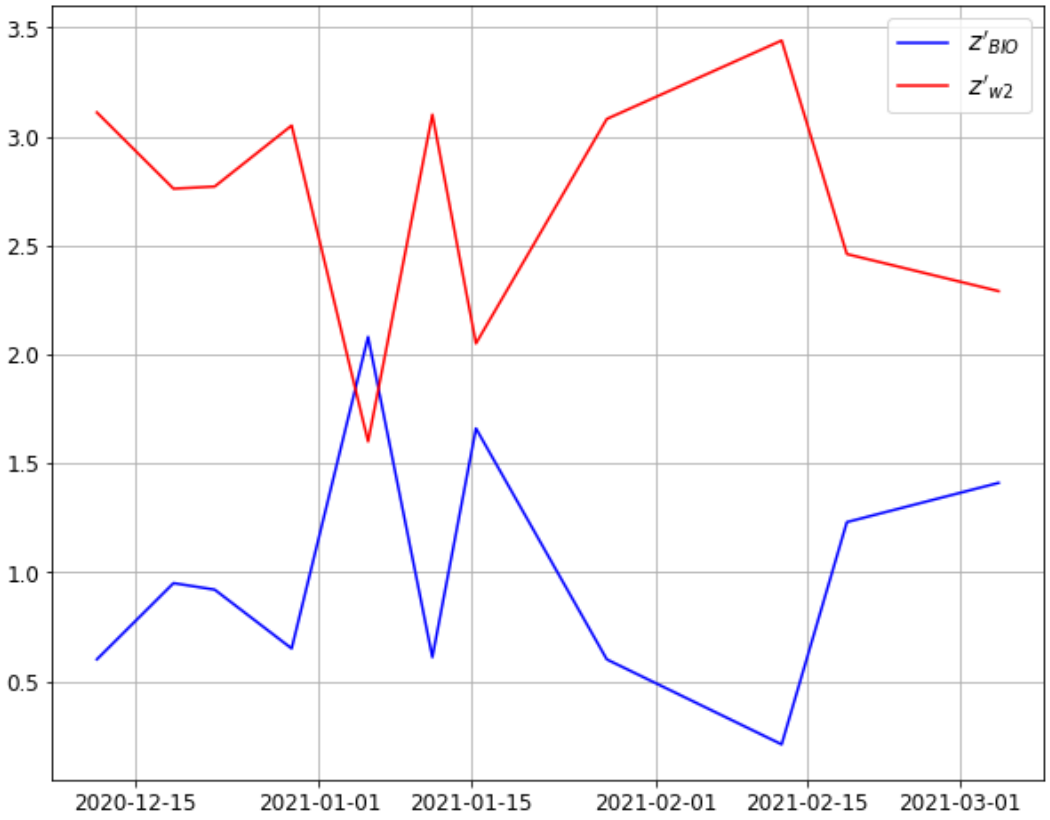

Figure 2-4: Comparison of the z'_{BIO} and z'_{w2} water level data. For clarity, only points where calibration observations at the jetty are available are shown.

It was assumed that the tidal measurements at BIO are located close enough to the jetty (2.5 km) for the variation of tide arrival time to not influence the calculation of z_{w2}. This was confirmed by the close agreement shown in Figure 2-5 between the observed z'_{w2} heights and the calculated z_{w2} values (from BIO values with the constant offset applied). The root mean square error (RMSE) between the two data sources is 1.8 cm or <1% of the mean tidal height.

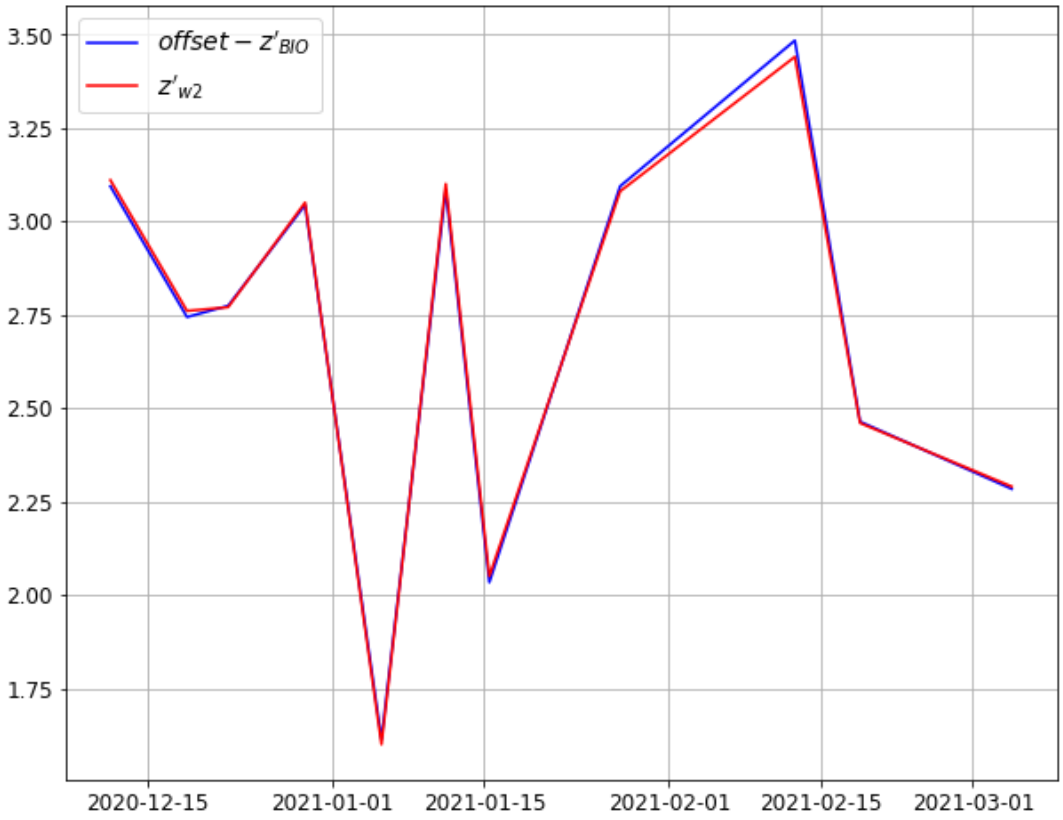

Figure 2-5: Observed jetty height above water (z'_{w2}) compared to calculated jetty height above water (z_{w2}) using calibrated BIO Tidal Data (Equation 1).

During the lowest tide the jetty surface was at z_{w2} = 3.93 m above the water surface, while during the highest tide the jetty was at z_{w2} = 1.15 m above the water surface. The mean height of the jetty above water level was z_{w2} = 2.51 m.

2.2.4. Overall Data Completeness

The data sets, including top and bottom path N_2O concentrations, sonic anemometer and water level measurements, were merged into intervals of 4 min 19 s, which is the time it takes for the OP-FTIR to record a spectrum along the bottom path, move up, then repeat for the top path and move down to start again. The measurement observation times were centered on the middle of the observation, when the top path spectrum begins recording. Missing data from the sonic, FTIR, and BIO water level results in varying completeness of the final flux data set; Figure 2-3 showed what that looks like on a timeline of produced flux (in green). The total number of 4 min 19 s intervals that could have been observed between Dec 7th 2020 and April 28th 2021 is 47369,

but the number of actual observations at the end of the process was 25769, for a final data completeness of 54%.

2.3. Micrometeorology

2.3.1. Flux formula

The concentration difference, $\Delta C_s = C(z_2) - C(z_1)$, for a gas, s, is found from the OP-FTIR measurement over a height difference, $\Delta z = z_2 - z_1$, where z_2 is the average top path height and z_1 is the average bottom path height. ΔC_s is related to flux of the gas, F_s, via Equation 2 as shown in Flesch et al., (2016):

Equation 2 $$F_s = -K_s \rho_a \frac{M_s}{M_a} \frac{\Delta C_s}{\Delta z} .$$

The density of dry air is ρ_a, while M_s and M_a are the molar masses of the gas s and dry air, respectively. The diffusivity of the gas, K_s, can be related to the momentum eddy diffusivity, K_m, with Equation 3 (Flesch et al., 2016):

Equation 3 $$K_s = \frac{K_m}{S_c} = \frac{u_*^2}{Sc \Delta U} \Delta z .$$

The turbulent Schmidt number, S_c, is estimated to be 0.64 (Flesch et al., 2002). The difference in average wind speed, ΔU, is found using the stability-corrected logarithmic wind profile,

Equation 4 $$\Delta U = \frac{u_*}{k_v} \left[\ln\left(\frac{z_2}{z_1}\right) - \psi_m\left(\frac{z_2}{L}\right) + \psi_m\left(\frac{z_1}{L}\right) \right] ,$$

where the von Karman constant is 0.4 and the MOST stability correction function, ψ_m, is described below. For the measurements in 2020-2021, we used a 3-D sonic anemometer, which measures the wind velocities (Ux, Uy, Uz) and the acoustic temperature, all sampled at 10 Hz. The averages, variances, and covariances of these variables are used to calculate the average wind velocities, the average wind direction, the friction velocity, and the Obukhov stability length, with calculation

details shown below in Section 2.3.2. The outputs from the 3-D sonic anemometer are used in the flux calculation as well as to infer the vertical temperature gradient for FTIR retrievals (Section 2.3.2). As with Flesch et al. (2016), it is assumed that the acoustic temperature gradients (inferred from the sonic anemometer measurements) are equivalent to the actual temperature gradients (used for the FTIR retrievals). In 2018 the 3-D sonic anemometer was unavailable, and a method for approximating flux was developed, which is included in the Appendix Section B.

The full flux formula is derived by substituting Equation 3 and Equation 4 into Equation 2 and integrating over the OP-FTIR measurement path. The equation needs to be integrated over the measurement path, ℓ_{path}, since height varies along the path horizontally from x_1 to x_2; z_1 and z_2 are heights on the bottom and top paths, respectively. The final formulation of Flesch et al., (2016) is shown in Equation 5.

Equation 5
$$F_s = -\frac{k_v \rho_a u_*}{S_c}\frac{M_s}{M_a}\frac{\Delta C_s}{\frac{1}{\ell_{\mathrm{path}}}\int_{x1}^{x2}\left[\ln\left(\frac{z_2}{z_1}\right)-\psi_m\left(\frac{z_2}{L}\right)+\psi_m\left(\frac{z_1}{L}\right)\right]dx}$$

The MOST stability correction, ψ_m, is selected based on the value of the buoyancy parameter, z/L,

$$\psi_m\left(\frac{z}{L}\right) = -5\frac{z}{L} \qquad (L > 0 \ \text{Stable})$$
$$\psi_m\left(\frac{z}{L}\right) = 2\ln\left(\frac{1+y}{2}\right) + \ln\left(\frac{1+y^2}{2}\right) - 2\tan^{-1} y + \frac{\pi}{2} \qquad (L < 0 \ \text{Unstable}),$$

where $y = \left(1 - 16\frac{z}{L}\right)^{1/4}$. This numerical analysis was implemented in Python and the integral in the denominator of Equation 5 was solved numerically using the trapezoid rule. This formulation assumes that the surface is smooth to moderately rough (a safe assumption for the harbour water surface), the measurement height is in the constant flux surface layer and the measurement path is horizontally homogenous. Furthermore, since the surface is flat the functions $z_1(x)$ and $z_2(x)$ representing the beam paths are these linear functions,

$$z_1(x) = \frac{z_{R1} - z_{FTIR}}{\ell_{\mathrm{path}}}x + z_{FTIR}$$

$$z_2(x) = \frac{z_{R2} - z_{FTIR}}{\ell_{path}} x + z_{FTIR} ,$$

remembering that the height above the water surface of the instruments is for example,

$$z_{FTIR} = h_{FTIR} + z_{W2} ,$$

as explained in section 2.2.3. The dry air density, ρ_a, was found using the retrieved concentration of H_2O from OP-FTIR, converted to mmol,

Equation 6
$$\rho_a = \frac{P_{cell}}{Rd\, T(z_{mid})_{Kelvin}} \frac{1 - [H2O]_{mmol}}{1000 + [H2O]_{mmol}} ,$$

where $T(z_{mid})_{Kelvin}$ is the value of the vertical temperature profile (Equation 9 shown below in Section 2.3.2) at the mean midpoint height between the beam paths, and Rd is the gas constant for dry air, $2.867x10^{-4}$ kPa m^3 kg^{-1}.

The Halifax Harbour ocean surface can be assumed to be aerodynamically smooth and flat even with small waves because the surface roughness is low compared to solid buildings or tall vegetation (Arya, 2001). Furthermore, in a smaller body of water like a harbour the waves are wind-waves (weak and generated nearby), which, unlike swell-waves (strong and generated far away), move in the same direction as wind in the harbour. Wind-waves have lower surface roughness because they travel with the wind and less momentum is transferred between the air and water. While large swell, when moving against the wind could have a higher surface roughness, in the harbour the waves are always small wind-waves. The biggest obstruction to flow is the dockyard and jetty at the edges of the path. These represent only 2% of the path for the IR beam. The jetty's significance within the sonic anemometer footprint is examined further in the results (see Section 3.3.3).

2.3.2. Sonic data processing and characteristics

The total number of observations obtained during the period Dec 6th, 2020, to April 28th 2021 was 181709. If data were being collected 100% of the time the potential observations would be

205920 at minutely sampling frequency, therefore the sonic was operating 88% of the time. The instrument operates at 10 Hz but was programmed to output minutely average values and calculated covariances. An observation is logged as incomplete if there are less than 50 samples out of a potential 600 per minute due to, for example, rain droplets on the sonic transducers. As discussed previously, there are also missing data chunks of about 8-10 days due to late downloads (holidays, illness) and a power outage; these are not recorded so they are not included in the incomplete observation fractions in Table 2.

Table 2: Sonic anemometer data products

Description	Symbol	Incomplete (Percentage)
Friction velocity	u_*	13407 (6.5%)
Acoustic temperature	Ts	12218 (5.9%)
Covariance between Ts and Uz (vertical wind speed)	$\langle Uz, Ts \rangle$	13407 (6.5%)

According to the method selected by the manufacturer described by Roland et al. (2006), u_* is calculated from covariances of wind speed components Ux, Uy, and Uz (in instrument coordinate system bubble-levelled with surface):

Equation 7 $$u_* = (\langle Ux, Uz \rangle^2 + \langle Ux, Uy \rangle^2)^{\frac{1}{4}} .$$

The Obukhov length, whose sign determines the form of the stability correction, is calculated from sonic outputs in Equation 8 as shown by Rebmann et al. (2012).

Equation 8 $$L = \frac{-{u_*}^3}{g k_v} \frac{Ts_{Kelvin}}{\langle Uz, Ts \rangle}$$

Some resulting statistics for 1/L (proportional to the water surface heat flux): the mean for the entire measurement period is -0.03 and over 75% of the data is negative, i.e., unstable surface

layer conditions prevail. The unstable conditions are the result of the surface water temperature being greater than the air temperature. Figure 2-6 shows a time series of 1/L, while the histogram for 1/L is also shown in Figure 2-7.

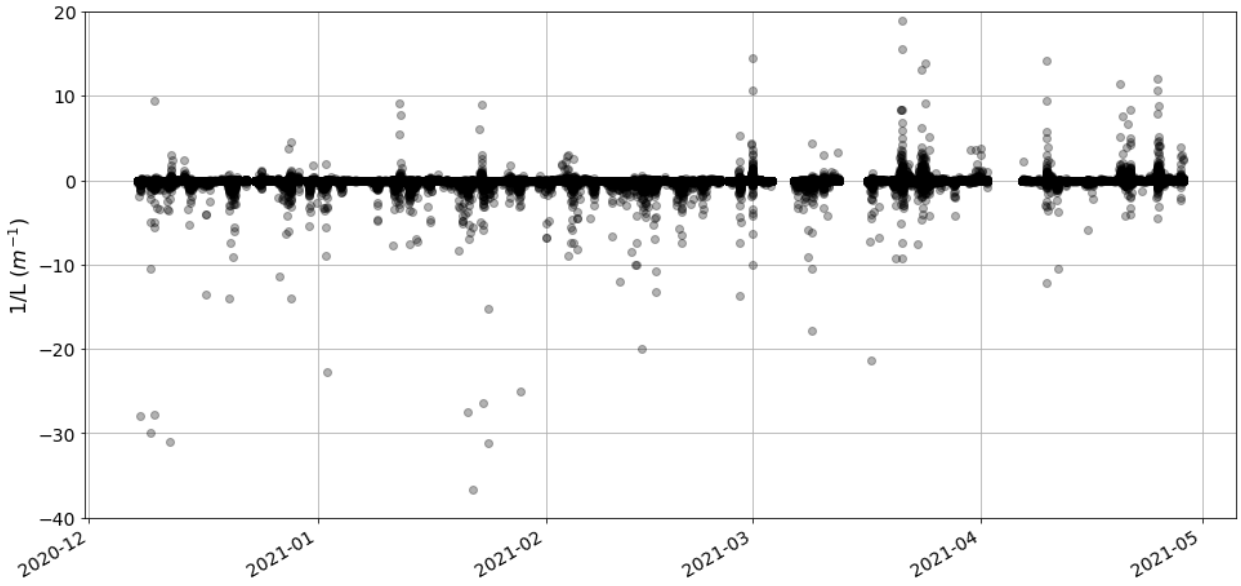

Figure 2-6: Time series of 1/L.

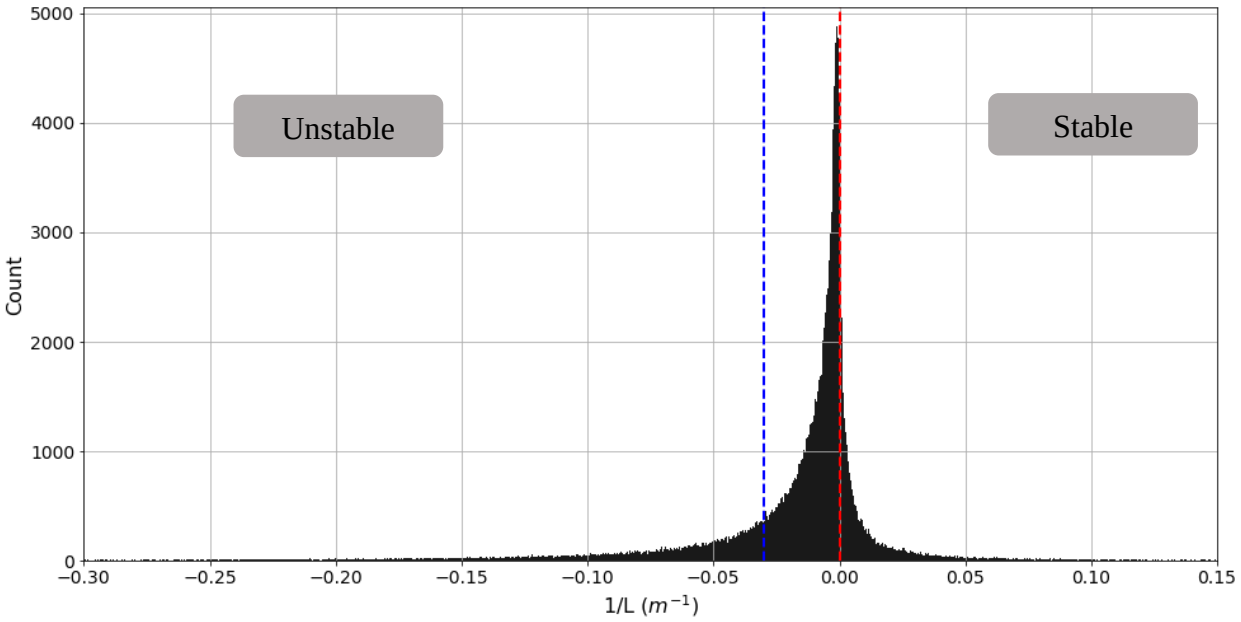

Figure 2-7: Histogram of 1/L. Red line indicates 1/L = 0. The x-axis is limited to view only 88% of the data so that the peak shape is visible. The mean of this selection of data is -0.018. The mean for the whole data set is -0.030 (indicated by blue line).

Next, the temperature as a function of height is also represented by a stability-corrected log profile, similar to the velocity profile in the MOST formalism (Flesch et al., 2016). The temperature profile, T(z), at the sonic anemometer instrument location is calculated from the sonic temperature, the friction velocity, and the Obukhov length (Ts, u_*, L):

Equation 9 $$T(z) \cong \frac{u_*^2 Ts_{Kelvin}}{k_v^2 g L}\left[\ln\left(\frac{z}{z_s}\right) - \Psi_H\left(\frac{z}{L}\right) + \Psi_H\left(\frac{z_s}{L}\right)\right] + Ts_{Kelvin}\ .$$

$$\Psi_H\left(\frac{z}{L}\right) = \begin{cases} -5\frac{z}{L} & (L > 0)\ \text{Stable} \\ 2\ln\left[\frac{1+y^2}{2}\right] & (L < 0)\ \text{Unstable} \end{cases}$$

The height of the sonic instrument's measurement point is z_s. The value of T(z) was calculated for the mean path height for the top and bottom paths using this formula, accounting for height variations due to tides, and those temperature values were used in the spectroscopic retrieval of concentrations. Resulting statistics for T(z) at the mean height (variable in time) of the bottom and top paths are shown in Table 3.

Table 3: Statistics for T(z) at the time-variable mean height of the bottom and top paths. The total count is smaller than the total sonic data entries (181709) because this is now merged with water level data.

	$T(z_{bottom})$	$T(z_{top})$
count	161233	161233
mean	2.55	2.55
std	6.71	5.54
min	-1391.00	-537.00
25%	-1.05	-1.10
50%	2.33	2.29
75%	6.07	6.07
max	21.94	21.81

The temperature calculation produced extremely negative temperatures (T(z) < -30°C), which were obviously not physical, for ~300 data points (0.19%). The temperature differences between calculated T(z) at the two mean path heights as well as the temperature measured from the gas analyzer sample cell (T_{cell}), since they are all with ~1 m of each other, should be within a reasonable range of the moist lapse rate of 6.5 °C/km, which over the mean path difference of 1.385 m amounts to 0.01 °C. Allowing for instrumental bias between measured Ts and T_{cell} and potential uneven heating of the air near the jetty, as well as expected departures from the average lapse rate, the difference in temperatures should still be within a few degrees on average (as is clear from the statistics shown in Table 3). Figure 2-8 shows calculated $T(z_{top})$ compared to measured T_{cell} for the month of January; Figure 2-9 shows the difference between calculated $T(z_{top})$ and measured T_{cell}, from now on referred to as T_{error}, over the same date range. T_{cell} is measured by the gas analyzer sample cell, which is located closer to the top path then the bottom path at 42 cm below the mean top path. It is expected that T_{error} should only be a few degrees. It is unclear if data points subject to artifacts from the T(z) calculation can be found by looking for unphysically negative temperatures alone. The solution to this was found by characterizing the data as a function of u_* and L.

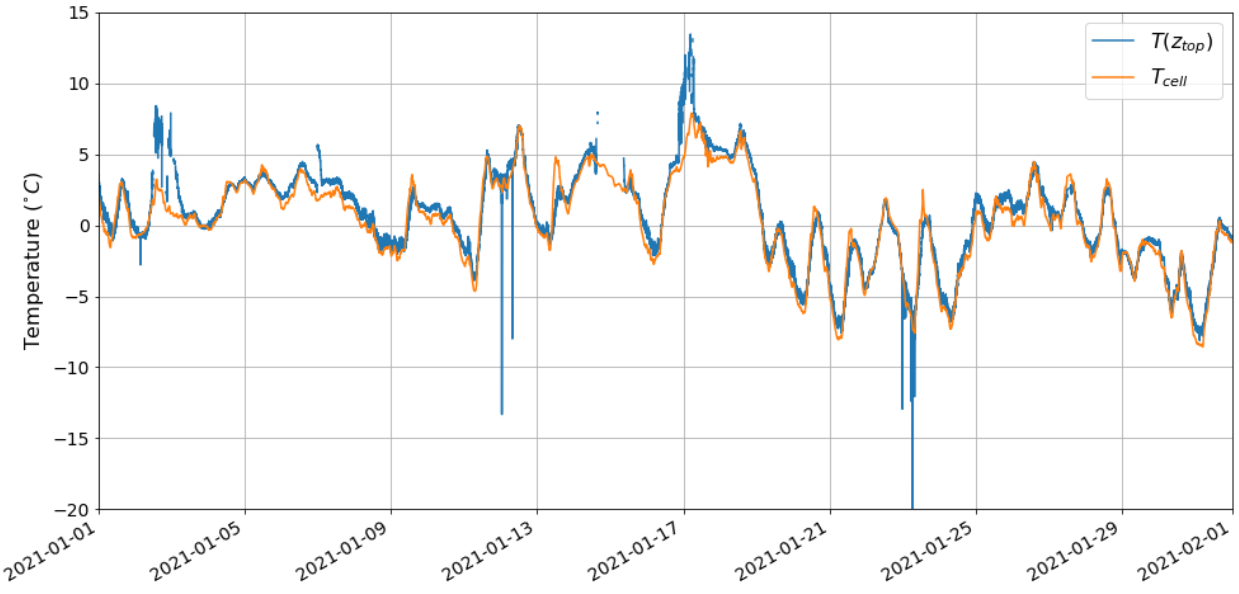

Figure 2-8: The temperature at the height of the mean top path, $T(z_{top})$, should be the closest to the temperature measured by the gas analyzer sample cell, T_{cell}. Plotted only for the month of January to show finer details.

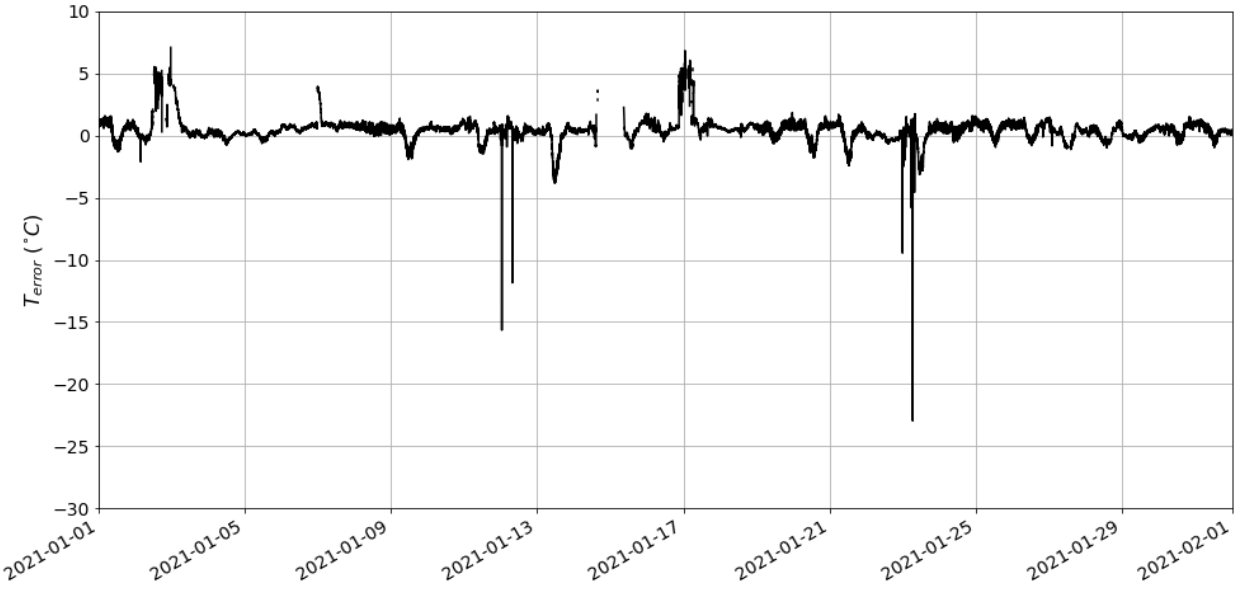

Figure 2-9: The temperature difference between $T(z_{top})$ and T_{cell}, from now on referred to as T_{error}. While anomalies on January 12th and 23rd certainly appear suspicious, it is not completely clear from T_{error} alone which data points are an artifact produced by the T(z) calculation.

To help identify where the T(z) calculation is causing errors due to the breakdown of MOST, u_* versus T_{error} was plotted and this produced an elbow-shaped curve, shown in Figure 2-10. From this plot it is apparent that the breakdown in the T(z) calculation is contained below a u_* of 0.2 m/s. The most extreme discrepancies are below a cut-off of 0.05 m/s, but it is not clear how to become convinced of what precise u_* cut-off is most appropriate such that all the points in this segment of data are biased in the same way. For example, there are still many reasonable temperatures at low u_* values, even below 0.05 m/s.

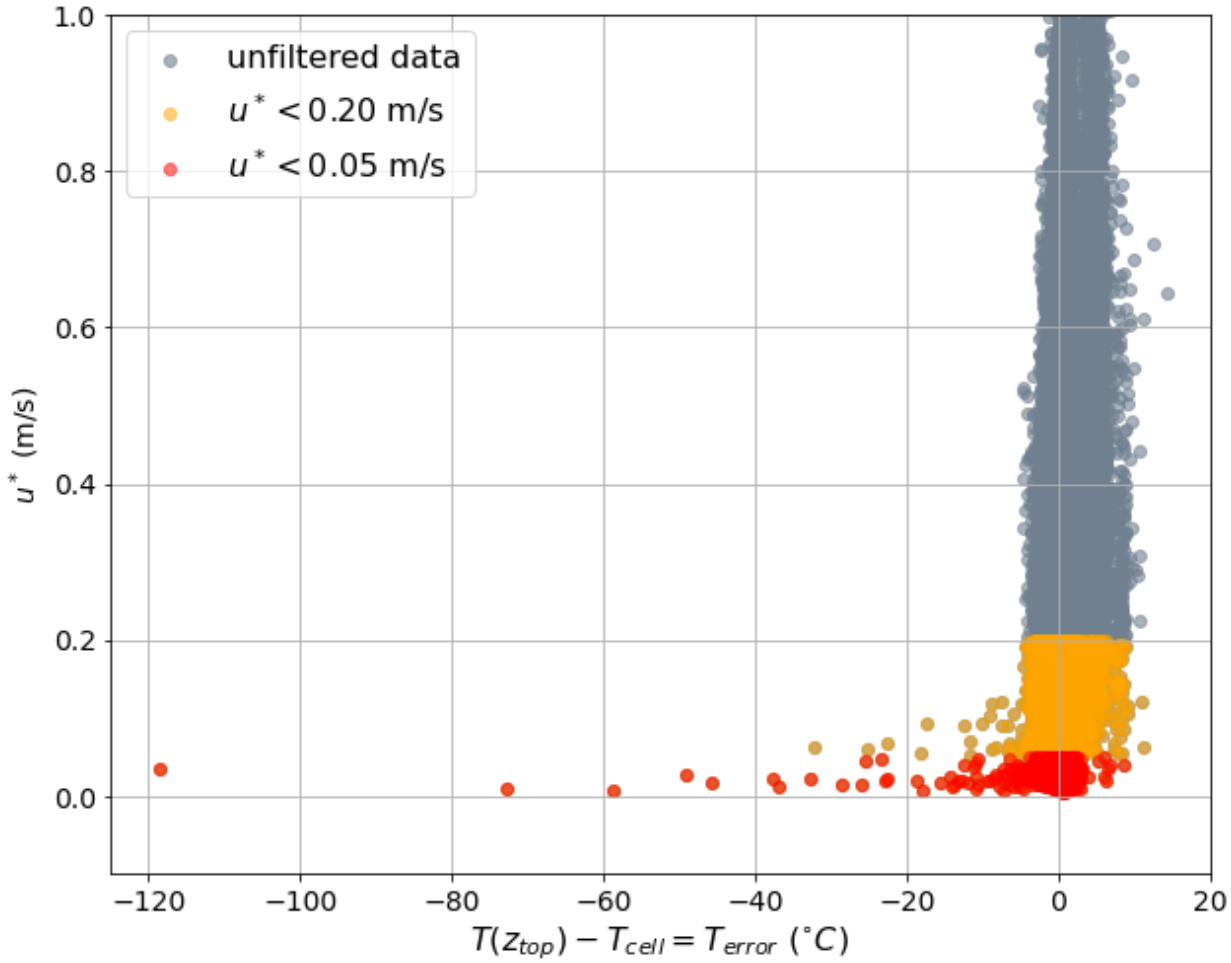

Figure 2-10: Plotting u_* versus T_{error} produces an elbow-shaped curve that is suggestive of a breakdown point in the T(z) calculation. Red and yellow segments identify data with u_* less than 0.05 m/s and 0.20 m/s, respectively.

It was shown in Table 3 that $T(z_{top})$ and $T(z_{bottom})$ are very similar data sets. $T(z_{bottom})$ is one meter below where T_{cell} is measured. This is double the distance from T_{cell} to $T(z_{top})$. $T(z_{top})$ was used to decide on a filtering method for the T(z) calculation, while $T(z_{bottom})$ was used to test the method. Therefore, Table 4 shows statistics relating to $T(z_{bottom})$ when temperatures corresponding to the u_* segments shown in Figure 2-10 are filtered out. Filtering u_* too high, e.g., 0.2 m/s eliminates large numbers of data points unnecessarily (30%). Figure 2-11 shows how u_* filtering looks in the temperature time series. It is evident that the $u_* > 0.2\ m/s$ filter removes temperatures that follow the temperature trend. Filtering at u_* of 0.05 m/s removes only 3204 (2%) of the data points but still leaves unphysical temperatures as can be seen in the table where the minimum value is -74°C. There could be a middle-ground value of u_* to use, however this seemed too arbitrary, and the investigation of L characteristics below provided a better solution.

Table 4: Statistics of $T(z_{bottom})$ when temperatures corresponding to the u_* segments are filtered out. Values in °C.

	No u_* filter	u_* > 0.05 m/s	u_* > 0.2 m/s
count	161233	158537	113483
% lost	0	2.0	29.7
mean	2.55	2.57	2.89
std	6.71	5.27	5.39
min	-1391	-74.28	-11.86
25%	-1.05	-1.06	-0.79
50%	2.32	2.31	2.57
75%	6.07	6.06	6.48
max	21.94	21.94	21.94

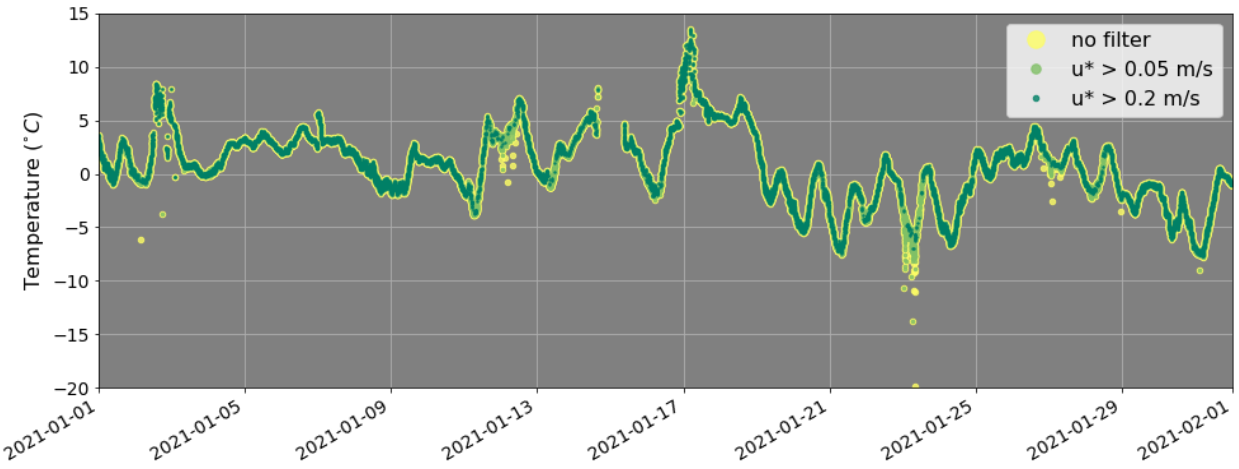

Figure 2-11: u_* filtering effects shown on the times series of $T(z_{bottom})$. $u_* > 0.2$ m/s removes points that follow the trend while $u_* > 0.05$ m/s leaves points that are erratic.

To look further into why low u_* values are associated with the temperature errors, L (which is derived from u_*) and the covariances used to calculate u_* were also plotted versus the temperature difference T_{error}. Figure 2-12 shows T_{error} plotted against L, and the covariance between the pairs (Ts, Uz), (Ux, Uy) and (Ux, Uz). Near zero each of these parameters coincides with large negative values in the T(z) calculation, and therefore, in T_{error} as well. Wind speeds close to zero lead to the covariance parameters tending to zero and this causes nonphysical results in the T(z) calculation. From the data it appears that the discontinuity in L tends to negative infinity from the positive L side, which is the stable case. On the unstable (L < 0) side it appears that the ln and 4th root functions in Equation 9 either slow or cancel out the 1/L discontinuity, at least enough to suppress it in the data. This agrees with expectations from MOST theory wherein the calculations break down due to near zero wind speeds, when stability correction terms become erroneous and sonic measurements can also become error prone (Arya, 2001). Therefore, an attempt was made to filter data points based on the discontinuity in L to see if it led to a more targeted way to flag and remove the artifacts in T(z). Figure 2-13 shows the elbow-shaped curve from Figure 2-10 now with a filter for L in the range of 0.0 < L < 2.0. This L filter range was chosen because it eliminates the discontinuity observed in L in Figure 2-12 (top-left plot). In Figure 2-13 it is apparent that this L filter eliminates all the obvious high error temperatures while leaving more points intact at a range of lower u_* values. Figure 2-14 is the temperature plot, as in Figure

2-11, this time with L filtering instead of u* filtering. It shows a more effective yet conservative filtering when based on L.

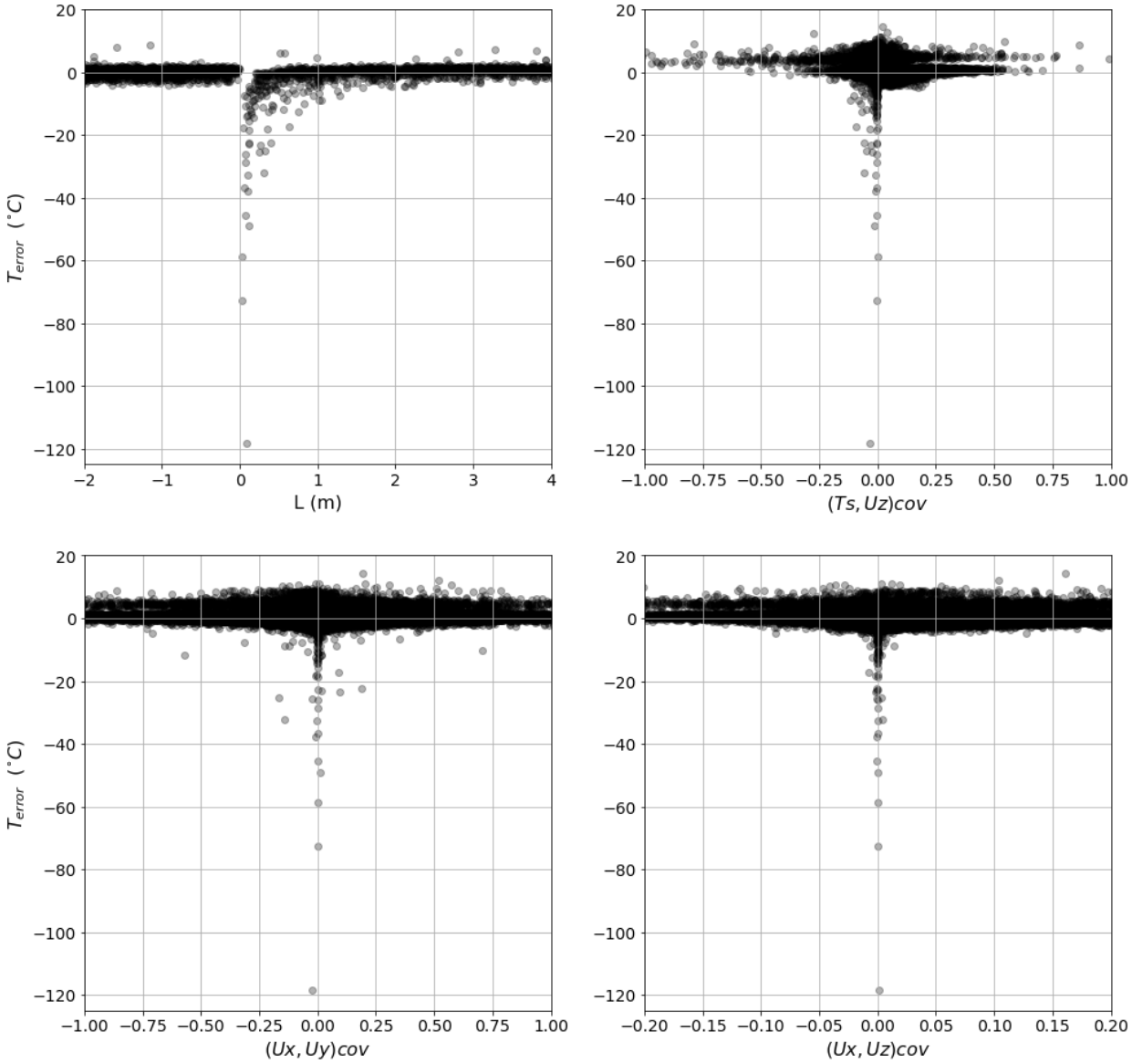

Figure 2-12: T_{error} versus L (top-left) and versus the covariance between the pairs Ts & Uz (top-right), Ux & Uy (bottom-left) and Ux & Uz (bottom-right).

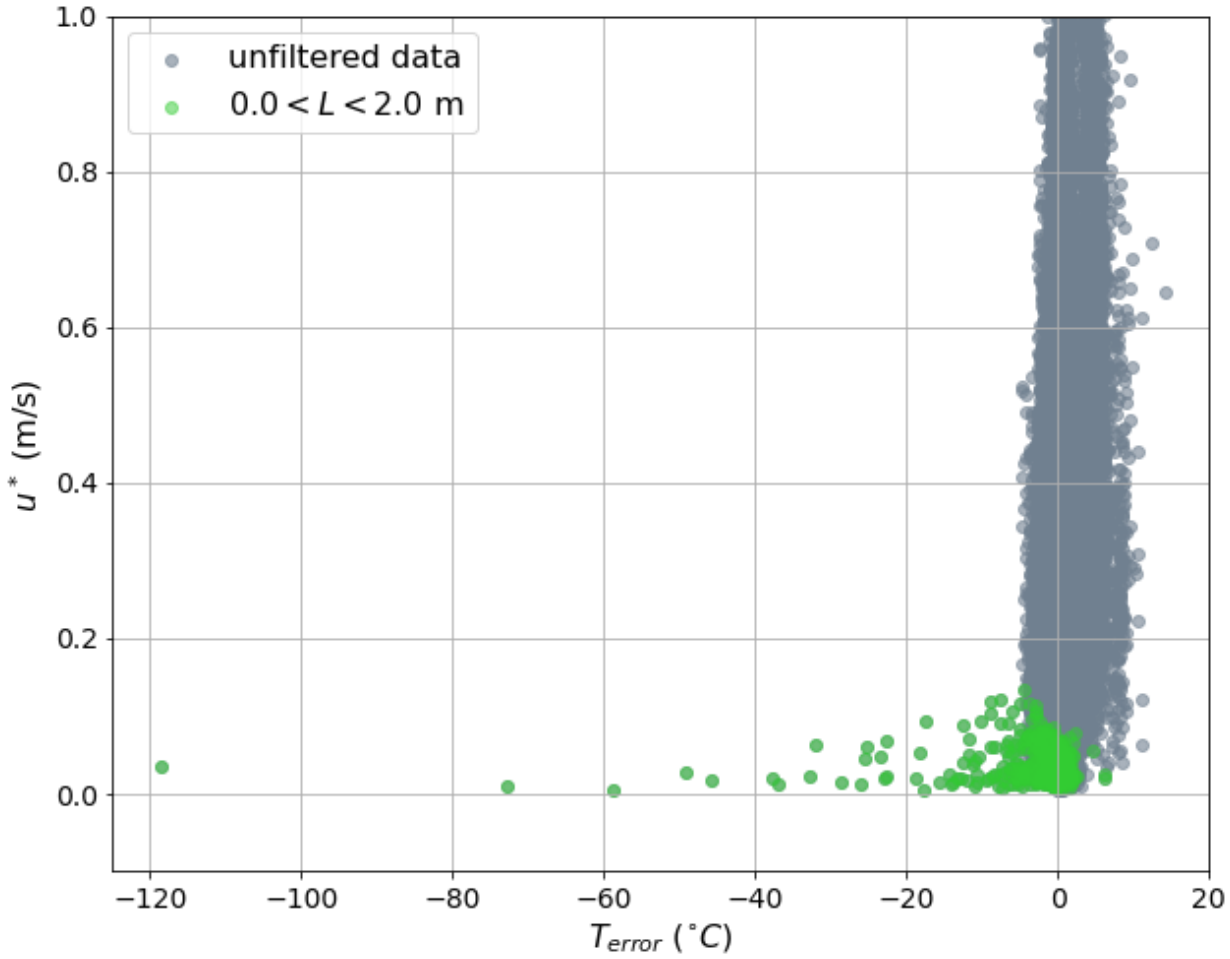

Figure 2-13: u_* versus T_{error} 'elbow plot'. Green region shows the filtered data for an L filter with the range of 0.0 < L < 2.0.

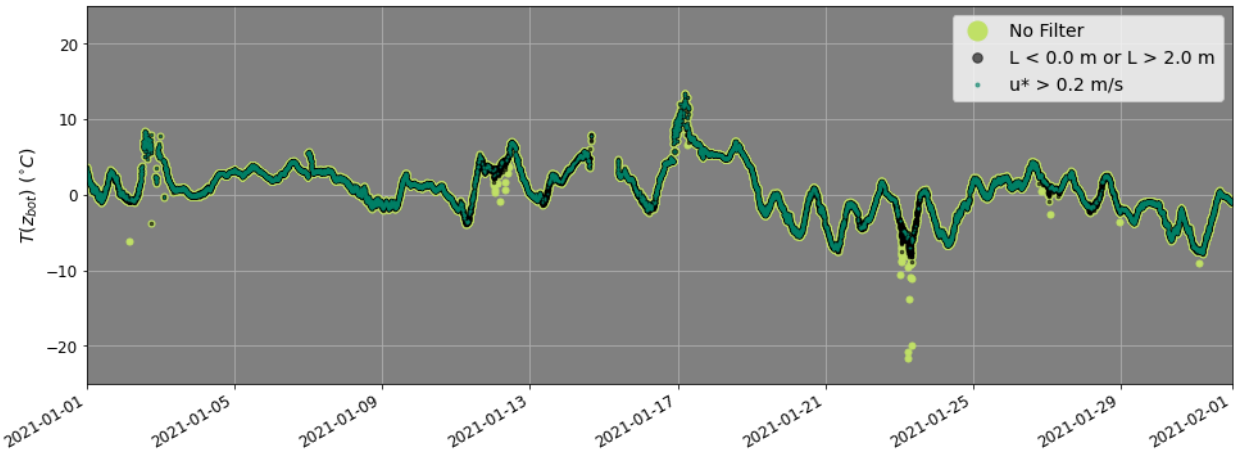

Figure 2-14: L and u_* filtering effects compared in the times series of $T(z_{bottom})$. A filter of $u_* > 0.2$ m/s removes too many points while the L filter is conservative of data but removes obvious regions where calculated T(z) has broken down.

Filtering out data points where L is between 0 and 2.0 more specifically targets the data where T(z) calculation produces unphysical values but keeps many more data points intact. Table 5 shows $T(z_{bottom})$ statistics after L filtering, which only removes 648 points (0.4%) compared to 3204 points (2.0%) with the weakest recommended u_* filter that still does not remove many unphysical points. To remove all the unphysical points a u* more like 0.2 m/s could be used which eliminates 48445 points (30%), but many of those points are very likely mis-targeted and removed unnecessarily. Ultimately, the L filter was used to produce flux results, however further filtering with u* could be performed in future investigations if necessary. The FTIR retrievals were performed with unfiltered temperature data so that retrieval results could be fully analyzed with respect to these filtering methods as well. Finally, Figure 2-15 shows the filtering comparison for $T(z_{bottom})$ during the entire measurement period.

Table 5: $T(z_{bottom})$ statistics as a result of L filtering. Remaining points are all within a plausible range for the observation campaign.

	Removed points (0 < L < 2.0)	Remaining points (L < 0 or L > 2.0)
count	648	160585
% of total	0.4 %	99.6%
mean	-4.90	2.58
std	65.66	5.25
min	-1391.09	-11.86
25%	-3.25	-1.05
50%	2.84	2.32
75%	6.61	6.06
max	15.05	21.94

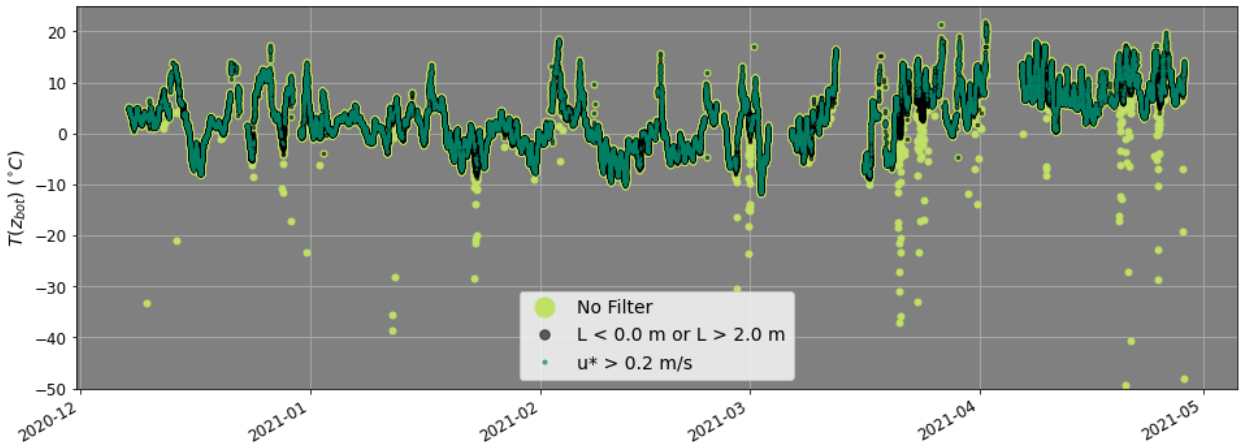

Figure 2-15: The temperature for $T(z_{bottom})$ during the whole campaign with L and u_* filtering effects compared.

2.3.3. Surface roughness homogeneity

In certain scenarios the assumption of a homogenous surface layer used in calculating the N_2O fluxes (Section 2.3.1) may not be valid. Depending on wind direction, the topography and structures in the harbour may have an impact on air flow measured by the sonic anemometer, and thus be unrepresentative of the flow over open water. Wind flowing on the NW-SE axis is parallel

to the shore and the assumptions made about the homogeneity of the surface layer over the smooth/flat water surface are assumed to hold. However, for wind flowing on the SW-NE axis the instrument footprint includes the ocean surface, as well as the jetty and urban structures. On this axis, there are step changes in the surface roughness, z_o, and surface temperature, which violate the homogenous surface layer assumption and may affect the flux calculation. Figure 2-16 shows the wind roses for 2- and 10- m measurements in the harbour during the 2018 campaign. The 2-m measurement is from a 2-D sonic anemometer on the jetty. The 10-m measurement is from a METOC station at CFB Halifax, 1.6 km away, very nearly at sea level. The measurement spans September 15th to October 20th. It is encouraging to see that the prominent wind direction is along the water, with the harbour likely behaving as a channel during this period. Wind direction is considered in the results of the 2020/2021 campaign and in Section 3.3.3.

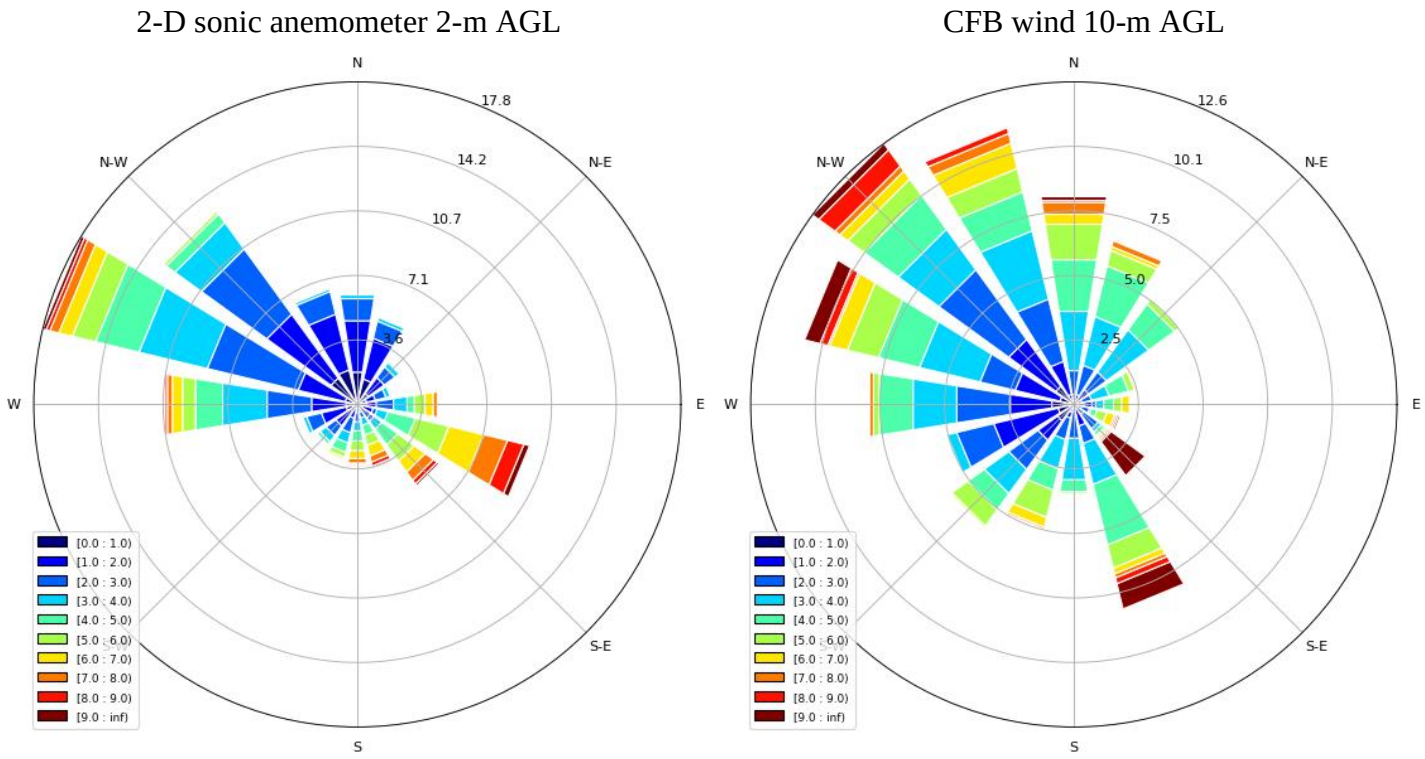

Figure 2-16: Wind roses for measurements at 2-m and 10-m heights above ground level, very near sea level. The 2-m measurement is from a 2-D sonic anemometer on the jetty. The 10-m measurement is from a METOC station at CFB Halifax, 1.6 km away. The measurement spans September 15th to October 20th in 2018. Percent distribution is shown radially, angle represents wind direction and colour represents wind speed in ms^{-1}.

2.4. Spectroscopic Retrievals

This section describes the work carried out to optimize the retrievals of N_2O from IR absorption spectra recorded between the spectrometer and retroreflectors on the opposite side of the harbour. The 'retrieval' process involves simulating the absorption spectra of all significant gases within the spectral range where N_2O is IR-active. The target (N_2O) and interfering species (here H_2O, CO_2, and CO) concentrations are adjusted iteratively until the Root Mean Square (RMS) residual, i.e., the difference between the measured and simulated spectra, is minimized (Figure 2-17). The retrieval 'window' specific to the target gas (N_2O), i.e., an optimized subset of the broadband measured spectral range, was selected based on an early work test over August 2 to September 14, 2018 (50,000 individual observations) to account for many environmental conditions. In the 2018 data set, each spectrum is a one-minute average of 240 IR spectra acquired at 4 Hz over the broadband IR range of 500-5000 cm^{-1} (2-20 μm). In the 2020 data set, spectra were two-minute averages of 480 IR spectra, which resulted in improved spectral noise levels.

2.4.1. Retrieval window width

Early in the project, 2018 campaign data was used to compare the spectral fitting performance in a strong N_2O absorption band to that in two weak bands. The weaker bands were at 2400-2500 cm^{-1} and 2500-2600 cm^{-1}, as compared to the more standard window in the 2000-2200 cm^{-1} range. Initially it was thought that since the weak band had almost no interfering species the fits would perform better, but even though the RMS residual was low, the retrieved concentration of N_2O was unphysically high. The benefits of working with the strong band are a higher signal to noise ratio for the N_2O absorption features; the trade off is that interfering H_2O lines are always mis-fitted to an extent leading to systematic fit residual features.

Further studies were performed to determine the most optimal spectral interval of the strong band. Windows used in previous studies were compared to a working window previously used by our research group. One window, 2080-2270 cm^{-1}, was used in another OP-FTIR field study (Paton-Walsh et al., 2014). Another window, 2000-2240 cm^{-1}, was the result of a study that sought to optimize FTIR retrieval windows through an iterative approach (Esler et al., 2000). From this work it was understood that depending on path length, the optimal window width is affected by N_2O and interfering species absorption depth. In the strong N_2O band, selecting a window that is too wide results in too many absorption lines of CO_2 becoming saturated, which ill-conditions the spectroscopic retrievals due to signal levels dropping to zero. For H_2O and CO_2, it was also

found that selecting too narrow a window can reduce retrieval accuracy because of a lack of spectral features for the fit to work with. This information was used to select a window that had lines with 'good' signal levels for each species, without any saturation. An example of a fit using this optimized window is shown in Figure 2-17.

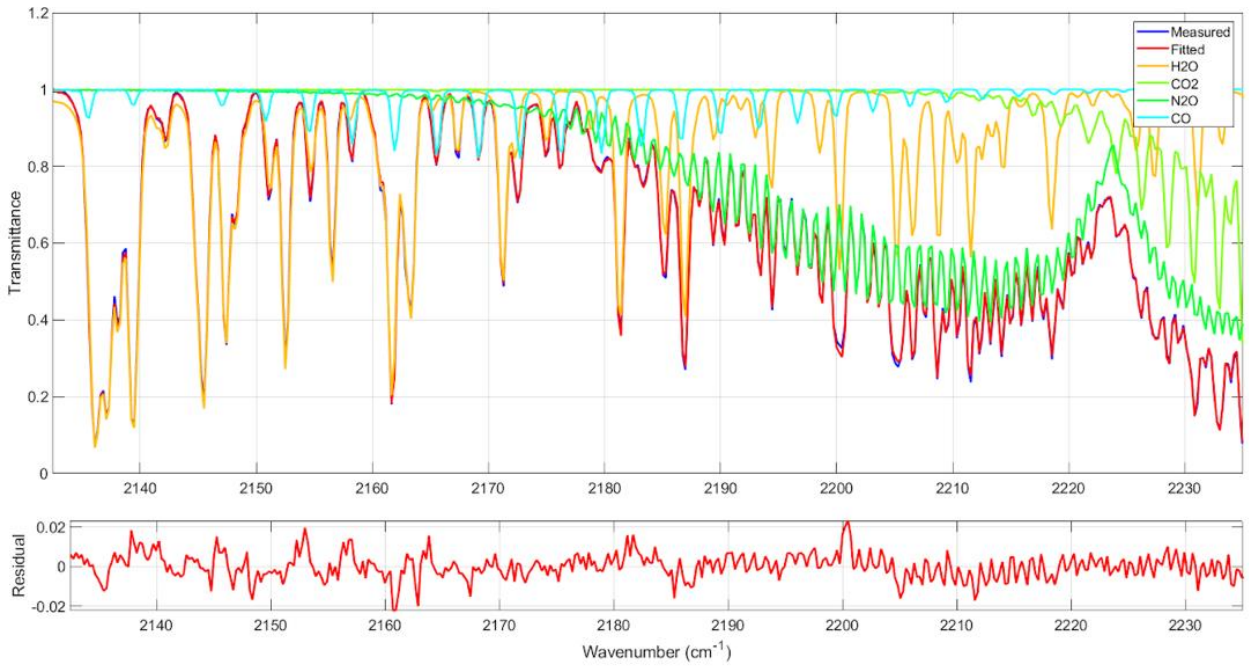

Figure 2-17: Top panel: An example of a 'retrieval' fit (red) in the optimized N_2O window of 2132.5-2235 cm^{-1}. The fit is the sum of component gas spectra. Bottom Panel: The residual is the difference between the fit and measurement. A single IR spectrum (1 min average of 240 spectra in 2018) provides one observation of the target gas concentration in the time series for the campaign.

With new 2020/2021 data, test retrievals on a short time period were again performed to compare 2018 and 2020/2021 retrieval results given that the measurement system had changed. Mainly, the difference during the 2020/2021 campaign was the use 50% larger retroflectors to reduce IR beam loss from divergence. During this process, the previously optimized spectral window was adjusted slightly in several tests to see if any further improvements could be made. 200 spectra were used from April 16th in the 2021 campaign and from October 3rd in the 2018 campaign, as these date ranges where the best match for temperature and relative humidity, which strongly influence the spectrum transmittance and fits. Fit RMS for N_2O retrievals in 2021 is half of what it was in 2018 due to the larger retroreflector arrays; this upgrade is described in detail by Power (2021), albeit for HCHO retrievals. Using the new 2021 data, starting from 2132.5 – 2235 cm^{-1} the window was extended, narrowed, and shifted to try to include or exclude line features to

improve the fit RMS residual value. The conclusion of this re-investigation was that the previously determined window was still optimal.

2.4.2. Interfering gas components and HITRAN 2016 spectral database

The modelled gas components in the retrieval of N_2O in the 2132.5 – 2235 cm^{-1} window are H_2O, CO_2, CO and N_2O. In 2021 it was timely to check if updating the molecule spectroscopic database used by MALT, which is the HITRAN database, improves fit performance. The wavenumber region surrounding our favoured windows was reviewed to see if any components were missed that might have newly added lines in the HITRAN database. Since the residuals of fits became less noisy from 2018 to 2021 (see previous section), there was now some new structure discernible in the 2021 residuals that may have been caused by another interfering species. Ozone (O_3) was added to the 200-spectrum ensemble of fits, but there was not enough O_3 absorption for a good fit (negative O_3 values were retrieved) and extending the window to try to cover more of the O_3 spectrum led to the need of introducing new interfering species with not enough absorption and thus diminishing returns in terms of retrieval accuracy and stability. Even though it adds more data, a wider window is not always better due to fitting challenges. A wider window made it harder to fit the continuum of the spectrum, which is the background variation of the 100% transmission level determined by the spectrometer optics.

The update to HITRAN 2016 spectroscopy (from 2012) was tested molecule by molecule using the same 200-spectrum ensemble from 2021 data as described above. The effect of the update of a single molecule on our fitting residuals was examined, and test retrievals were performed with various component combinations. The result of this analysis was that some molecules were updated while others were not. The principal interfering species H_2O and CO_2 were updated because there were clear and specific (physical) improvements to the fit. The update of H_2O resulted in changes to the residual of ~1% for some affected H_2O lines (Figure 2-18). The improvements in the fit due to updated lines of H_2O and CO_2 were above the instrumental SNR and resulted in an average improvement to the RMS residual of 7% across the 200-spectrum ensemble. The 2016 N_2O HITRAN update was a partial band update that gave poorer accuracy of fit due to the transition between the updated and not updated regions falling within our window. As such, the original 2012 N_2O spectroscopy was kept. For CO there was no change visible above noise, so the 2012 spectroscopy was kept. O_3 was tested but results included poor band coverage

and non-physical fits. The effect of updating O_3 on most of the residuals was close to the noise level and thus not significant enough for further investigation; in any case, O_3 was not included in the final component list.

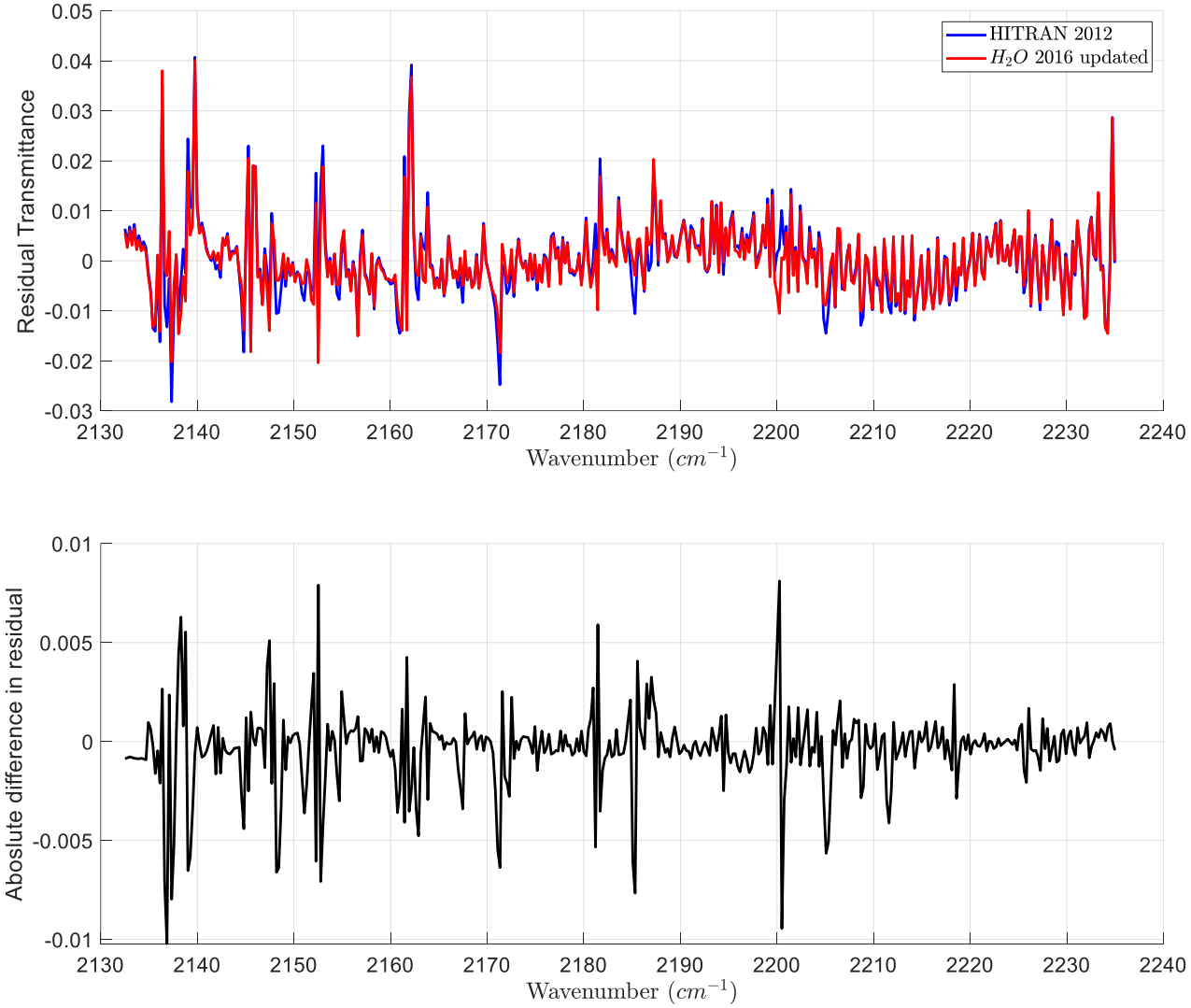

Figure 2-18: Top: The spectroscopic fit residual transmittance (for one example spectral fit) when using the HITRAN 2012 database (blue) for all gas components when substituting only H_2O from the HITRAN 2016 database (red). Bottom: The difference (2016 H_2O updated spectroscopy minus original 2012 spectroscopy) between the absolute values of the two residuals, where negative values are improvements to the fit. Many more H_2O lines are fit better than worse.

2.4.3. Fit residuals and data filtering

After the obvious failed fits due to missing or erroneous pressure and temperature inputs were removed (some due to the divergent T(z) calculation as described in Section 2.3.2), a general analysis of the quality of the retrievals was performed. Figure 2-19 shows the IR signal level (at 2500 cm^{-1}) vs. RMS residual "elbow" plot for the entire ensemble of 2020-2021 data, unfiltered with respect to L. This plot always takes the shape of an elbow, below which the signal becomes insufficient to allow MALT to converge on a solution; the RMS residual increases exponentially from this point, which can be considered a minimum viable signal value. The plot reveals a sharp drop off in fit quality below 0.1 (~10% of maximum signal at the beginning of the campaign). The elbow is also a logical place to set a threshold of acceptance for the RMS residual as well. Using this plot, the data was filtered for any observation where either of the observation paths (top or bottom) had RMS residual above 0.012. The elbow starts to bend gradually sooner but below RMS of 0.012 it makes more sense to use the signal level to make a cut and preserve more data. This information was used to create a selection (Figure 2-19 Region (A)) of acceptable data that satisfies an RMS residual < 0.012 (red line) and an IR signal > 0.1. Region (A) filters out 20% of the data set. The 'either' conditional when processing the two paths is important because the conditions can vary between the bottom or top path acquisition. This represents the greatest risk for false concentration differences (ΔC). There is a high tolerance in ΔC (since it is a subtraction) for varying conditions of both paths when in unison, however, if one individual path has severe and unique issues it can spuriously influence ΔC, i.e., not due to flux.

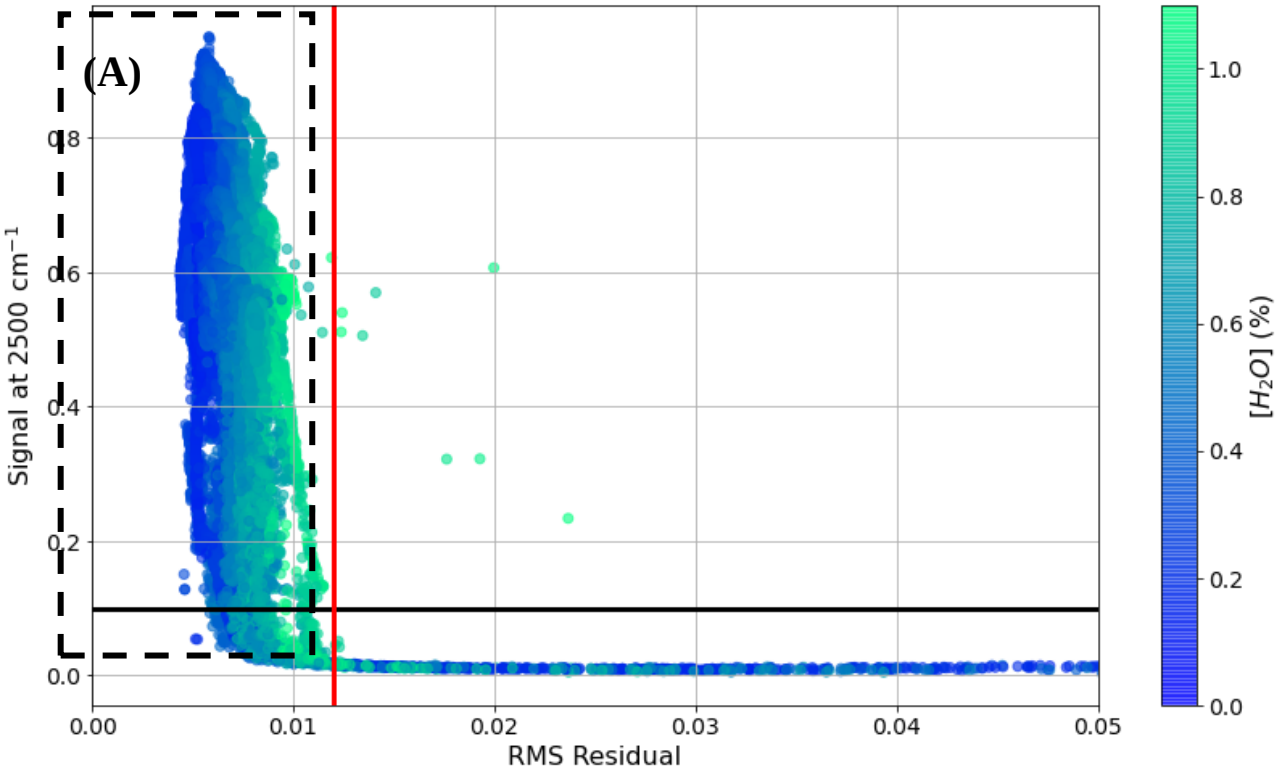

Figure 2-19: IR signal at 2500 cm^{-1} vs. the RMS residual. Acceptable data satisfies an RMS < 0.012 (red vertical line) and an IR signal > 0.1 (black horizontal line); this filtering forms the region in the dashed box (A). H_2O concentrations are shown with a colour bar since they tend to have a correlation with RMS residual values.

Figure 2-20 shows the individual N_2O concentrations with and without a filter applied to keep only observations where the signal is above 0.1 for both paths. Again the "both" is crucial as can be seen in the figure at the end of February (circled in red), where only one path is functioning and retrieving physically possible N_2O levels. The other path is retrieving unphysical values (<< 280 ppbv) because the signal is so low during this time. This was due of the bottom beam path being obstructed by snow. This would have created an enormous false signal in ΔC if it was not filtered out. While 0.1 looks slightly too conservative on this plot as it keeps noticeable dips in N_2O concentration, it is still in question weather some of those dips are physical, and, since both paths dip in unison, if the ΔC accuracy is affected. In Figure 2-19 above a signal of 0.1 does align with where RMS residual starts to noticeably decrease, so this is assumed to be a good starting point. As individual events of interest are examined, the logs and data quality for specific date ranges can be re-checked.

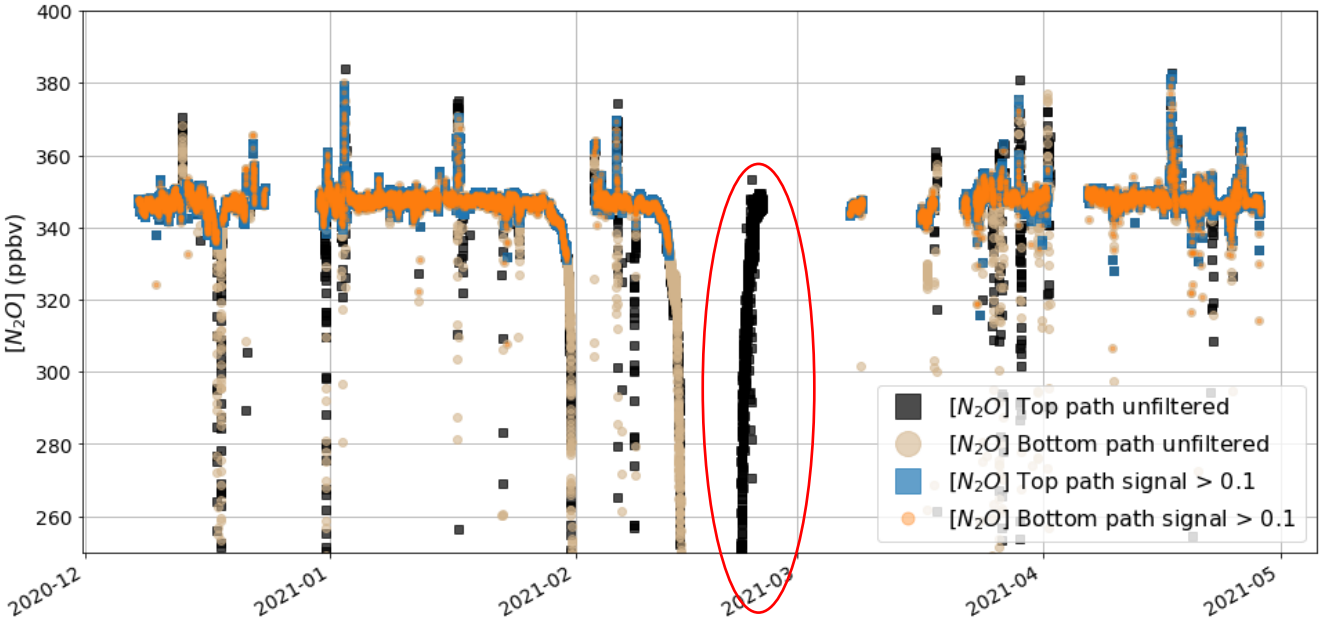

Figure 2-20: Black and tan show the unfiltered N_2O retrievals for top and bottom paths, respectively. Blue and orange (top and bottom) show only the data with IR signal > 0.1. Squares used for top paths and circles for bottom paths. Red oval highlights a region of interest where only the top path is functioning.

2.4.4. Retrieval input temperature sensitivity study

The 200 spectra from April 16th, 2021, used in other retrieval testing above where also used in an investigation of the sensitivity of ΔC to retrieval temperature error. The test spans from 12:00 pm April 16th to 4:00 am April 17th. The retrievals are steady for the majority of this time range, then starting at 2 am, they become very noisy, which gives a good variety of data to test on. The first test was to examine the effect of varying the temperature by increments of 1°C. For an individual retrieval this had the effect of misfitted lines in the retrieval window. The single-spectrum fit residual shown in Figure 2-21 changes for individual lines by ~5% per °C. The result of this on the ensemble of spectra, shown as a time series in Figure 2-22, is that the temperature offset appears to affect the concentration retrieved much like a constant offset. Therefore, if the temperature offset (or error) is in the same direction, e.g. positive temperature shift for both top and bottom paths in the experiment, the resulting offset in the retrieved N_2O concentration nearly cancels out in the concentration difference, ΔC, which is the value needed for flux. The calculated ΔC from retrievals varies by ~0.05 ppb for a 1°C temperature error. This is shown in Figure 2-23.

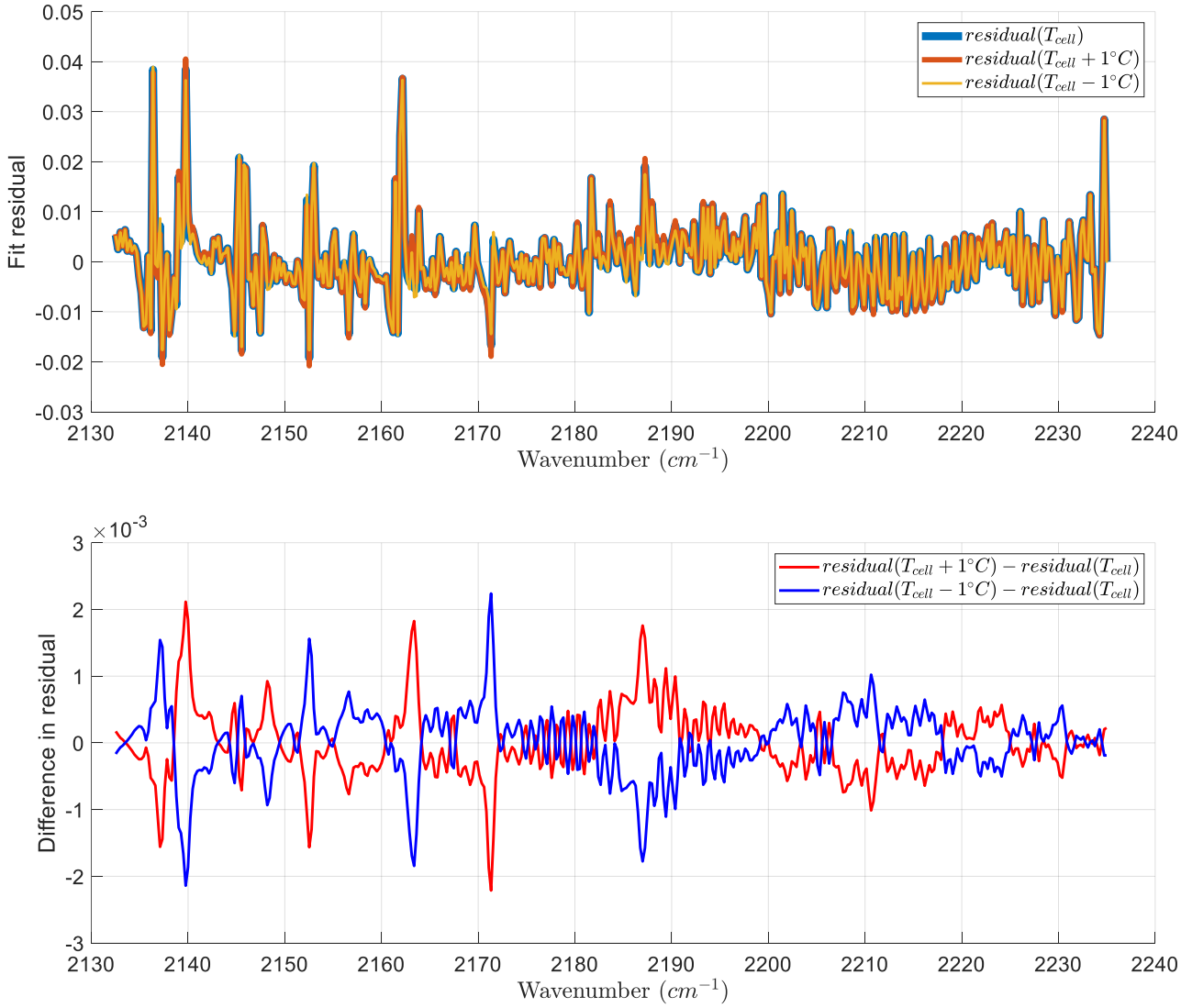

Figure 2-21: Top panel: Bottom path residual compared for a single fit during a steady period on April 16th, 2021. The fit used either T_{cell} as input temperature in the retrieval (blue), or T_{cell} + 1°C (red), or T_{cell} − 1°C (yellow). Bottom panel: Shows the differences between retrieval residuals to see the change in spectral line fits when using T_{cell} + 1°C (red) or T_{cell} − 1°C (blue).

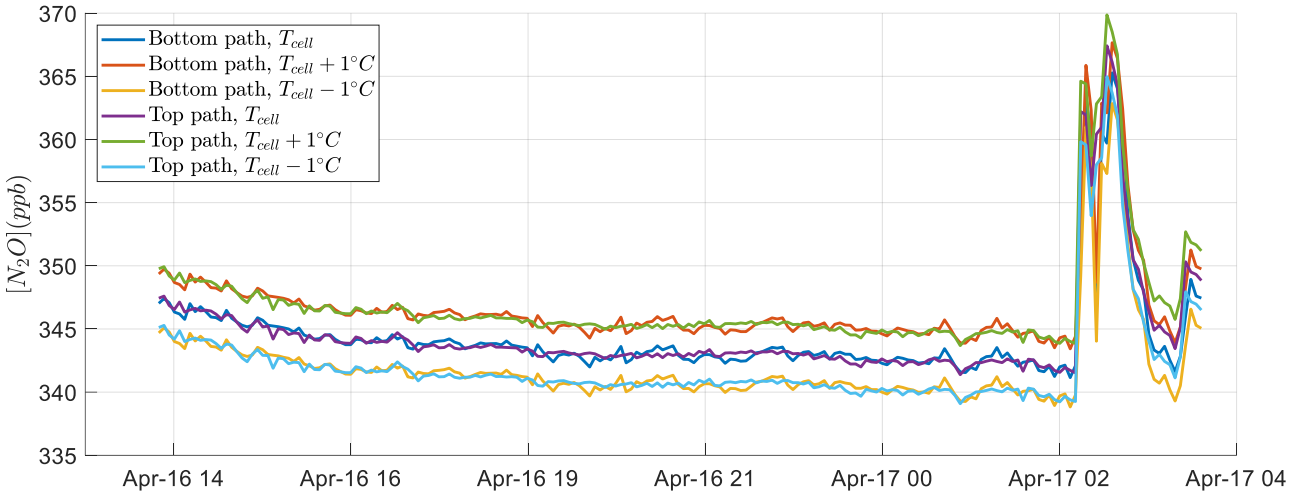

Figure 2-22: Time series of retrieved [N_2O] from 200 spectra during 12:00 pm April 16th to 4:00 am April 17th. Purple and blue: top and bottom path retrievals, respectively, using the temperature from the sample cell (T_{cell}). Green and red: top and bottom path retrievals using $T_{cell} + 1°C$. Cyan and yellow: top and bottom path retrievals using $T_{cell} - 1°C$.

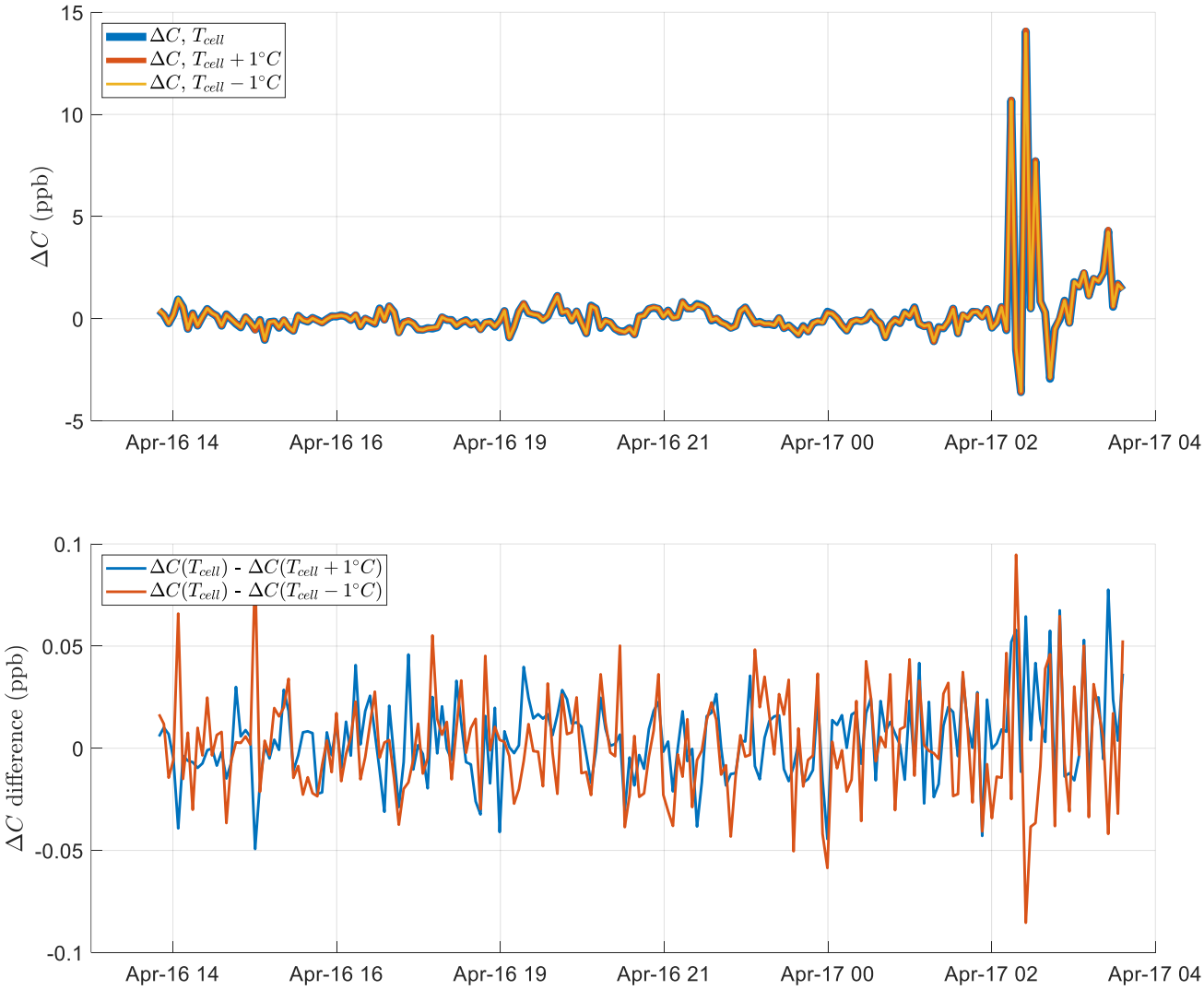

Figure 2-23: Top panel: ΔC calculated using [N_2O] from the three temperature test retrievals using T_{cell} as input temperature (blue), or T_{cell} + 1°C (red), or T_{cell} − 1°C (Yellow). Bottom panel: Difference between ΔC values when using T_{cell} − 1°C (red) or T_{cell} + 1°C (blue).

Test retrievals where also performed with the temperature offset applied asymmetrically. For example, using T_{cell} + 1°C for the top path and T_{cell} − 1°C for the bottom path. The resulting time series of ΔC are shown in Figure 2-24. This results in a 5 ppb error in ΔC and represents the worst-case scenario wherein temperature errors are asymmetric for the top and bottom retrievals. This is a large enough error to potentially change the sign of the calculated flux. However, this scenario seems unlikely since the instrumental bias should be very similar for temperature observations taken with the same instrument within 2 minutes of each other (which for Ts is an

average of 1200 samples). The same process was repeated for an asymmetric offset of $\pm 0.05°C$, which is on the order of the mean temperature difference between the $T(z_{bottom})$ and $T(z_{top})$ temperature profile calculations for the full campaign period (see Section 2.3.2). The result of that test is shown in Figure 2-25 where the error in ΔC is approximately 0.24 ppb. Further results looking at the error in ΔC but using the retrieved values for the full observation period are examined in Section 3.2.

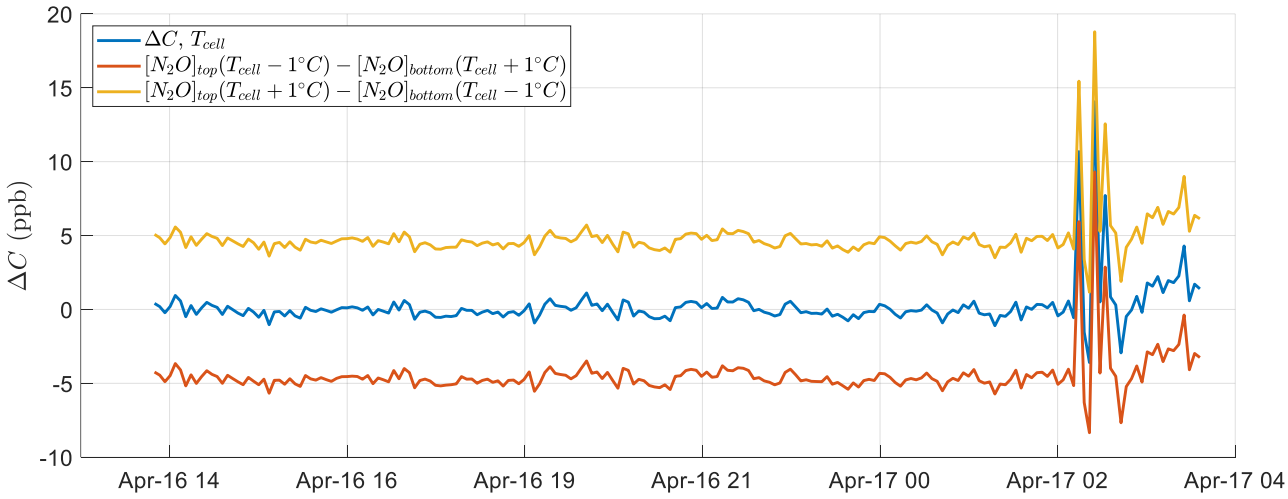

Figure 2-24: ΔC calculated using $[N_2O]$ from the three test retrievals with temperature offsets. Blue: Retrieval used T_{cell} for both paths as input temperatures. Red: Retrieval used asymmetric temperature perturbations with $T_{cell} + 1°C$ used for the top path and $T_{cell} - 1°C$ used for the bottom path. Yellow: Retrieval used the opposite temperature perturbations, with $T_{cell} - 1°C$ used for the top path and $T_{cell} + 1°C$ used for the bottom path.

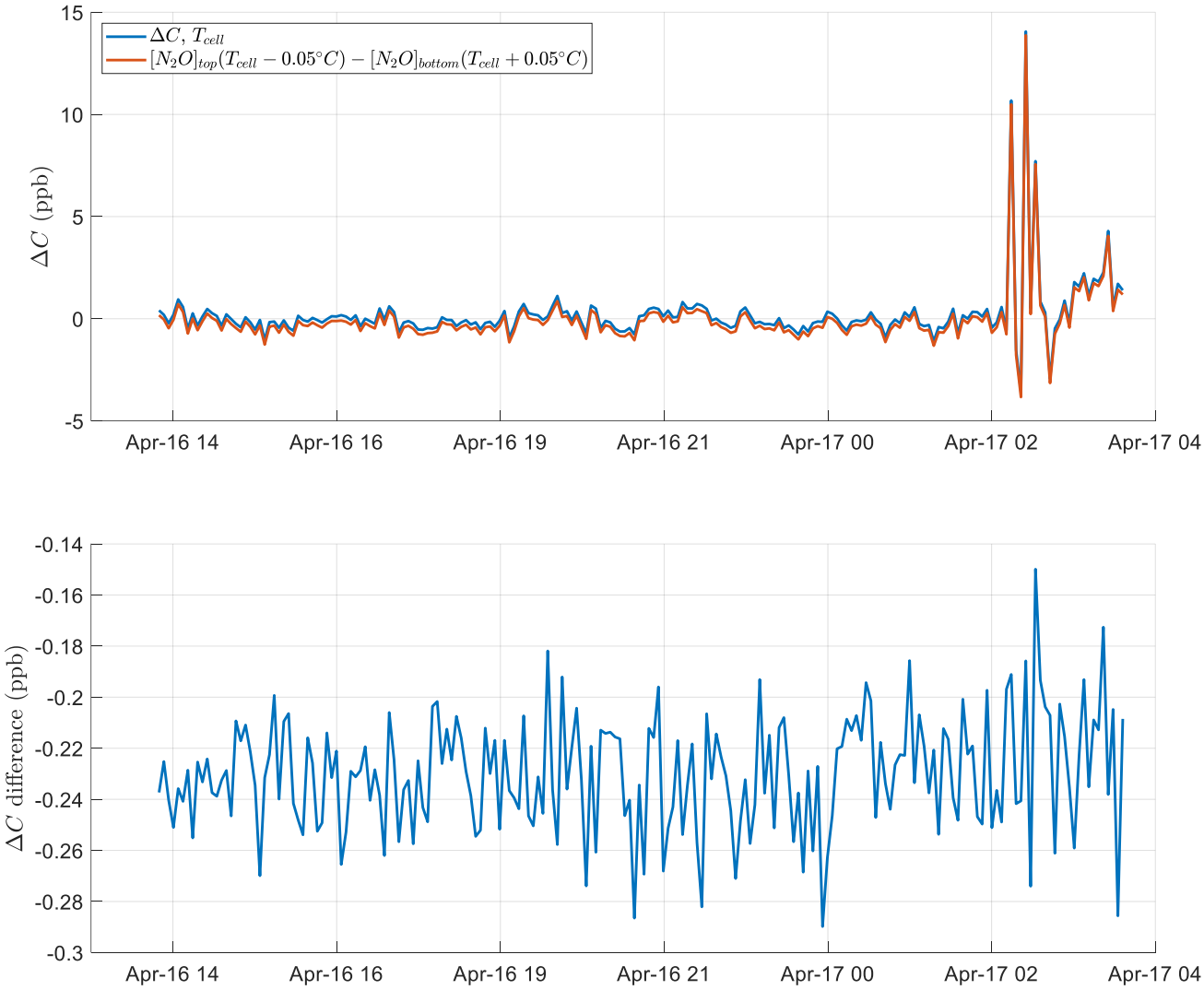

Figure 2-25: Top panel: ΔC calculated using [N_2O] from the test retrievals with input temperature incremented by 0.05°C. Blue: Retrieval used T_{cell} for both paths as input temperatures. Red: retrieval used asymmetric temperature perturbation with $T_{cell} - 0.05°C$ used for the top path and $T_{cell} + 0.05°C$ used for the bottom path. Bottom panel: Difference between ΔC caused by the asymmetrical input temperature error.

2.4.5. Dry mixing ratio correction

The flux calculation of Flesch et al. (2016) requires ΔC to be in the form of a dry mixing ratio. Starting from the N_2O concentration, C_{N_2O}, retrieved from FTIR observations in units of ppb, the dry mixing ratio is found as follows,

Equation 10 $$C_{N_2O,\,dry} = \frac{1x10^{-9}(C_{N_2O})}{1-1x10^{-2}(C_{H_2O})},$$

where C_{H_2O} is the concentration of H_2O retrieved from FTIR observations in units of percent. The correction from wet to dry mixing ratio results in a mean change of 1.7 ppb to a path-average N_2O concentration. This is a 0.49% change, which is equal to the mean H_2O concentration retrieved. The mean change in ΔC between the two paths is 0.01 ppb (mean difference is 0.17 ppb) so the impact of not making the correction is a 6% error in this data set.

3. Results and Discussion

3.1. Wind flow characteristics

Figure 3-1 shows the wind roses for the entire measurement period (December 2020 to April 2021) from the 3-D sonic anemometer and a nearby weather station (Shearwater jetty, 6 km away see Figure 1-5). It is encouraging to see good agreement in the prominent wind direction. Shearwater jetty is in a similar topography as our site: a shoreline location with nearby MacNab's Island forming a channel with the mainland. The main difference at our study location is that the Halifax peninsula and Dartmouth waterfronts have a steeper elevation rise compared to the Shearwater area, together with taller buildings along the shoreline. This seems to block the flow of W-SW winds and possibly E-NE winds as well. The dominant and strongest winds at the Jetty were in the expected direction based on the water channel orientation, with 40% of data points showing wind direction as N-NW, which is also the direction of the fastest wind speeds. This was all the more expected since the channel opens to the Bedford Basin on this side (large open body of water). This is consistent with the exploratory work with 2018 wind data shown in Section 2.3.3. The instrument footprint that the sonic anemometer is measuring largely comes from over the water surface and travels parallel to the jetty obstruction, reinforcing the validity of the micrometeorological assumptions in this work.


3-D Sonic Jetty 5.2 meters ASL
N
N-E
E
S-E
S
S-W
W
N-W
19.8
15.8
11.9
7.9
4.0
Dartmouth
Halifax
Shearwater Jetty 5.5 meters ASL
17.9
14.3
10.7
7.2
3.6
Shearwater

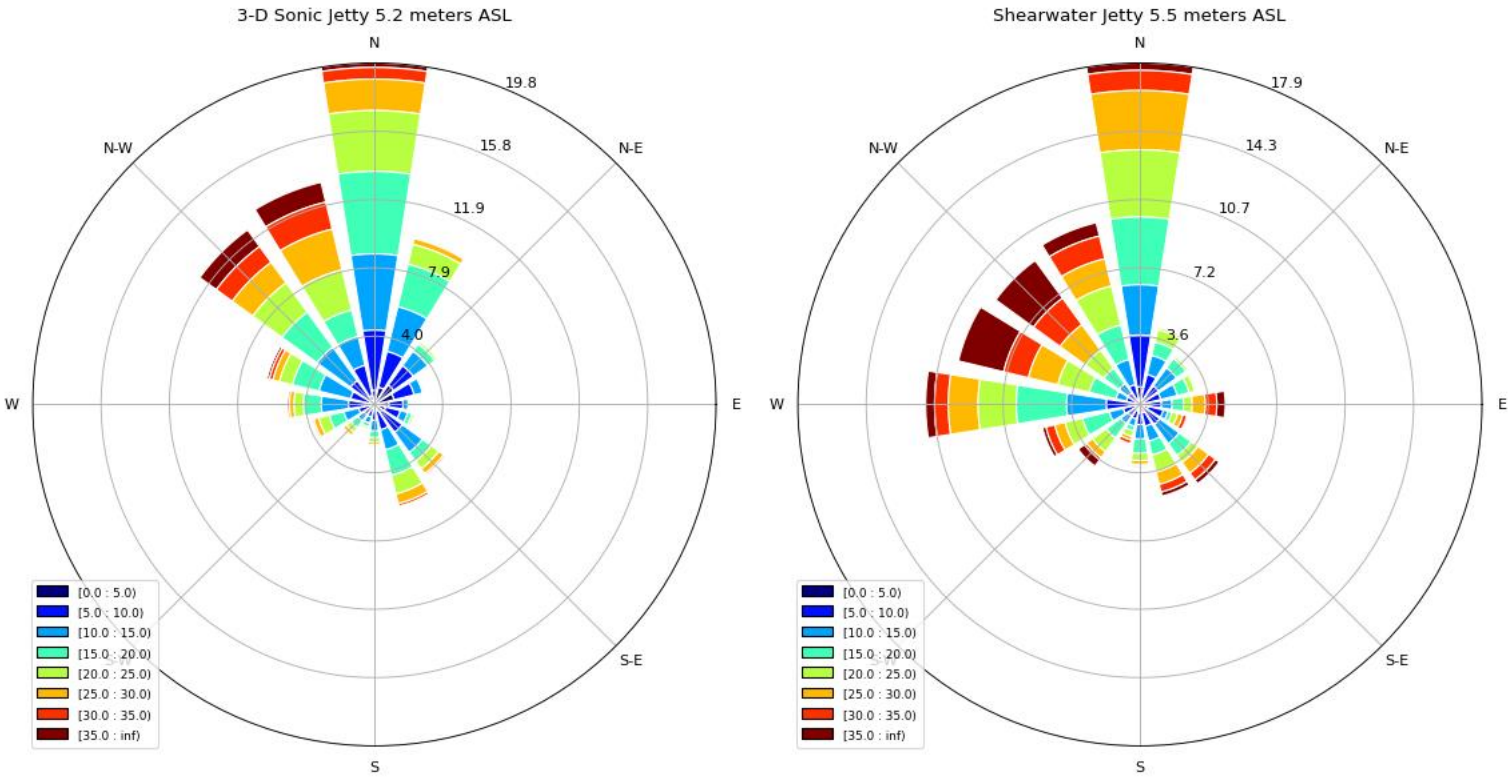

Figure 3-1: Previous Page Map: Wind roses for two weather stations from December 2020 to April 2021, overlaid on geographic locations of stations. Bottom Panel: Wind roses enlarged. Left: 3-D sonic Jetty at study location (elevation above mean sea level = 5.2 m) Right: Shearwater Jetty (elevation above mean sea level = 5.5 m). Percent distribution is shown radially, angle represents wind direction and colour represents wind speed in km/h.

3.2. Retrieved concentration difference

3.2.1. Concentration difference characteristics

The concentration difference between the top and bottom OP-FTIR path measurements, ($\Delta C = C_{top} - C_{bottom}$) was used in the calculation of the concentration gradient. Table 6 and Figure 3-2 show the complete statistics for the concentration difference, ΔC, after merging data sets and applying the filtering process described in Chapter 2. After filtering, the data set still contained a single ΔC observation that is certainly an outlier with a value of -141 ppb. The next lowest minimum value is -23.6 ppb. The single remaining outlier was removed and the fact that there was only one is a good indicator that the previous filtering was optimal. Figure 3-3 shows the concentration differences ΔC over two days in January with three observation time lengths: the finest timescale possible (4m 19s), 30 min averaging bins, and a 3-hour moving average. The sonic

data is merged with the FTIR data where one observation (top and bottom paths) requires 4 minutes and 19 seconds. The uncertainty in ΔC is calculated below (Section 3.3.1) as part of the process of calculating flux, also using results from Sections 3.2.2 and 3.2.3, presented next. Uncertainty becomes a greater concern when the error bars cross $\Delta C = 0$, as this means that the sign of the resulting flux is uncertain. Figure 3-4 shows the distribution of the ratio between ΔC and the uncertainty in ΔC. This ratio is >1 for 48% of the data set, meaning that the flux signal for those observations is not clearly in or out of the ocean. That percentage improves for the 30-minute bins, which is shown in Section 3.3 for final flux results.

Table 6: Complete statistics for the concentration difference, ΔC, of N_2O (dry mixing ratio difference in ppb) after merging FTRI and sonic data sets and filtering for outliers. December 2020 to April 2021.

Observation count	25768
Mean	0.17
Standard deviation	1.09
Standard error (SE)	0.0068
Minimum	-23.43
25^{th} percentile	-0.29
50^{th} percentile (Median)	0.13
75^{th} percentile	0.56
Maximum	39.4

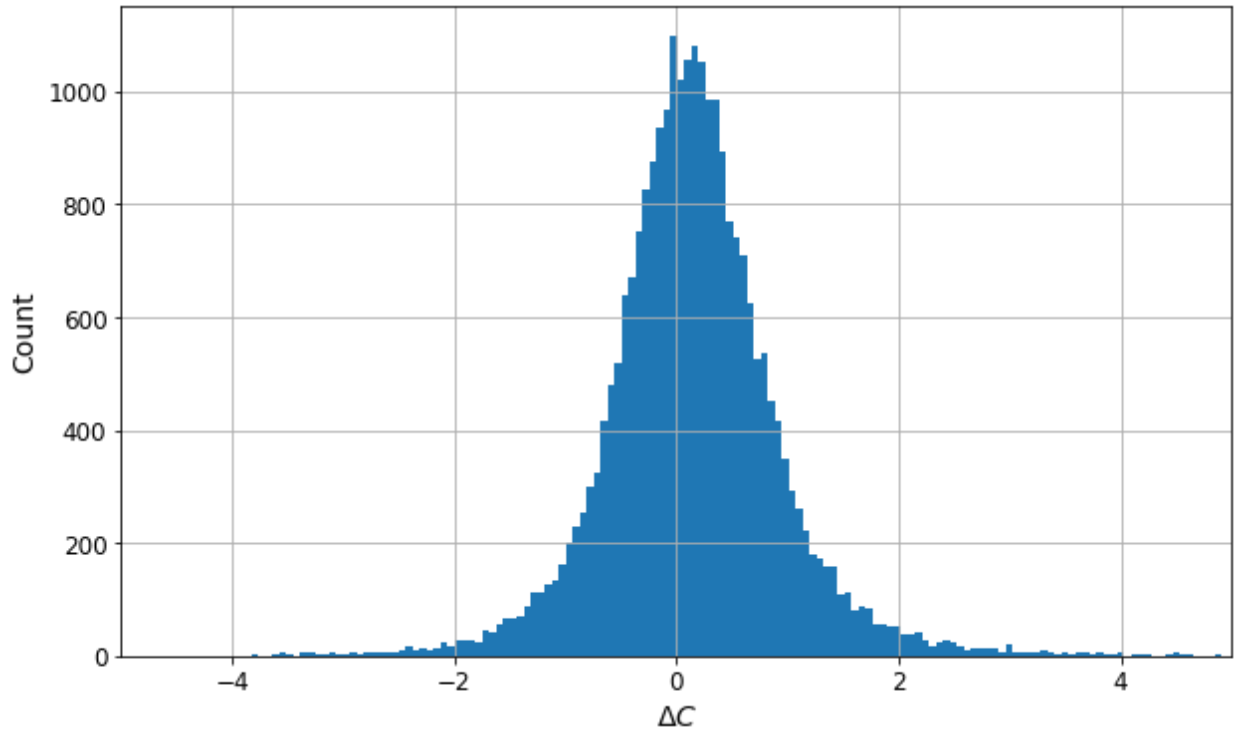

Figure 3-2: Histogram of the concentration difference, ΔC, of N_2O (dry mixing ratio difference in ppb). December 2020 to April 2021.

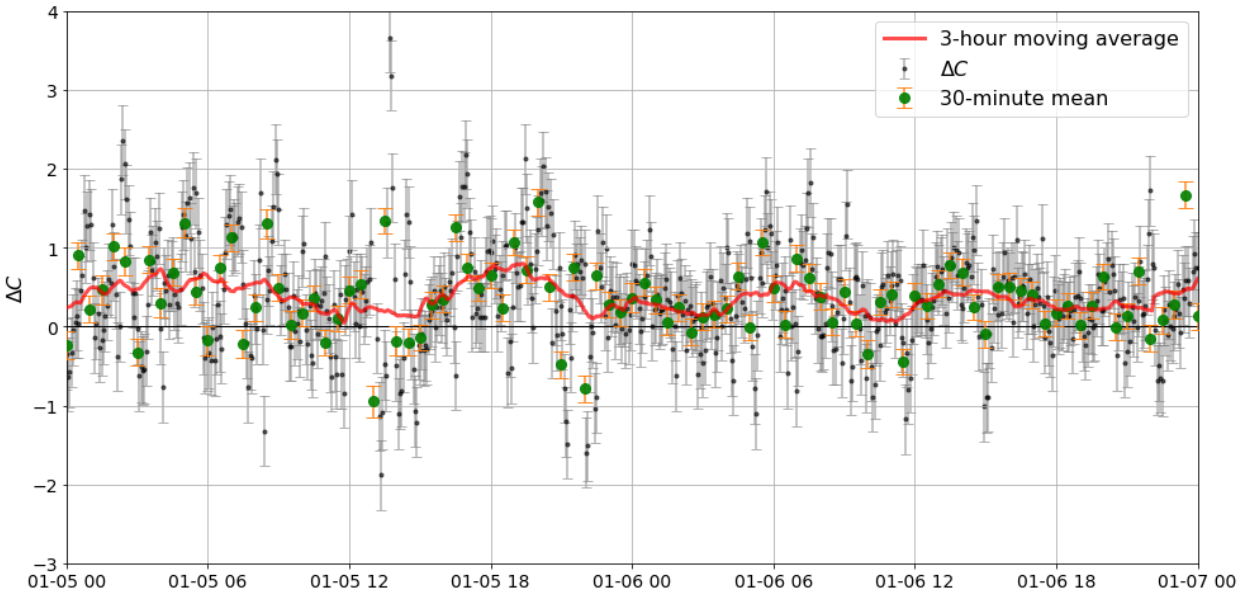

Figure 3-3: Concentration difference, ΔC, of N_2O (dry mixing ratio difference in ppb) from January 5th to 7th. Black: finest acquisition timescale of 4 m 19 s. Green: 30-minute averaging bins. Red line: 3-hour moving average.

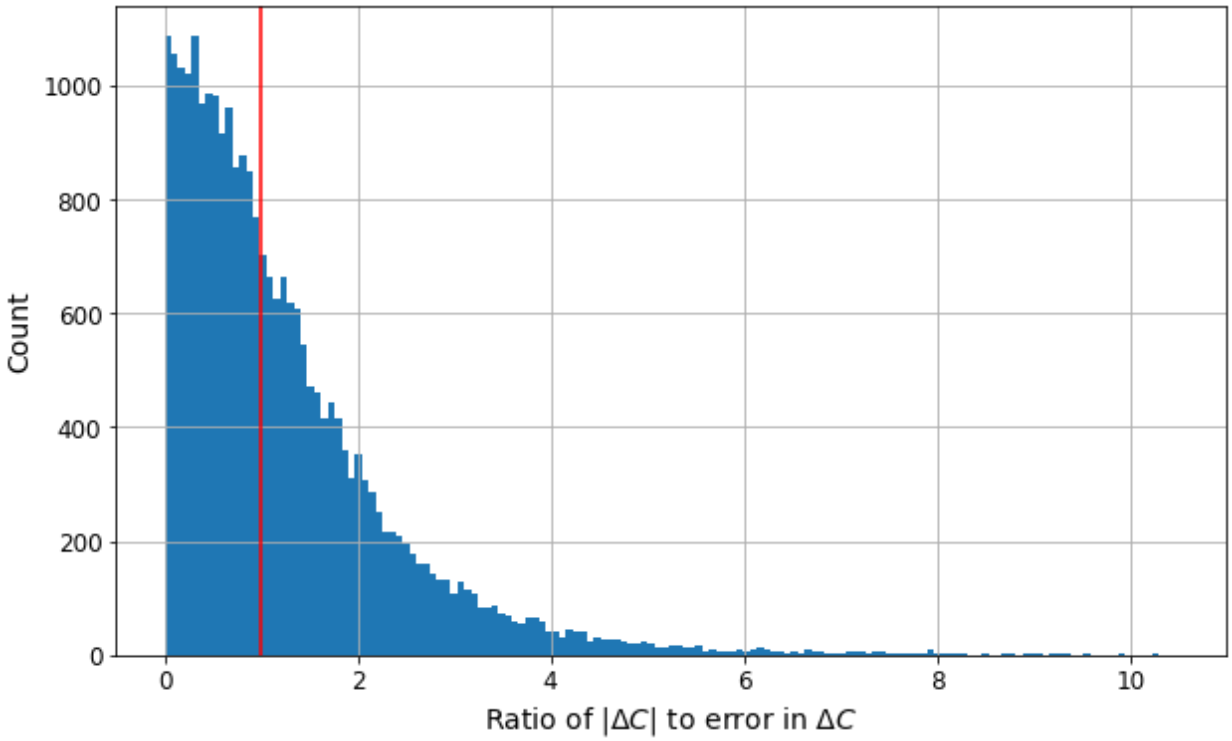

Figure 3-4: distribution of the ratio between ΔC and the error in ΔC (dry concentrations of N_2O). Data to the right of x=1 (red line) has smaller error than the observed magnitude of ΔC.

3.2.2. Variance of retrieved concentration

The variance of the retrieved concentration, σ_C, is used in flux uncertainty calculations to represent the random error of the OP-FTIR instrument and spectroscopic retrieval. Bai et al. (2011) have reported a variance of 0.3 ppb, whereas Flesch et al. (2016) used 0.4 ppb in their calculations. To get a comparison for σ_C from the Halifax Harbour campaign a 4-hour section of data with good signal levels and a smooth time variation was used to find the root mean square error (RMSE) to a best fit curve (2^{nd} degree polynomial fit). This analysis assumes the concentration is not erratic (smooth curve) so that the RMSE approximates σ_C. However, the RMSE is a result of instrumental noise as well as changes in concentration due to environmental factors, such as wind speed; therefore, σ_C is likely smaller than the RMSE. Figure 3-5 shows the section and fit for spectra from the top path, for which the resulting RMSE was found to be 0.26 ppb. Therefore, under good

observation conditions our system can retrieve concentrations with similar noise as was observed in Bai et al. (2011). However, Figure 3-6 shows the same 4-hour section for the bottom path spectra where the RMSE was found to be 0.74 ppb, which is higher than the value used by Flesch et al. (2016). The bottom path is closer to the ground/water and is expected to be less precise because of the lower signal return from an array with more wear and tear, as well as possibly due to increased air scintillation effects (as observed by viewing the scene through the system telescope). These sections on January 1st, 2021, are during a time of excellent (campaign high) signal level (arbitrary IR signal intensity 0.87 – 1.08), and it was assumed that the random noise would be greater at lower IR signal levels, but, as shown below in Figure 3-7 and Figure 3-8, that is not necessarily the case.

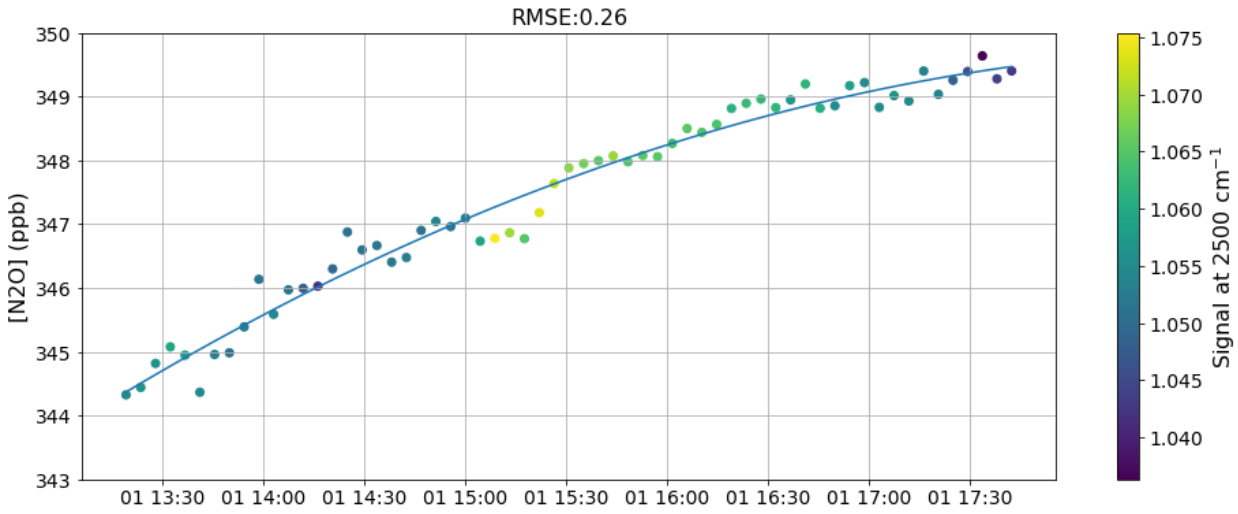

Figure 3-5: Retrieved concentration from top path spectra on Jan 1st, 2021. Blue line: Best fit polynomial with RMSE = 0.26 ppb. Colour bar: IR signal at peak of 2500 cm^{-1}.

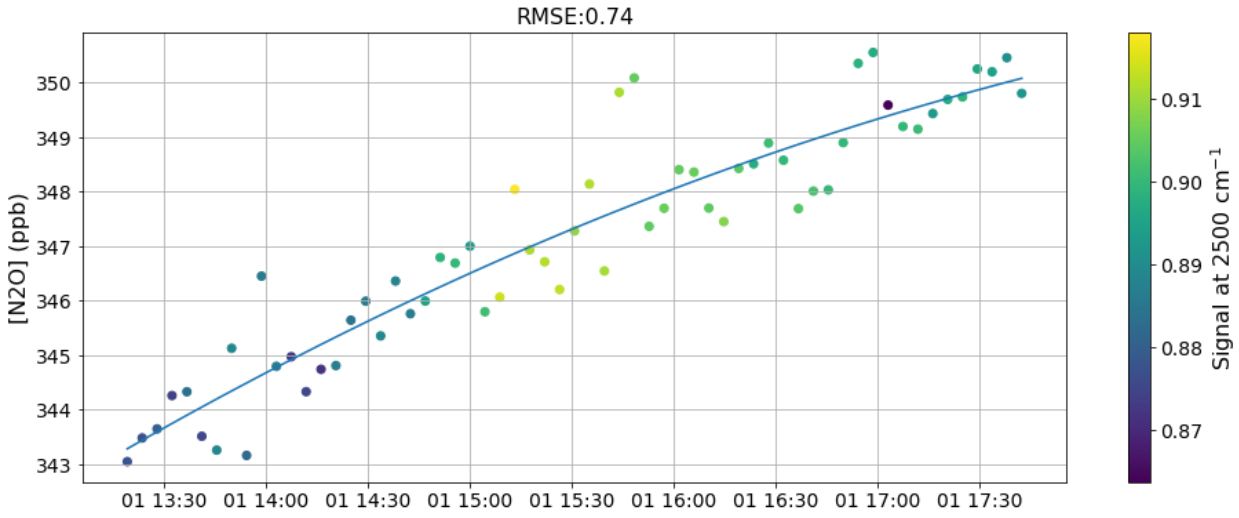

Figure 3-6: Retrieved concentration from bottom path spectra on Jan 1st, 2021. Blue line: Best fit polynomial with RMSE = 0.74 ppb. Colour bar: IR signal at peak of 2500 cm^{-1}.

The RMSE analysis was performed for a longer period of 12 hours on April 26th, 2021, near the end of the experiment. The signal level is now half that of the January time period used above, as cube corner coatings degraded and became coated with salt. Figure 3-7 shows the results for the top path. The RMSE was found to be 0.19 ppb, which was the best found during this analysis. Figure 3-8 is the result for the bottom path using the same time range, where the RMSE was found to be 0.25 ppb. These values were used as spot checks to determine that it is reasonable to use a variance of $\sigma_C = 0.3$ ppb as reported in Bai et al. (2011). It also shows that σ_C is not adversely influenced by IR signal levels (> 0.1) in our experiment, most likely because N_2O absorptions are still deep compared to instrumental noise levels, which matters most for the retrieval.

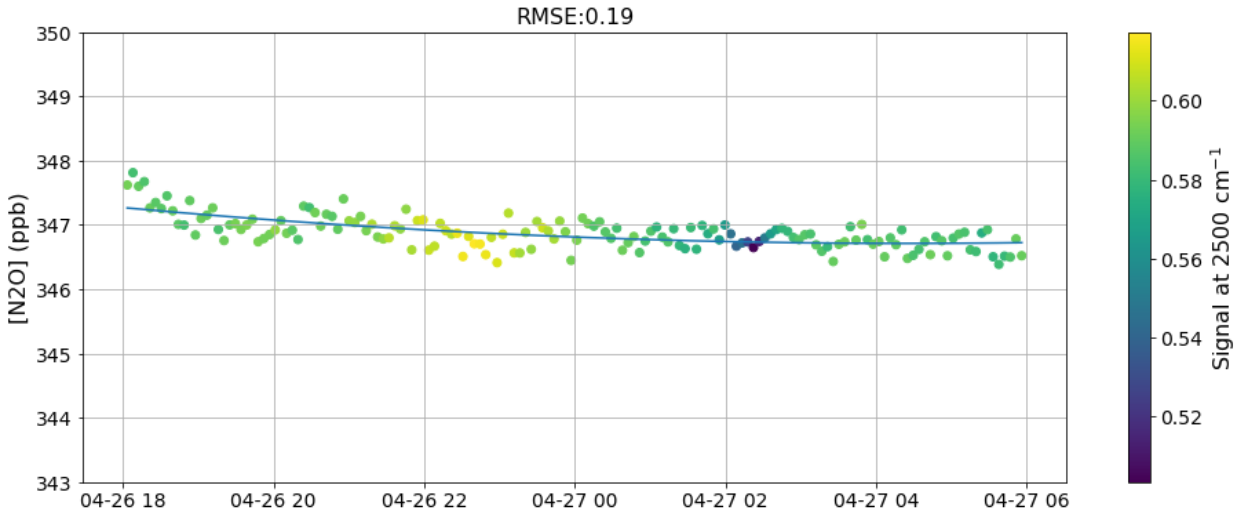

Figure 3-7: Retrieved concentration from top path spectra on April 26th, 2021. Blue line: Best fit polynomial with RMSE = 0.18 ppb. Colour Bar: IR signal at peak of 2500 cm^{-1}.

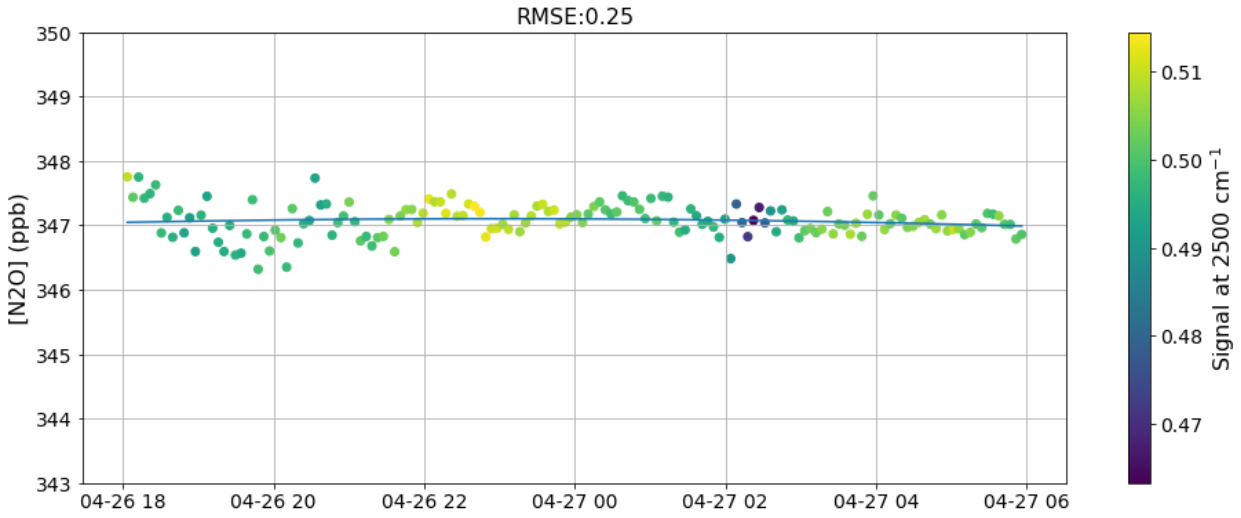

Figure 3-8: Retrieved concentration from bottom path spectra on April 26th, 2021. Blue line: Best fit polynomial with RMSE = 0.24 ppb. Colour Bar: IR signal at peak of 2500 cm^{-1}.

3.2.3. Sensitivity of concentrations to retrieval temperature differences

The sensitivity analysis of Section 2.4.4 showed, based on a selection of 200 spectra, the impact of arbitrarily imposed 1℃ retrieval temperature errors on retrieved concentrations and concentration differences. Now, based on data for the entirety of the 2020/2021 campaign, and utilizing temperature inputs from two separate instruments, the sensitivity of concentrations to temperature is empirically characterized. More specifically, the error in the concentration

difference, ΔC, due a 1℃ error in the temperature input used in the retrieval process is estimated from a large ensemble of real-world data, as described below. It is important to characterize the error in ΔC and not just in individual single-path concentrations, because as seen in both simulation and real-world data, these error values are quite different.

N_2O concentration retrievals were performed with temperature inputs from two instruments at the sonic anemometer site. First, a single temperature (T_{cell}) from the sonic's IR gas analyzer sample cell was used to retrieve *both* top and bottom path concentrations. Then, a separate retrieval was performed using two different temperatures, corresponding to the average height of the top and bottom beam paths ($T(z_{top})$, $T(z_{bot})$), respectively. These temperatures at heights z_{top} and z_{bot} were calculated using the vertical temperature profile derived from the 3-D sonic anemometer data. In comparing the retrieval results that used these different temperature inputs it was found that the retrieved concentrations differed little for a given path. The mean difference between concentrations retrieved for the top path using T_{cell} versus $T(z_{top})$ was ~1 ppb (~0.3% for N_2O). For the two retrieval configurations using different temperature inputs, the mean difference in ΔC is calculated as

$$[d\Delta C]_{mean} = \left[N_2O_{top}(T_{cell}) - N_2O_{bot}(T_{cell})\right]_{mean} - \left[N_2O_{top}\left(T(z_{top})\right) - N_2O_{bot}(T(z_{bot}))\right]_{mean},$$

and is equal to only 0.03 ppb. Thus, the top path concentration error of ~1ppb seems partially cancelled out by the subtraction of a similarly altered bottom path concentration in order to calculate ΔC. The RMS residuals of the spectral fits also show that MALT did not struggle to compute the retrievals with different temperature inputs, which could be the case if input temperatures were non-representative of true environmental conditions. The mean RMS residual for all the fits of top path spectra using $T(z_{top})$ was 0.006765 (0.6%), while using T_{cell} the mean RMS residual of the top path spectra only differed by 0.000041 (0.0041%), or a 0.6% difference. Similar small differences were found for the bottom path spectral retrievals using T_{cell} and $T(z_{bot})$.

The sensitivity of the retrieved concentration difference to retrieval input temperature, $d\Delta C/dT$, is needed to calculate the uncertainty in flux; the two retrievals using different input temperatures were used to estimate this. First, we examine single path concentration temperature sensitivity, dC/dT. Starting with the top path, $T(z_{top})$ was subtracted from T_{cell} to calculate the

input temperature differences (dT), here standing in for a true error in input temperature. The full (but filtered) measurement period covers a large real-world sample set and the temperature differences in the two retrieval inputs span a wide range with the majority falling between -8℃ and 5℃. The differences between the retrieved concentrations, dC, due to the input temperature differences ranged around -20 ppb to 20 ppb. Figure 3-9 shows dC plotted against dT with a linear fit used to determine $dC/dT = 2.21$. Figure 3-10 shows the same analysis but for the bottom path where $dC/dT = 2.22$. Therefore, a 1℃ error in temperature is estimated to cause an error of 2.22 ppb in retrieved N_2O concentration. The average N_2O concentration retrieved during the measurement period was 346 ppb, therefore the percent error due to a 1℃ error in temperature is estimated as 0.6%.

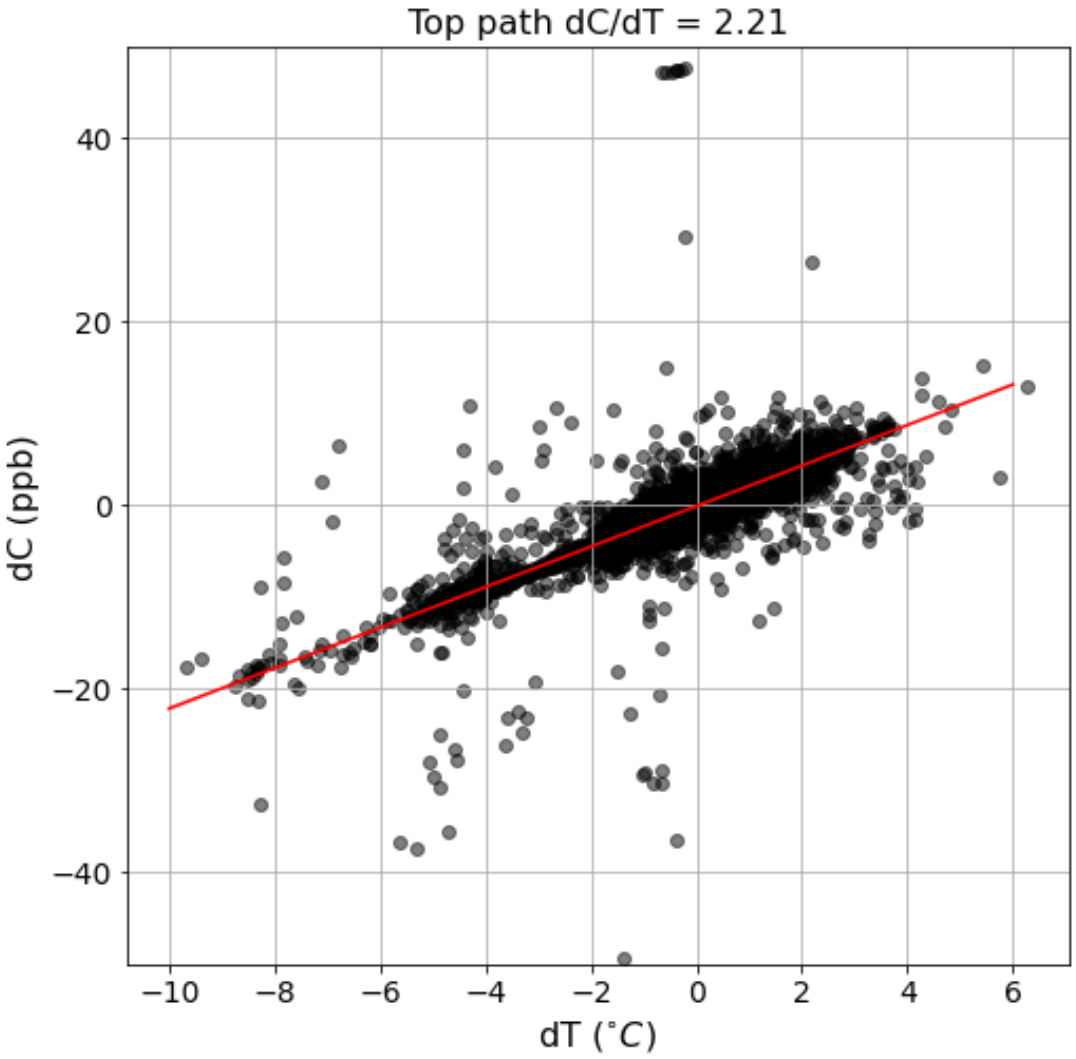

Figure 3-9: dC, the difference in retrieved concentrations of N_2O resulting from two unique input temperatures differing by dT, plotted against dT. Top path spectra analysed for the full measurement period from December 2020 to April 2021 (25768 data points).

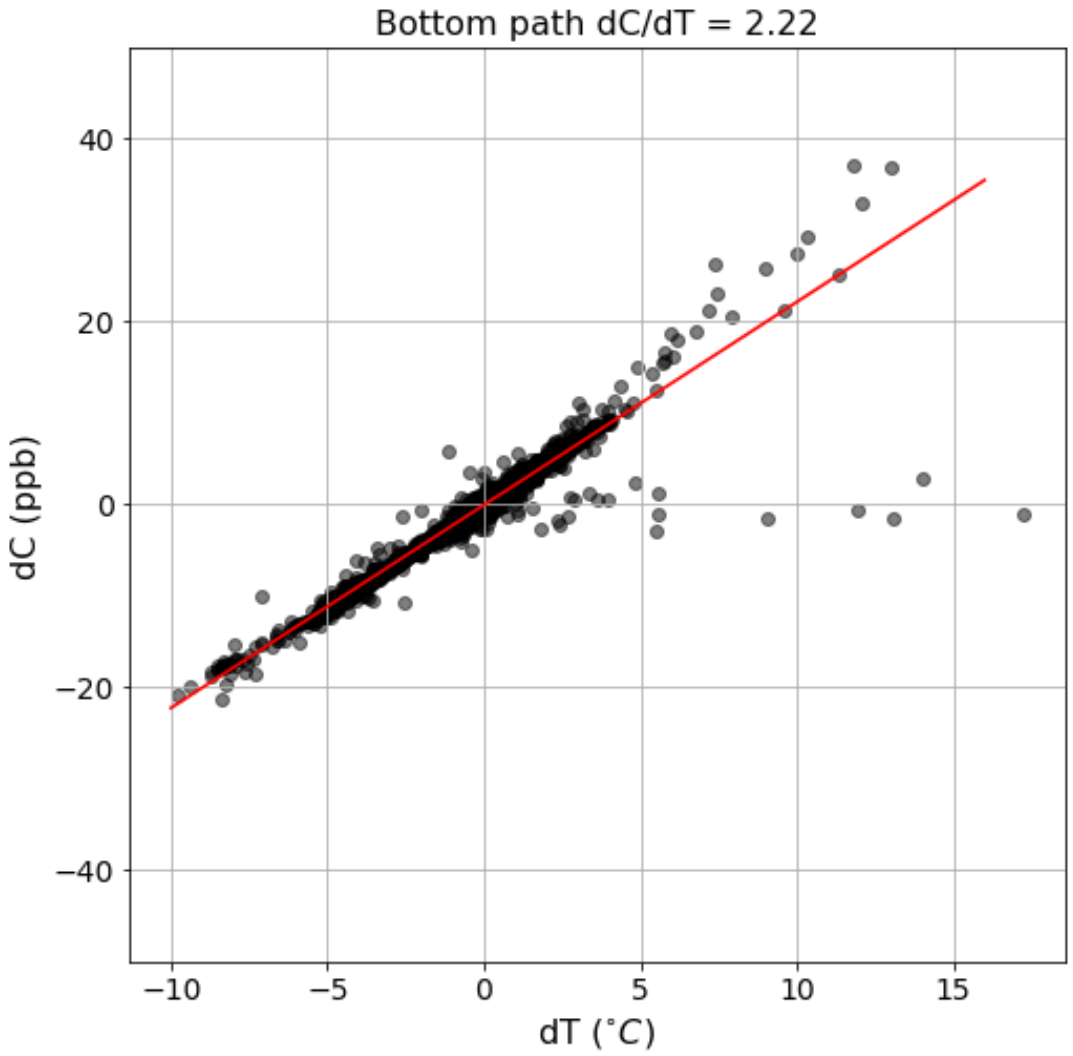

Figure 3-10: dC, the difference in retrieved concentrations of N_2O resulting from two unique input temperatures differing by dT, plotted against dT. Bottom path spectra analysed for the full measurement period from December 2020 to April 2021 (25768 data points).

MALT simulations showed that for a concentration difference, ΔC, the error due to temperature depends on whether the temperature error for the two paths is in the same or opposite directions from a 'true' temperature. A systematic instrumental error that results in both top and bottom path input temperatures being 1 ℃ higher than the true value has little to no effect on ΔC, while a source of error (either systematic or random) that stretches or compresses the temperature gradient will affect ΔC significantly, and even has the potential to change the sign of the calculated flux. To estimate the real-world effect of this in the field, $d\Delta C/dT$ was examined for the two

different but reasonable retrieval input temperatures. Figure 3-11 shows the change in ΔC when using the two different temperature inputs. For dT in this case the average path height temperature of the $T(z_{top})$ and $T(z_{bot})$ was subtracted from T_{cell}. The slope is $d\Delta C/dT = 0.16$, which is 10-fold smaller then dC/dT; however, typical measured values of ΔC are also much smaller than single concentrations ($\Delta C_{mean} = 0.17$ ppb while $N_2O_{mean} = 346$ ppb). The difference in retrieved ΔC can reach ~20-40 ppb, however, for 80% of the data the change to ΔC is less than 0.7 ppb and the mean change in ΔC is 0.06 ppb. Since u* is a key component in determining the T(z) profile, it will contribute to errors in T(z) and hence dT; u* is plotted in colour in Figure 3-11 and shows some weak correlation with dT, but does not show any obvious correlation with $d\Delta C$. It is unclear yet what is causing the occasional extreme effects on $d\Delta C$ in this large ensemble retrieval input temperature test. Some of the higher $d\Delta C$ values coincide with a larger temperature difference between z_{top} and z_{bot} as shown in Figure 3-12. For some $d\Delta C$ values of ~40 ppb, the difference between fit RMS residual from the two methods is higher than usual, which is shown in Figure 3-13. This could be the case of those rare MALT retrievals that do not fit correctly due to some secondary effect of temperature in the fitting process, via spectral temperature dependencies. In the uncertainty analysis and calculations that follow, the value of $d\Delta C/dT = 0.16$ ppb/℃ will be used (Section 3.3.1). The absolute value of ΔC was measured as 0.08-1.26 ppb (10^{th} and 90^{th} percentiles, respectively). Therefore, for every 1℃ error in input temperature the error in ΔC is estimated as 13-207% for 80% of the data. This seems very high; however, this value is multiplied in the flux uncertainty equation by variance in the temperature measurement, which is usually small (0.1~0.2 ℃ as expected from the moist lapse rate over a small height range). A histogram of the ratio $d\Delta C/dT$ is shown in Figure 3-14 with a peak value at 0.09 ppb/℃, while the median of $d\Delta C/dT$ is 0.11 ppb/℃, which makes the fitted value of 0.16 ppb/℃ be a conservative first approximation of the sensitivity of concentration differences to temperature errors.

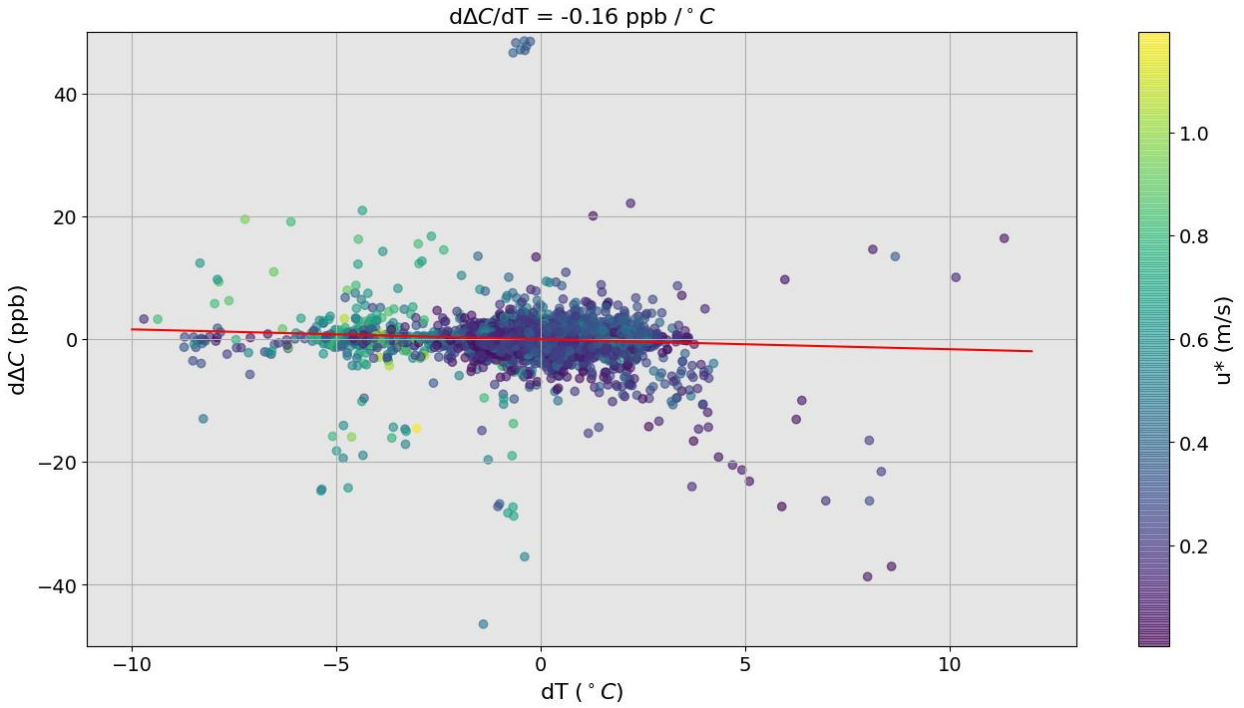

Figure 3-11: The change in ΔC (dΔC) when using two different retrieval temperature inputs. For dT the average path height temperature of $T(z_{top})$ and $T(z_{bot})$ was subtracted from T_{cell}. Displayed in colour is u* which has some correlation to dT expected from theory.

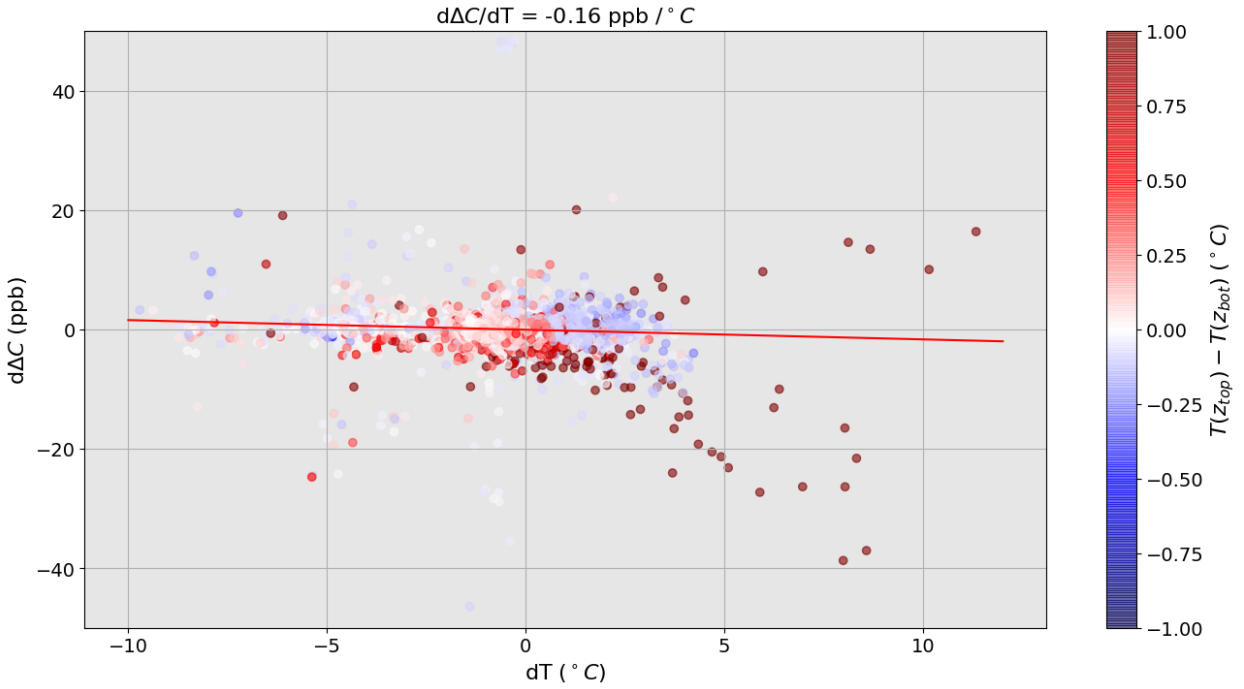

Figure 3-12: Same as Figure 44, with sonic-derived vertical temperature difference now plotted in color. Positive (red) values mean top path is predicted to be warmer than bottom path.

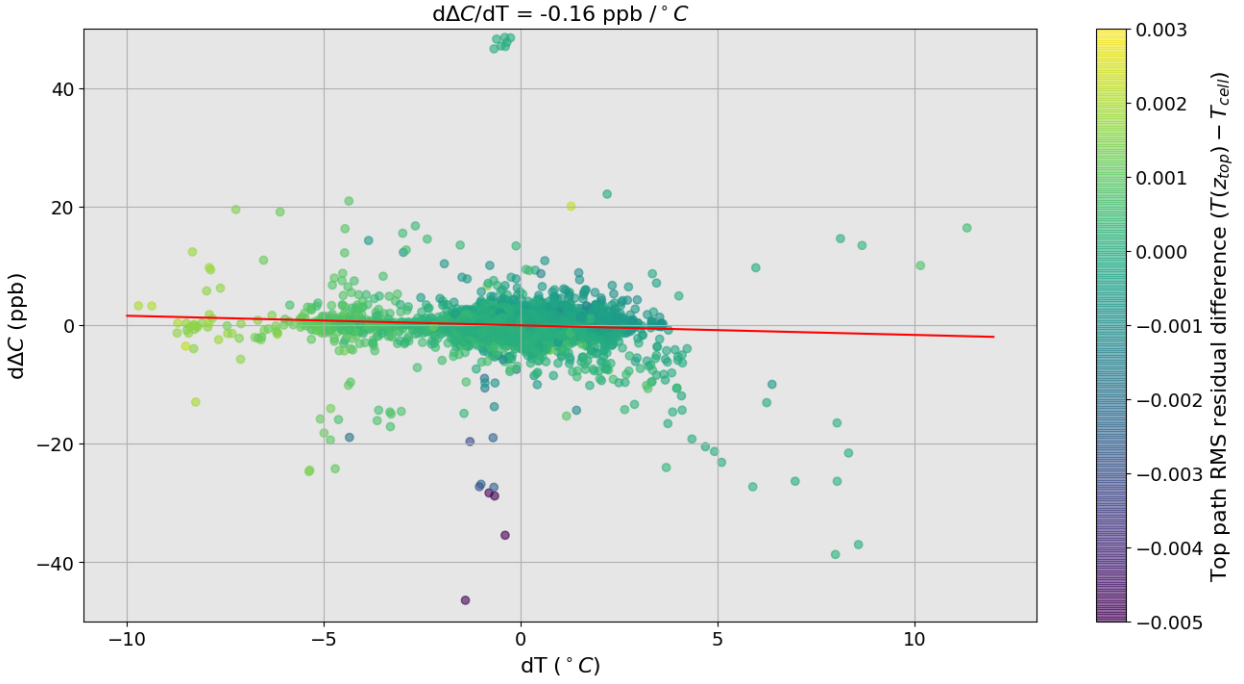

Figure 3-13: Same as Figure 44, with difference in the top path RMS residuals now plotted in colour. Negative residual difference values mean that retrievals using $T(z_{top})$ had a slightly better fit than retrievals using T_{cell}.

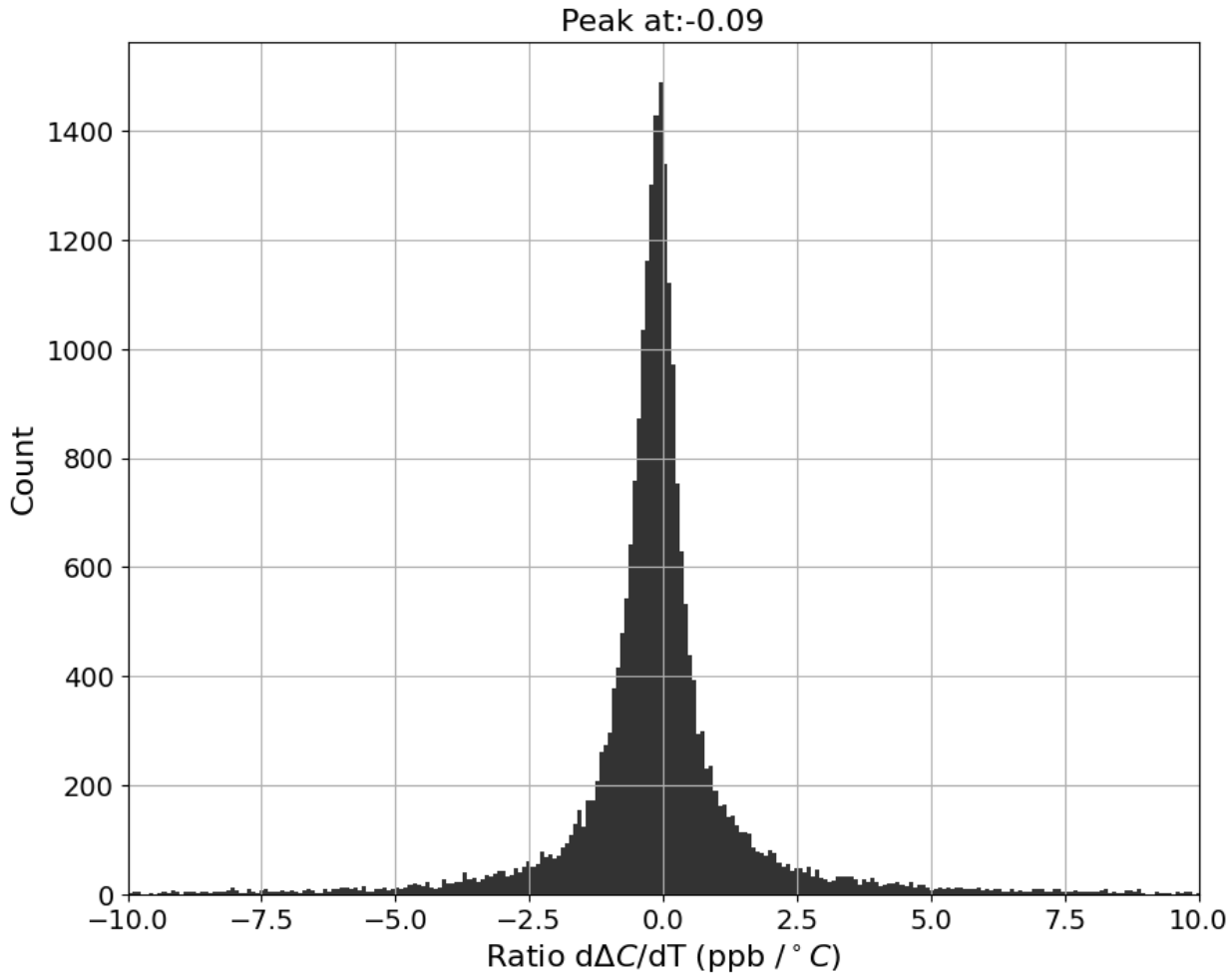

Figure 3-14: Histogram of the ratio $d\Delta C/dT$ with the peak value at 0.09 ppb/℃. The absolute value for 90% of the data is less than 3.5 ppb/℃.

3.3. Campaign N_2O Flux Results

3.3.1. Uncertainty calculation

To find the uncertainty for the calculated flux the formulation presented by Flesch et al. (2016) was used. The campaign concentration data ensemble was used to refine and customize the $d\Delta C/dT$ and σ_C variables and that analysis was shown above (previous Sections 3.2.2 and 3.2.3). Other variables that are more established, which this project could not quantify in any case, were taken from literature (described below). The equation for error propagation in the flux calculation is shown in Equation 11 (Flesch et al., 2016).

Equation 11

$$\frac{\delta F}{F} = \sqrt{\left(\frac{\delta S_c}{S_c}\right)^2 + \left(\frac{\delta \int K_m}{\int K_m}\right)^2 + \left(\frac{\delta \Delta C}{\Delta C}\right)^2}$$

The first term is the relative uncertainty in the Schmidt number and is assumed to be $\frac{\delta S_c}{S_c} = 0.2$ (Flesch et al., 2016). The second term is the relative uncertainty of the integral over the FTIR path of eddy diffusivity of momentum (Equation 5). The value of $\frac{\delta \int K_m}{\int K_m}$ was empirically approximated by sonic anemometers at three heights on a tower by Flesch et al. (2014), where it was shown to be strongly dependant on u* with the relationship,

Equation 12 $$\frac{\delta \int K_m}{\int K_m} \cong 0.009(u^*)^{-1.37} .$$

Lastly, the uncertainty in the concentration gradient, ΔC, is expected to have two components:

Equation 13 $$\frac{\delta \Delta C}{\Delta C} = \frac{\sqrt{2\sigma_C^2}}{\Delta C} + \frac{\frac{d\Delta C}{dT}\sigma_T}{\Delta C} .$$

The first component represents the quadrature sum of the variance of the top and bottom retrieved concentrations due to OP-FTIR instrumental precision. The value of $\sigma_C = 0.3$ was used from (Bai et al., 2011), which was confirmed to broadly agree with values from this experiment (Section 3.2.2). The second component accounts for uncertainty in the retrieved concentration difference due to uncertainty in the temperature input into the retrieval. Here a change was employed to the equation used in Flesch et al. (2016) where $\frac{d\Delta C}{dT}$ was used instead of $\frac{dC}{dT}$. An analysis of values of $\frac{d\Delta C}{dT}$ and $\frac{dC}{dT}$ from this project is discussed in Section 3.2.3. The resultant uncertainty values thus calculated are compared to those calculated using the $\frac{dC}{dT}$ value used in Flesch et al. (2016) in the following paragraph. Finally, the standard deviation of the temperature error, σT, was also found to be strongly dependant on u* during the tower experiment in Flesch et al. (2014) and was modeled as,

Equation 14 $$\sigma_T \cong 0.045(u^*)^{-1.07} .$$

In Flesch et al. (2016) a value of $\frac{dC}{dT} = 0.0038(C)$ was used in Equation 13, where 0.0038 is a ratio of the error in C to the measured C, or 0.38%. For the average measured concentration of 347 ppb this error amounts to 1.3 ppb, which is about half of our inferred value for a single path

concentration (2.2 ppb). In any case, the error propagation for a function $\Delta C(C_1, C_2, T) = C_1(T) - C_2(T)$ implies the error in ΔC to be,

$$\delta\Delta C = \sqrt{2\sigma_C^2} + \sigma_T \frac{d\Delta C}{dT},$$

which suggests that the value $\frac{d\Delta C}{dT}$ should indeed be used instead of $\frac{dC}{dT}$ (the former having a 10x smaller value of 0.16 $ppb/°C$ as inferred in Section 3.2.3). However, our error estimate is in fact larger than Flesch et al. (2016) since ΔC also has smaller values (then a single path concentration) in the observed data set (0.17 ppb, 0.13 ppb, 0.29 ppb, 0.56 ppb for mean, median, 25th and 75th percentiles, respectively, as shown in Table 6), then the relative ratio of $\frac{d\Delta C}{dT} = 0.16\ ppb/°C$ to ΔC is needed to give a sensitivity value in the same format as the 0.0038 value from Flesch et al. (2016). This ratio is 0.94, 1.23, 0.59 and 0.29 in the mean, median, 25th and 75th percentile sense. Therefore, $\frac{d\Delta C}{dT}$ used in this project is 247x (0.94/0.0038) more sensitive to temperature error than in Flesch et al. (2016) – for a mean ΔC of 0.17 ppb.

To summarize, the first term in Equation 11, representing the uncertainty in the Schmidt number is constant at $\frac{\delta S_c}{S_c} = 0.2$. The second term for the uncertainty of the diffusivity integral has a median value for the data set of $\frac{\delta \int K_m}{\int K_m} = 0.04$. The third term for the uncertainty of the concentration difference has a median value for the data set of $\frac{\delta\Delta C}{\Delta C} = 1.07$ (the median is used here because near zero ΔC values in the full data set skew the means of the ratios). The total uncertainty of the flux for the median value of the data set is $\frac{\delta F}{F} = 1.09$ or 109%. To compare these relative contributions for the range of values in the observed data set refer to Table 7.

Table 7: Contributions of uncertainty terms to final flux (relative) uncertainty. The uncertainty in the concentration difference, $\frac{\delta\Delta C}{\Delta C}$, is the dominant term for most of the data set. The extremely large maximum values in $\frac{\delta\Delta C}{\Delta C}$ are due to near zero ΔC values (minimum $\Delta C = 4x10^{-6}$ ppb).

	$\frac{\delta S_c}{S_c}$	$\frac{\delta \int K_m}{\int K_m}$	$\frac{\delta \Delta C}{\Delta C}$	$\frac{\delta F}{F}$
Mean	0.20	0.07	11.33	11.36
Median	0.20	0.04	1.07	1.09
Min	0.20	0.01	0.01	0.20
10%	0.20	0.02	0.37	0.44
25%	0.20	0.03	0.58	0.63
75%	0.20	0.08	2.29	2.30
90%	0.20	0.14	5.88	5.88
Max	0.20	12.80	134088.33	134088.33

The previous analysis is for the finest time resolution available in the merged data set of 4 m 19 s. It was assumed that the flux does not vary significantly for an interval up to 30 minutes. This allows for the resampling of the data for a mean flux in each 30-minute interval. To represent the standard error of the mean the average uncertainty during each 30-minute interval is reduced by a factor of $1/\sqrt{n}$, where n is the number of samples in the interval. The histogram in Figure 3-15 shows the completeness of these 30-minute intervals, with 7 samples per bin being the maximum and 0 samples per bin being a missed observation. Over the ensemble, 70% of 30-minute averaging bins that had recorded data were complete with the maximum of 7 samples per 30 minutes, 22% of intervals with observations in them had 6 samples, and 8% had less than 6 samples.

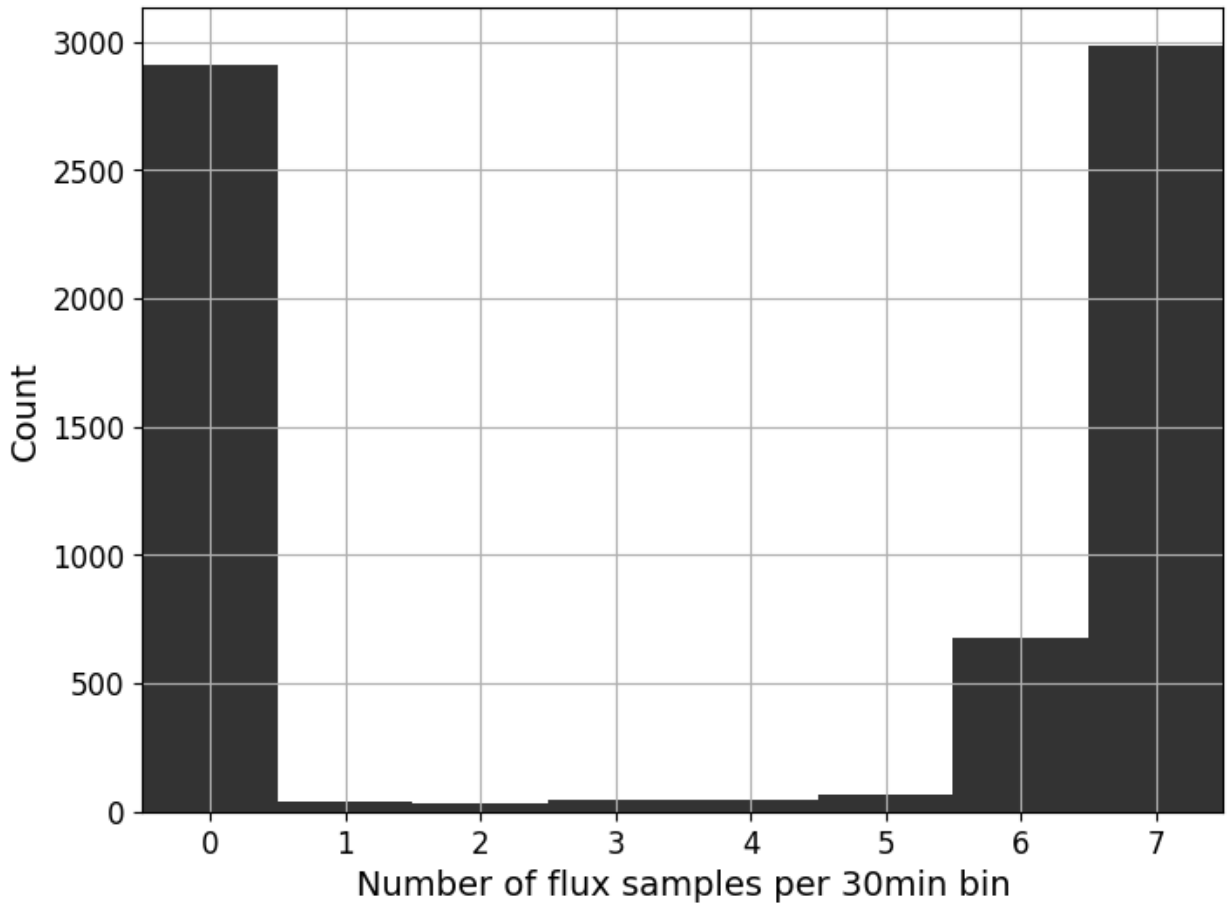

Figure 3-15: Histogram of the number of 4 m 19 s observations in each 30-minute interval. A complete sampling interval has a maximum of 7 observations.

Now that the flux data set is completed with uncertainty values, Figure 3-16 shows a histogram of the ratio of flux and to the error in flux (whereas Figure 3-4 used only the $\frac{\Delta C}{\delta \Delta C}$ portion of the uncertainty). This gives an approximation of the signal to noise ratio present in the calculated flux dataset. When this ratio is equal to one this represents a critical threshold where the flux is measured to be negative or positive but just at the noise level. For 4 m 19 s intervals $\frac{F}{\delta F} > 1$ for 46% of the data. Figure 3-17 shows the same ratio with the data set resampled to 30-minute intervals. Due to reduced uncertainty in the mean and smoothing of noisier measurement periods, $\frac{F}{\delta F} > 1$ for 69% of the data at 30-minute intervals. Note the change of x-axis limits and the higher values of $\frac{F}{\delta F}$ in Figure 3-17.

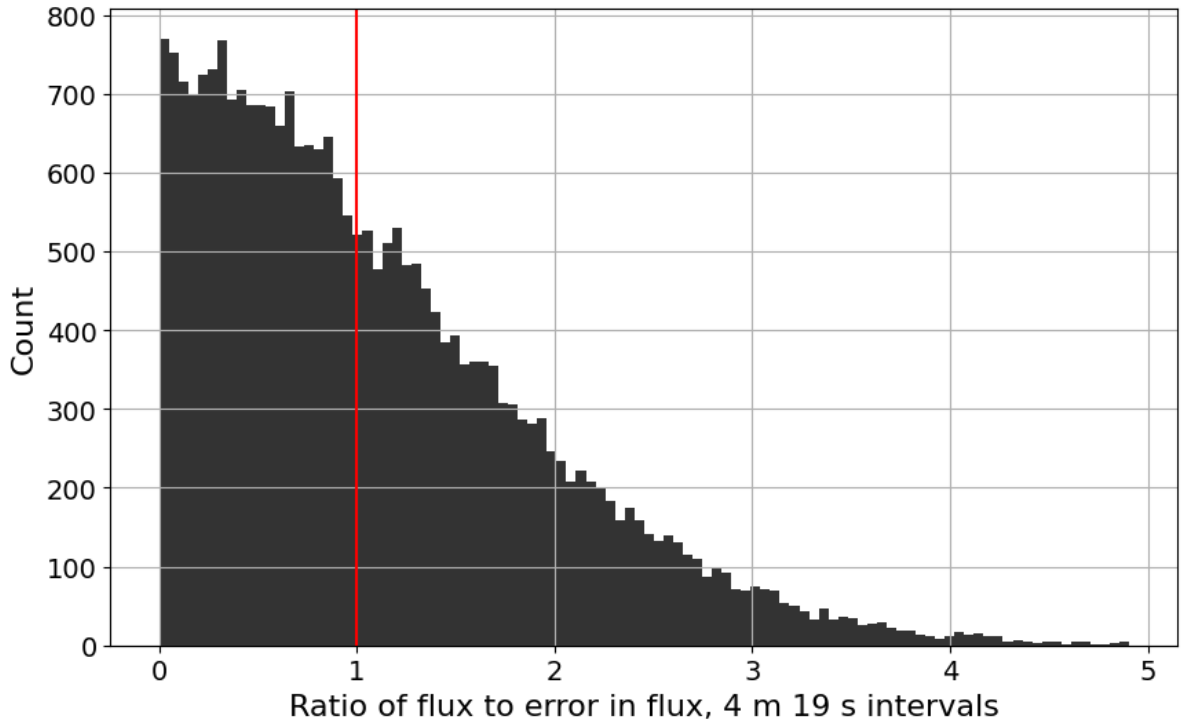

Figure 3-16: Histogram of the ratio of flux to error in flux (4 m 19 s intervals). Data to the right of x=1 (red line) represents 46% of data points and has smaller error than the observed magnitude of flux, so the direction of flux (source or sink) is predicted with more certainty.

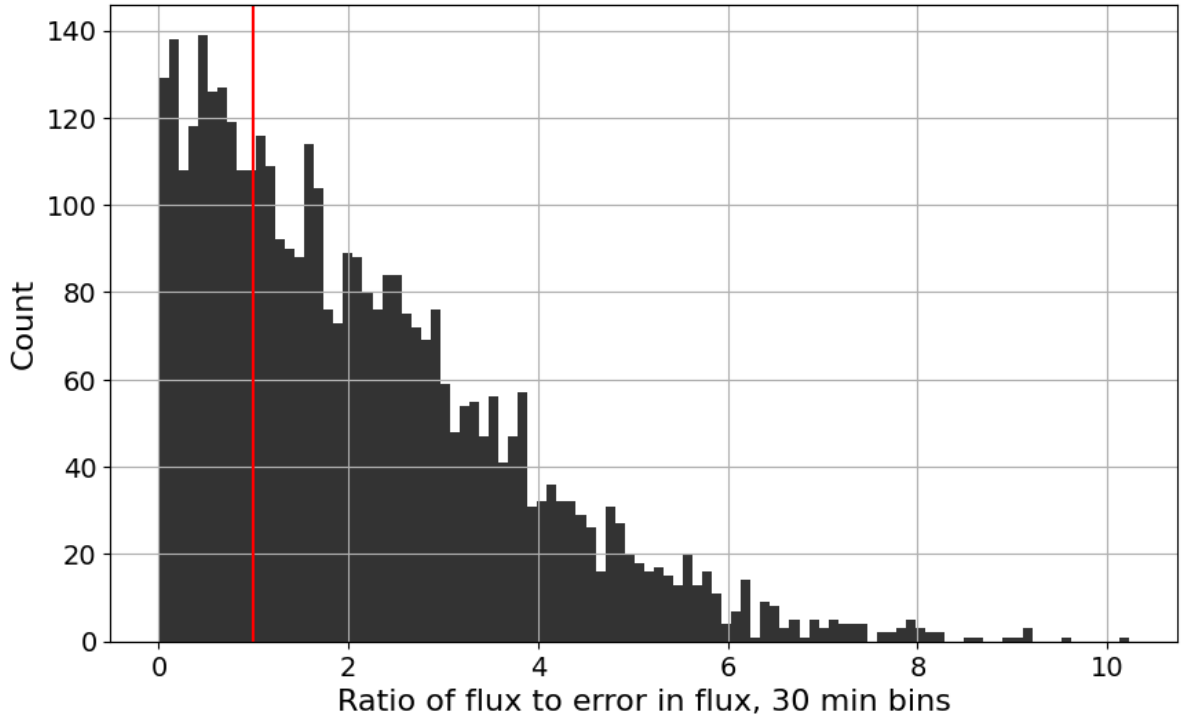

Figure 3-17: As in Figure 49, but in 30-minute intervals, with 69% of points above red line.

3.3.2. Flux result overview and seasonal values

As an overview of the N_2O ocean-air flux, data Table 8 shows the statistics for calculated fluxes in 30-minute intervals, as well as in daily means. The minimum daily flux was $-50.78 \pm 12.49\ g_{N_2O}\ ha^{-1}\ h^{-1}$, recorded on December 13, 2020. This negative flux means the ocean was a sink of atmospheric N_2O. The error in daily means is calculated as the average of the error in the 30-minute observations on that day. The daily error is not reduced by the square root of n, as would be the case with standard error in the mean, because the flux cannot be assumed to remain constant all day. The maximum daily flux was observed just 3 days after the minimum on December 16th, 2020, with a value of $+51.90 \pm 15.79\ g_{N_2O}\ ha^{-1}\ h^{-1}$. Over the observation period, flux was negative for 61% of the time; using the mean flux and the total hours observed, the total measured N_2O absorbed from the atmosphere by the ocean was $-10.81\ x\ 10^3\ g_{N_2O} ha^{-1}$. Prior knowledge suggested the expectation of the ocean being a net source, as discussed in Chapter 1 (Thomson et al., 2012), however, that is not what was observed in Halifax harbour from December to April. There is certainly the possibility that if we had observed 100% of the time during the campaign, the mean flux could end up being very different, especially given the strong episodic events discussed in Section 3.3.4.

Table 8: Statistics for calculated fluxes in 30-minute intervals and in daily means.

	30-minute means ($g_{N_2O}\ ha^{-1}\ h^{-1}$)	Daily means ($g_{N_2O}\ ha^{-1}\ h^{-1}$)
Count	3895	100
Mean	-5.55	-5.17
Standard deviation	28.23	16.81
Standard error (SE)	0.45	1.68
Minimum	-253.2	-50.78
25%	-18.66	-16.98
50% (Median)	-4.44	-5.74
75%	6.56	5.42
Maximum	244.5	51.91

Figure 3-18 shows the 30-minute N_2O ocean-air flux for an example four-day period from January 18th to 22nd plotted along with a 3-hour moving average, the tidal water level as well as the diurnal cycle. There is no significant correlation of flux to tidal or diurnal cycles. Figure 3-19 shows the daily mean N_2O fluxes for the full 5-month observation period together with the daily mean retrieved concentration differences, ΔC. Daily mean ΔC correlates very well to the flux (note the inverted y-axis to make it easier to compare), which is promising for additional usability of data collected when the 3-D sonic anemometer was not available, which includes September – October of 2018 and May – December of 2021. Daily mean ΔC can be used to qualitatively identify significant flux events because the sign of flux (capturing whether the ocean is a source or sink of N_2O at a given time) is entirely due to (opposite of) the sign of ΔC. Much of the time even the relative scale of peaks in daily mean ΔC lines up with peaks in flux, so to quantify flux only a constant multiplier may suffice for certain scenarios.

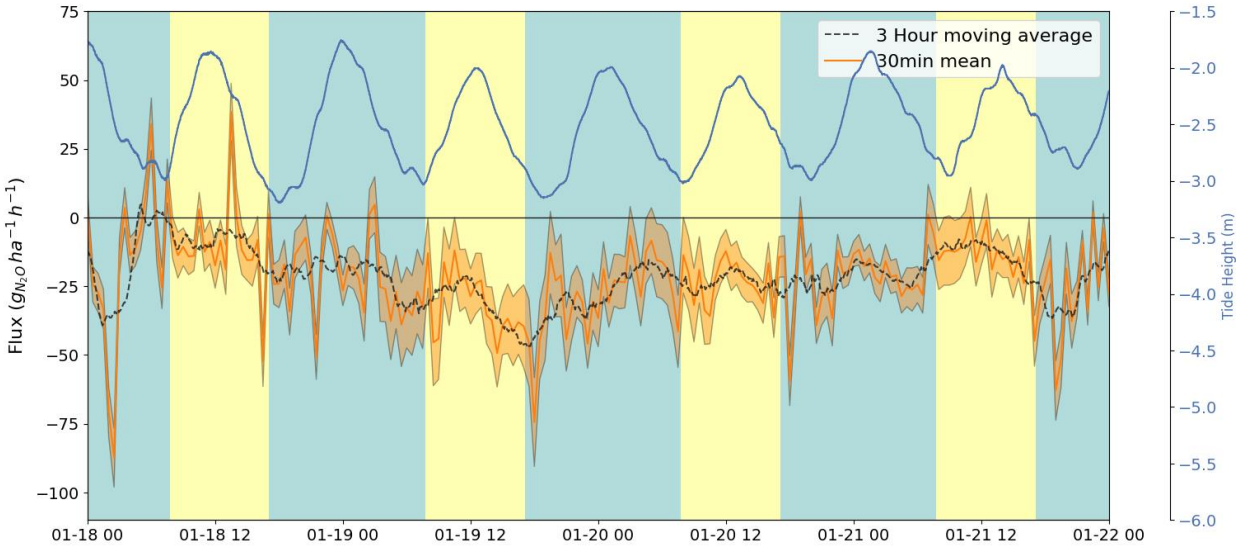

Figure 3-18: 30-minute N_2O flux (orange, with uncertainty shading) during a four-day period from January 18th to 22nd, 2021. Black dashed line: 3-hour moving average. Blue line: Tidal height. Background blue and yellow bands: Diurnal cycle. Positive flux is out of the ocean.

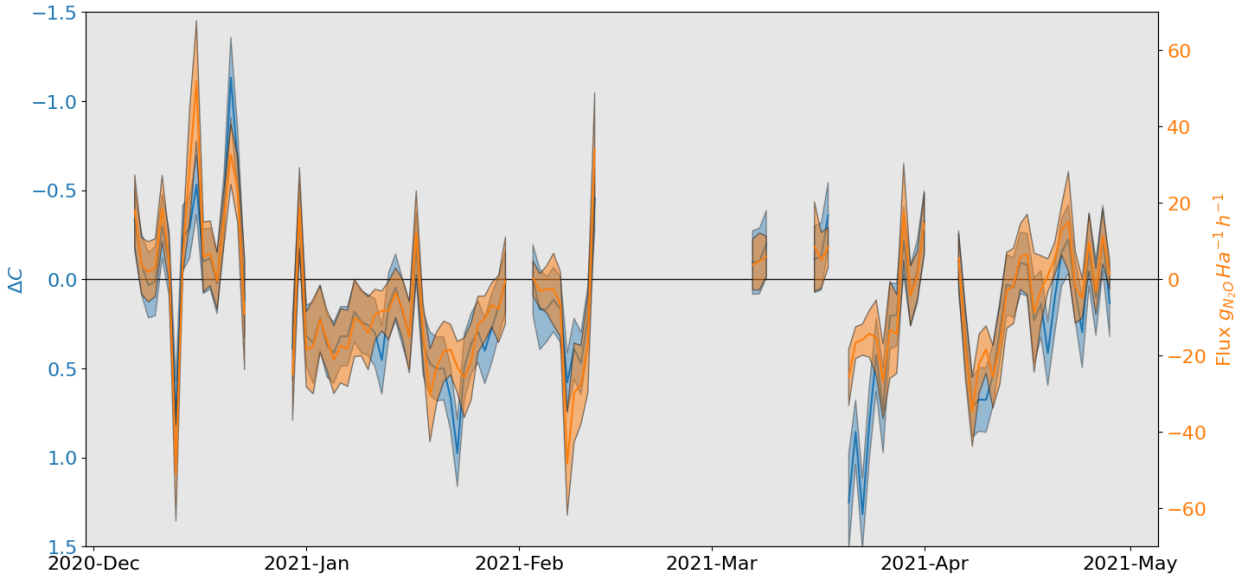

Figure 3-19: Daily N_2O fluxes (orange) and retrieved concentration differences (blue) for the full campaign period. Positive flux is out of the ocean. Concentration differences shown reflected about x-axis to highlight correlation to flux.

Returning to the work of Manizza et al. (2012), who modelled seasonal variation of ocean to atmosphere N_2O flux, Figure 3-20 shows the model predictions, which are now divided into latitude bands as opposed to a global map (Section 1.1.3). The model has a simplified approach to N_2O biological production controls and does not account for the variation in coastal ecosystems, in part due to the coarse resolution of 320 km by 320 km. However, it can serve as an order-of-magnitude comparison between observations at Halifax Harbour and predicted global ocean-atmosphere fluxes. In the geographic region north of 30°N the model predicts N_2O fluxes of –0.2 to 1.0 $\mathrm{mol_{N_2O} m^{-2} yr^{-1}}$ during the time of year that the Halifax observations were made. In the 10-30°N region the model predicts smaller N_2O fluxes of –0.1 to 0.2 $\mathrm{mol_{N_2O} m^{-2} yr^{-1}}$. Shown in Figure 3-21, the N_2O flux measurements from Halifax harbour were converted to the same units of $\mathrm{mol_{N_2O} m^{-2} yr^{-1}}$ and resampled to 15-day intervals (approximately bi-monthly) for an easier comparison to the model prediction. The magnitude of our total N_2O flux observations is more similar in scale to the model prediction at 10-30°N, even though Halifax is at 45°N. Also, similarities are not found between our observation and the model in the seasonal variation of total N_2O flux at latitudes > 30°N, with the model predicting a transition from small negative to small positive total flux (blue line in Figure 3-20) in late fall to early winter, a peak positive flux in mid-

winter and a diminishing flux into spring. Interestingly, the overall negative (in fall and winter) thermal N_2O flux component (red line in Figure 3-20, panel b) does agree well with our observations in both scale and seasonal variation. Also interesting is the fact that the N_2O flux due to ventilation (convective transport from deeper water) is positive, and we observed a strong albeit transient ocean-source event in December (Section 3.3.4). It is conceivable that more of such events could have occurred during some of our missed observations in winter. Again, the comparison to the global model (320 km by 320 km resolution) zonal average for latitudes > 30°N can only serve as an order-of-magnitude verification of the validity of our measurement-derived flux in a coastal setting.

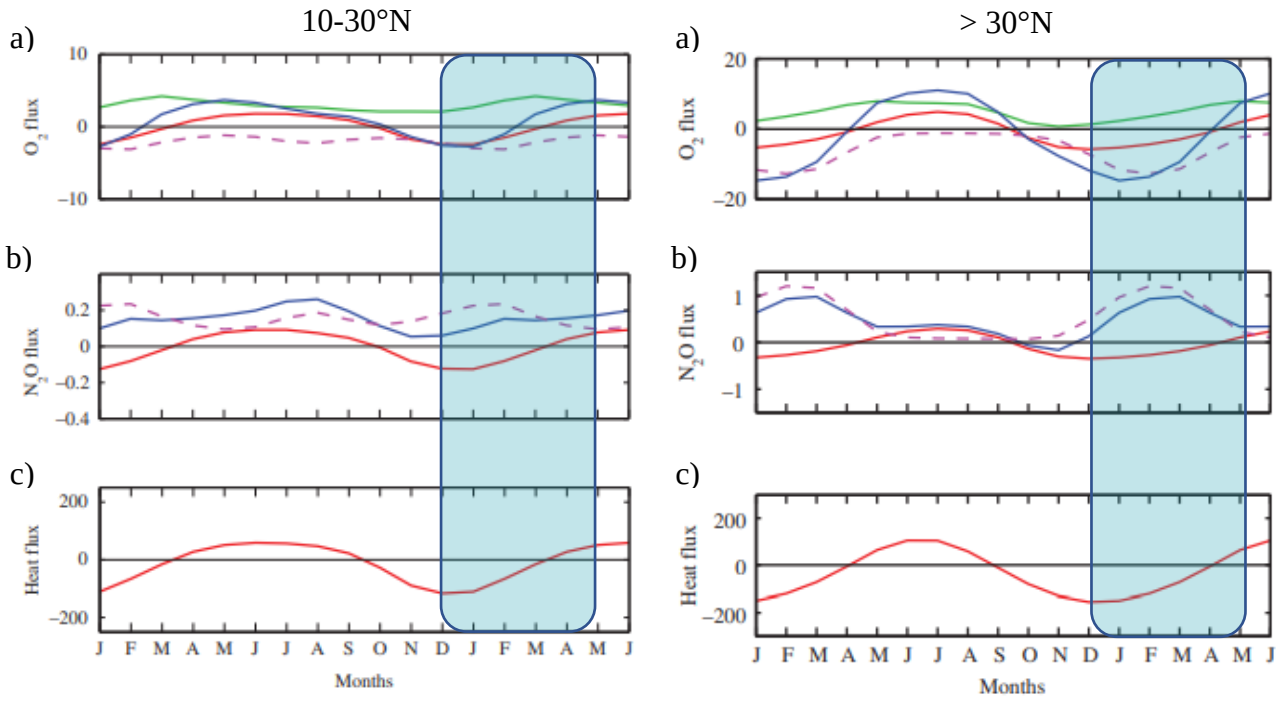

Figure 3-20: Seasonal ocean-air flux model predictions modified from Manizza et al. (2012). Left panels: zonal flux averages for 10-30°N. Right panels: zonal flux averages for >30°N. Note the change in y-axis scale for left vs. right panels. Panels (a): O_2 flux with (blue) total flux, (red) thermal flux component, (dashed magenta) ventilation flux component and (green) production flux component. Panels (b): N_2O flux in $mol_{N_2O} m^{-2} yr^{-1}$ with (blue) total flux, (red) thermal flux component, and (dashed magenta) ventilation flux component. Panels (c): Heat flux. Blue highlighted area represents the Halifax Harbour measurement period from December 2020 to April 2021. Positive flux is out of the ocean.

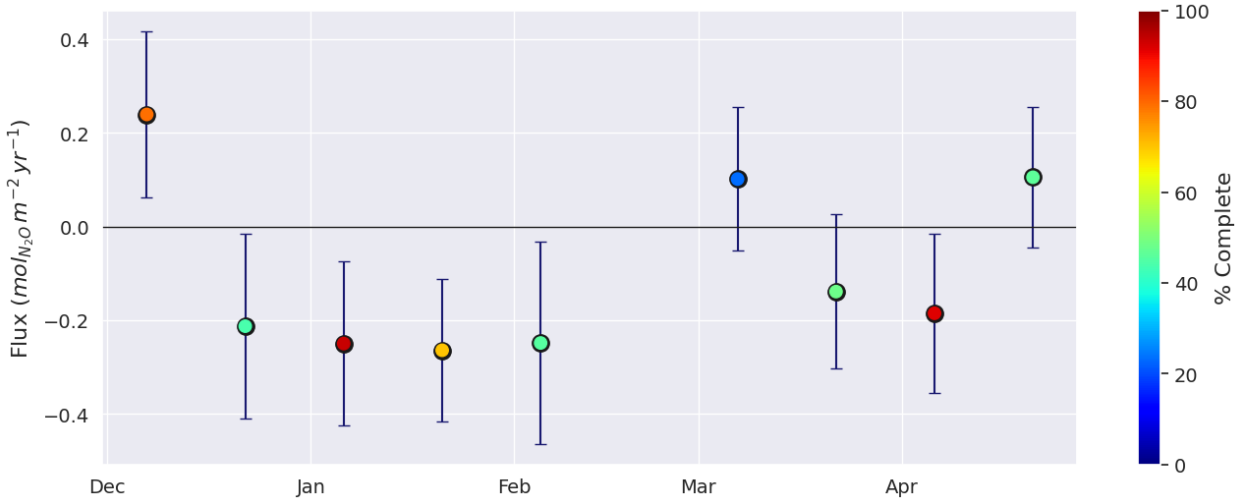

Figure 3-21: Halifax Harbour ocean-air N_2O flux in 15-day means and same units as the seasonal model prediction of Manizza et al. (2012). The error bars are the mean of the 30-minute errors in each 15-day interval. The colour of each point is a measure of how completely each 15-day period was observed (fraction of time observed out of total possible measurement time) given various interruptions in data collection.

3.3.3. Relationships between N_2O flux and wind, tides and heat flux

The placement of the 3-D sonic anemometer was a matter of some debate prior to instrument deployment in December 2020. The OP-FTIR measures average concentrations within a path across the water, with the shore assumed to have no significant impact on the measurements. The 3-D sonic anemometer, however, is a measurement at a point, and the properties measured by the sonic (turbulence, heat flux) will correspond to the surface conditions within an upwind footprint. An optimal placement for the sonic was chosen as described in Section 2.1.2. Now, post experiment, a review of the data ensemble is possible to potentially expose any bias (e.g., flow being unrepresentative of the ocean area) caused by the influence of local physical structures near the 3-D sonic anemometer tower. If there is a bias it should primarily be related to wind direction, where if the wind encounters the length of the jetty structure at the water's edge head-on it is expected to influence the wind properties more than if the wind is traveling parallel to the jetty. Figure 3-22 shows the friction velocity and the flux vs. wind direction with wind speed plotted in color. Wind directions of 0, 90, 180, 270 degrees are N, E, S, W respectively. As seen in the wind rose in Figure 3-1 (Section 3.1) the most frequent wind direction is from the N (0 deg) to NW (315 deg), and these directions correspond to the highest wind speeds. More frequent wind directions

end up having more data points so a larger range of fluxes can be seen in these sectors. Additionally, it is true that higher wind speeds result in larger u*, which also results in a larger flux. The distribution of wind directions and speeds fits with the expected wind flow in a harbour channel for which the most unobstructed path is oriented from the NW to the SE, with prevailing winds coming from the NW during the time of year observed. There is no obvious bias with wind direction, but we now explore further.

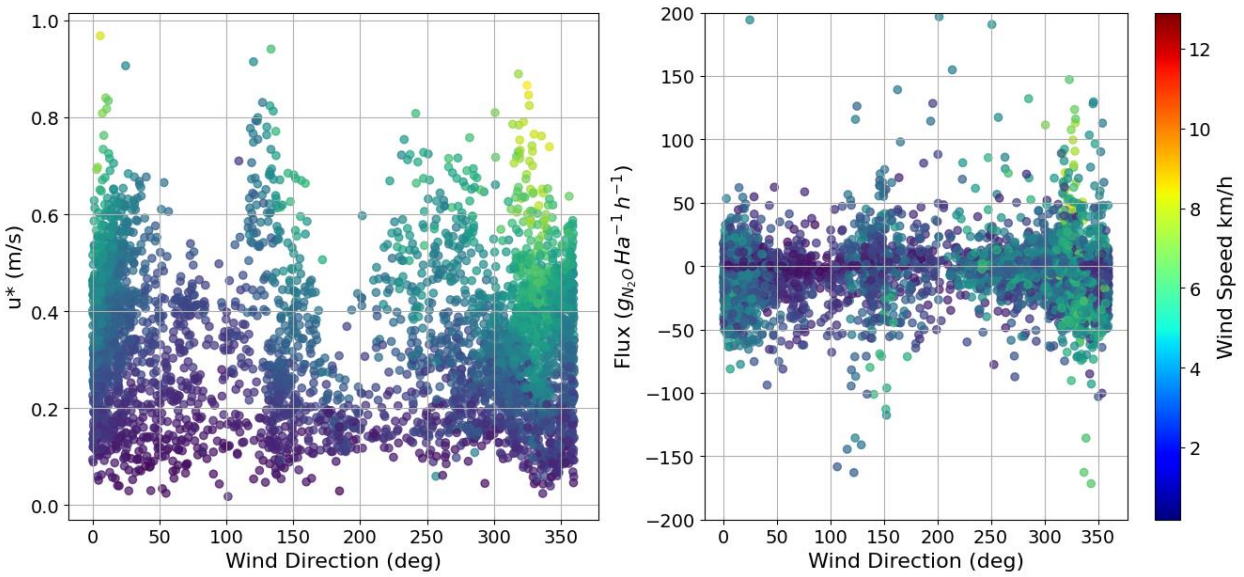

Figure 3-22: The friction velocity, u*, and the N_2O flux vs wind direction, with wind speed plotted in color. For wind direction 0, 90, 180, 270 degrees are N, E, S, W respectively.

To better inspect the distribution of the data for different wind directions Figure 3-23 and Figure 3-24 show "violin" plots with the data separated into wind direction bins each spanning 45 degrees and centered on the cardinal direction labelled. If there is a bias in flux induced by the jetty structure affecting the sonic anemometer measurements, then a noticeable difference should be seen between less obstructed wind directions parallel to the jetty (NW to SE) and more obstructed wind directions perpendicular to the jetty (SW to NE). The data is further split into two tidal ranges with data above the mean water level labelled as "High" and data below the mean water level labelled as "Low". Figure 3-24 uses only data above the 75th percentile for high tide and only below the 25th percentile for low tide, thus filtering out conditions at mid-tide. It is conceivable that a bias due to the jetty obstruction would affect the results differently depending on the tide. Perhaps for observation in the low tide bin, when the jetty is an average of 0.87 meters

higher above the water surface than in the high tide bin (1.3 meters when the mid tide is filtered out), the larger obstruction could introduce a more prominent step change in surface roughness leading to larger eddies and more vertical wind velocities and therefore increasing the range of calculated N_2O fluxes. However, it is in fact the high tide bin that tends to have a larger range of fluxes (wider vertical distributions in Figure 3-23 and Figure 3-24), when the obstruction from the jetty is the smallest. This effect could potentially have a physical explanation related to either weather patterns or ΔC being affected by the mixing of deep and shallow ocean water as it flows into the harbour.

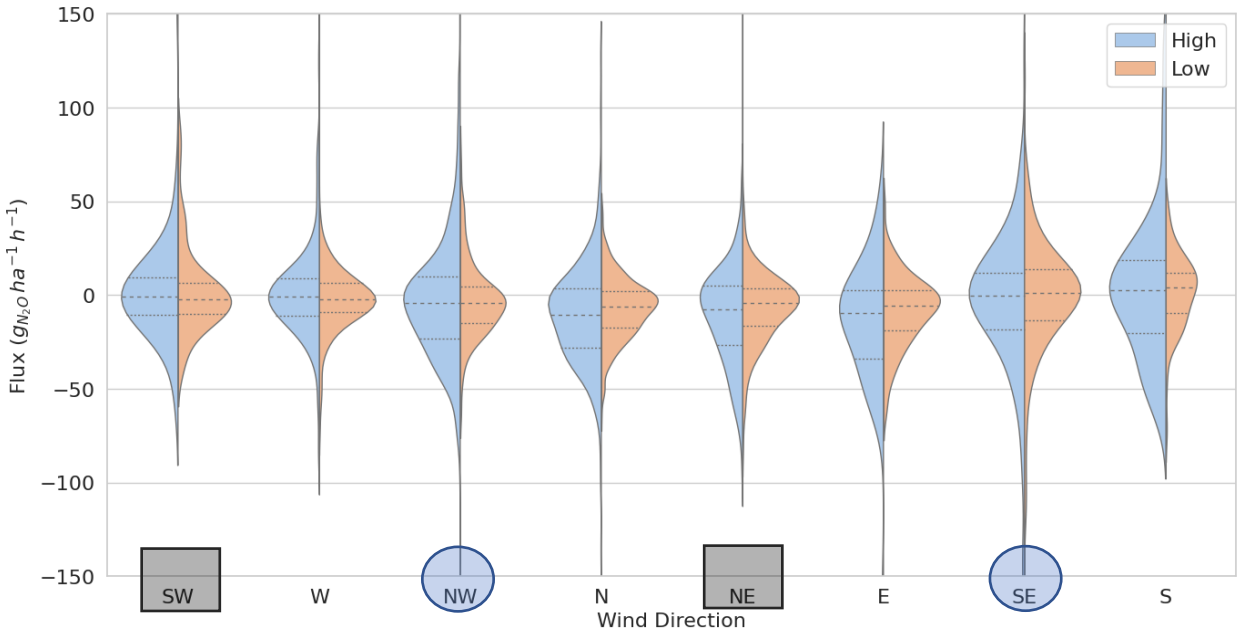

Figure 3-23: Violin plot with N_2O flux data separated into wind direction bins, each spanning 45 degrees and centered on the cardinal direction labelled. The data is further split into two tidal ranges with data above the mean water level labelled as “High” and data below the mean water level labelled as “Low”. Directions highlighted by a blue circle are over open water and directions highlight by a grey square are over land and buildings. Dotted lines on the distributions represent the 25th, 50th and 75th percentiles.

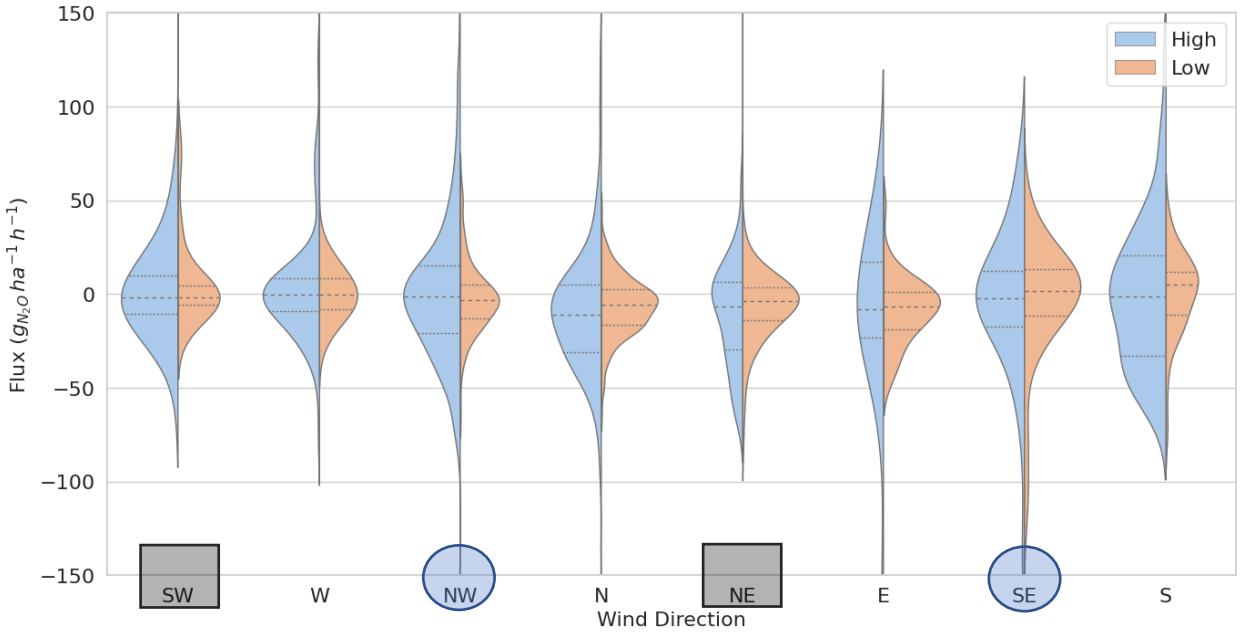

Figure 3-24: Same as Figure 3-23 except only tide levels from the 25th percentile and below are used for the "Low" bin and only tide levels from the 75th percentile and above are used for the "High" bin. Effectively, Mid-tide" data is hidden in this plot.

Figure 3-25 and Figure 3-26 show violin plots for the u* measurement. There are some differences between high and low tides, however, there are no stand-out features that are present depending on wind direction being perpendicular (SW-NE) or parallel (NW-SE) to the jetty. It is difficult to determine from this data what is physical to the harbour environment and what may be due to the placement of the sonic anemometer. Its is encouraging for the project that there is nothing obviously concerning showing up in these plots. In the end the sonic was placed in the best location that could be reasonably accessed in a working harbour and we do not discern noticeable issues with that placement. Consequently, the flux results were not filtered by wind direction and instead we opted to examine wind direction effects on a case-by-case basis.

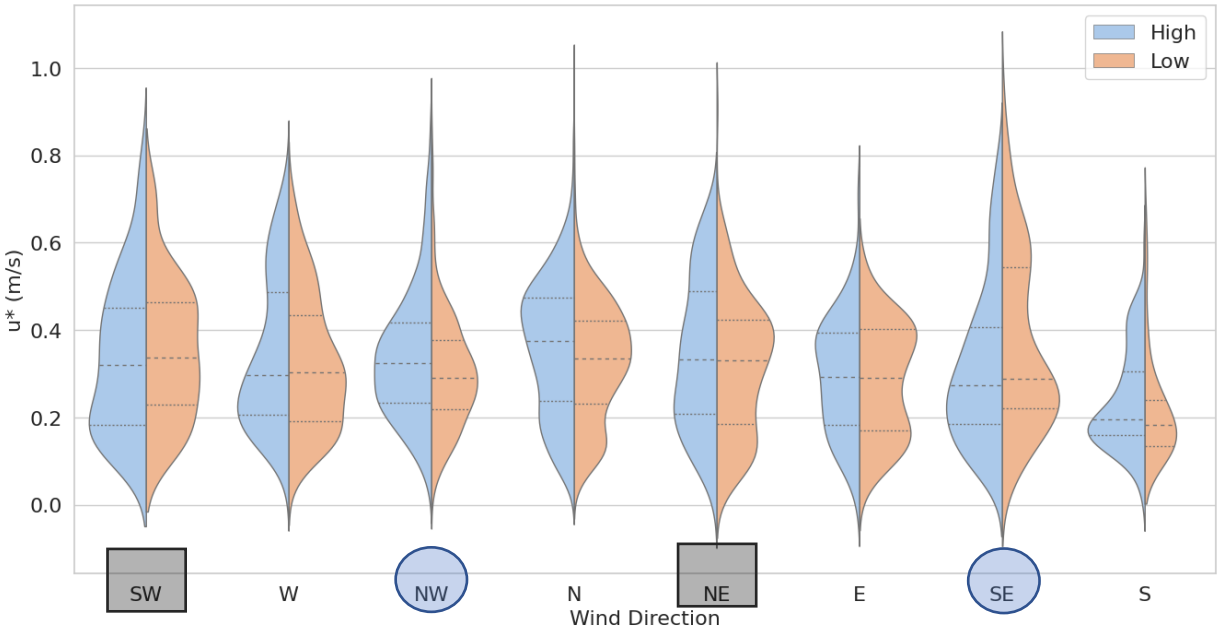

Figure 3-25: Violin plot with u* data separated into wind direction bins, each spanning 45 degrees and centered on the cardinal direction labelled. The data is further split into two tidal ranges, with data above the mean water level labelled as “High” and data below the mean water level labelled as “Low”. Directions highlighted by a blue circle are over open water and directions highlight by a grey square are over land and buildings. Dotted lines on the distributions represent the 25th, 50th and 75th percentiles.

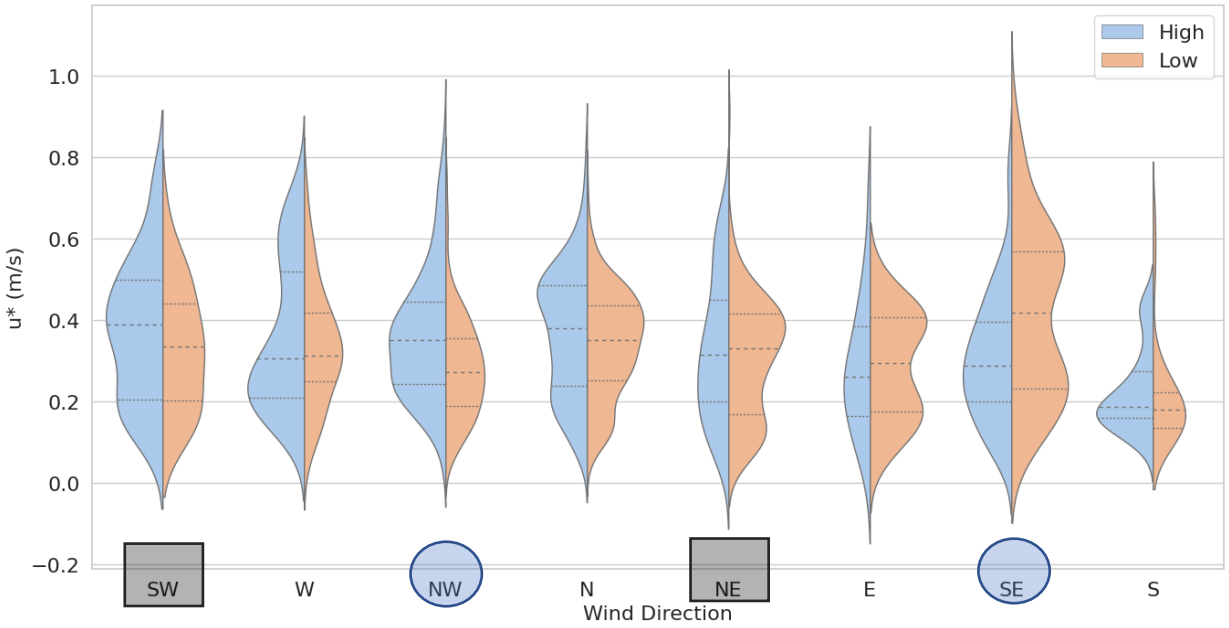

Figure 3-26: Same as Figure 3-25 except only tide levels from the 25th percentile and below are used for the "Low" bin and only tide levels from the 75th percentile and above are used for the "High" bin. Effectively, "Mid-tide" data is hidden in this plot.

Another relationship that is interesting is between u* and the flux of N_2O. Higher u* values are seen to correlate with a larger range of values in N_2O flux for a given set of ΔC values, which is shown in Figure 3-27. The limiting factor for N_2O flux during the observations in Halifax Harbour may be aerodynamic resistance of the boundary layer (rather than the internal rate of N_2O production/consumption or storage rate). Heat flux also has a similar relationship with N_2O flux and ΔC, with the sensible heat flux component, H_s, shown in Figure 3-28 calculated from the air density, ρ_a, heat capacity, c_p, and covariance of sonic temperature and the vertical wind component, $(Ts, Uz)_{cov}$, as:

$$H_s = \rho_a c_p \langle Ts, Uz \rangle \text{ (Rebmann et al., 2012).}$$

The latent heat flux component, L_e, shown in Figure 3-29 was calculated from the latent heat of vaporization, L_v, and covariance of the mass density of H_2O and the vertical wind component Uz as:

$L_e = L_v\langle[H_2O], Uz\rangle$ (Rebmann et al., 2012).

Positive heat fluxes correspond to heat transport from the ocean surface to the atmosphere and large out of ocean (positive) heat fluxes are seen to correspond to *both* large into ocean N_2O fluxes (negative) and large out of ocean N_2O fluxes (positive). These possibly point to the wind (and heat flux) conditions driving a convective overturning of water in the Bedford Basin. Wind (through the mechanism of driving ocean currents) and/or heat flux (through the mechanism of ocean surface cooling affecting water density) could increase convective overturning, bringing deeper anoxic and N_2O-rich (N_2O supersaturated) waters to the surface. Another process operating in parallel is that ocean cooling affects not only water density but also gas solubility, so strong ocean surface cooling could also lead to N_2O fluxes into the ocean, discussed further in Section 3.3.4.

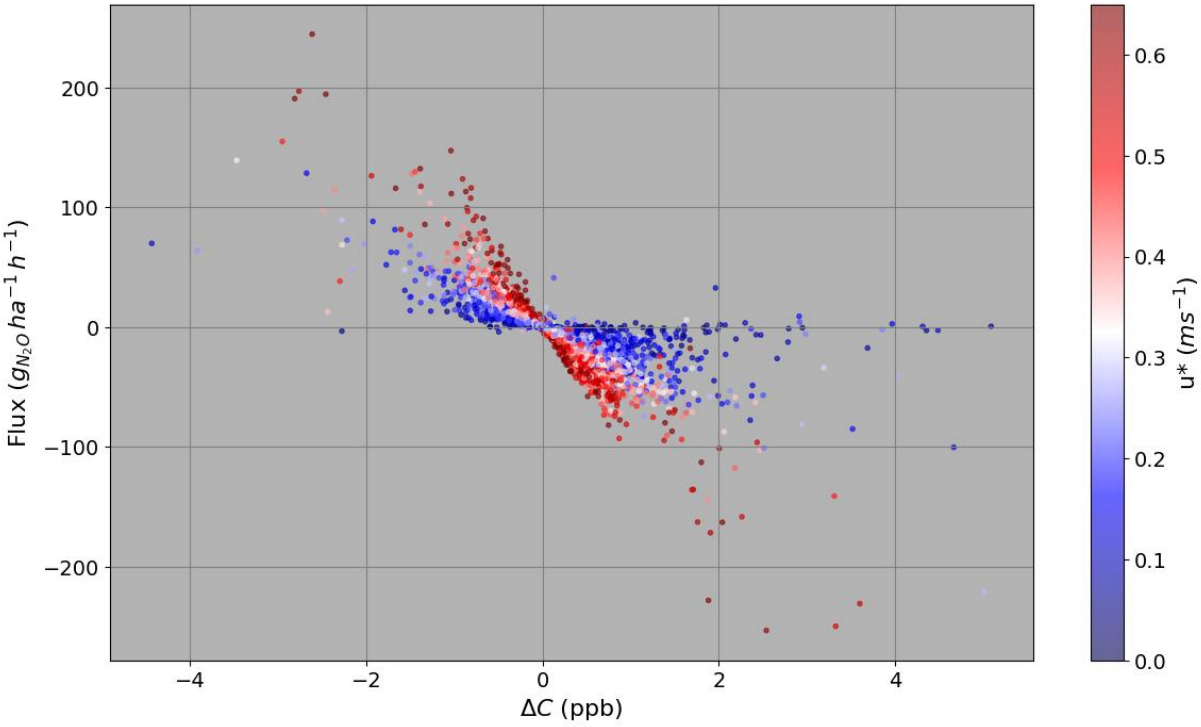

Figure 3-27: N_2O ocean-air flux plotted against the concentration difference, ΔC, with friction velocity, u* overlaid in color.

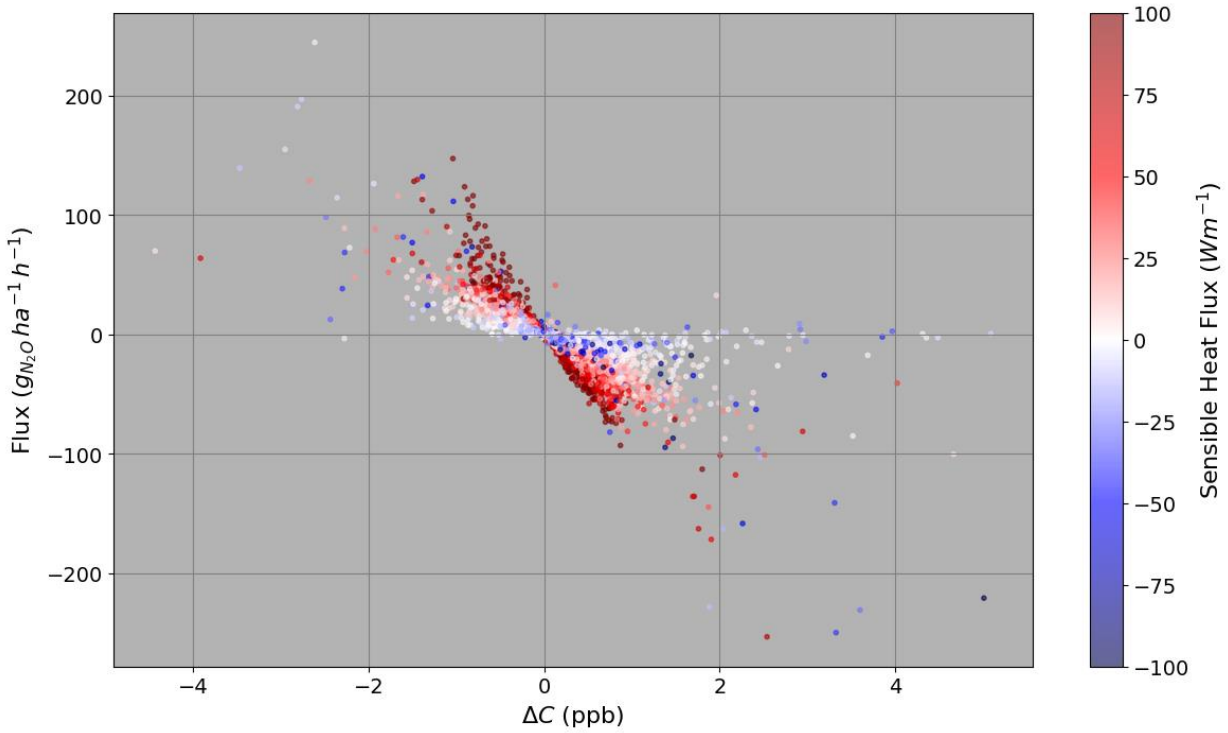

Figure 3-28: N_2O ocean-air flux plotted against the concentration difference, ΔC, with sensible heat flux, H_s, overlaid in colour. Postive H_s is out of ocean.

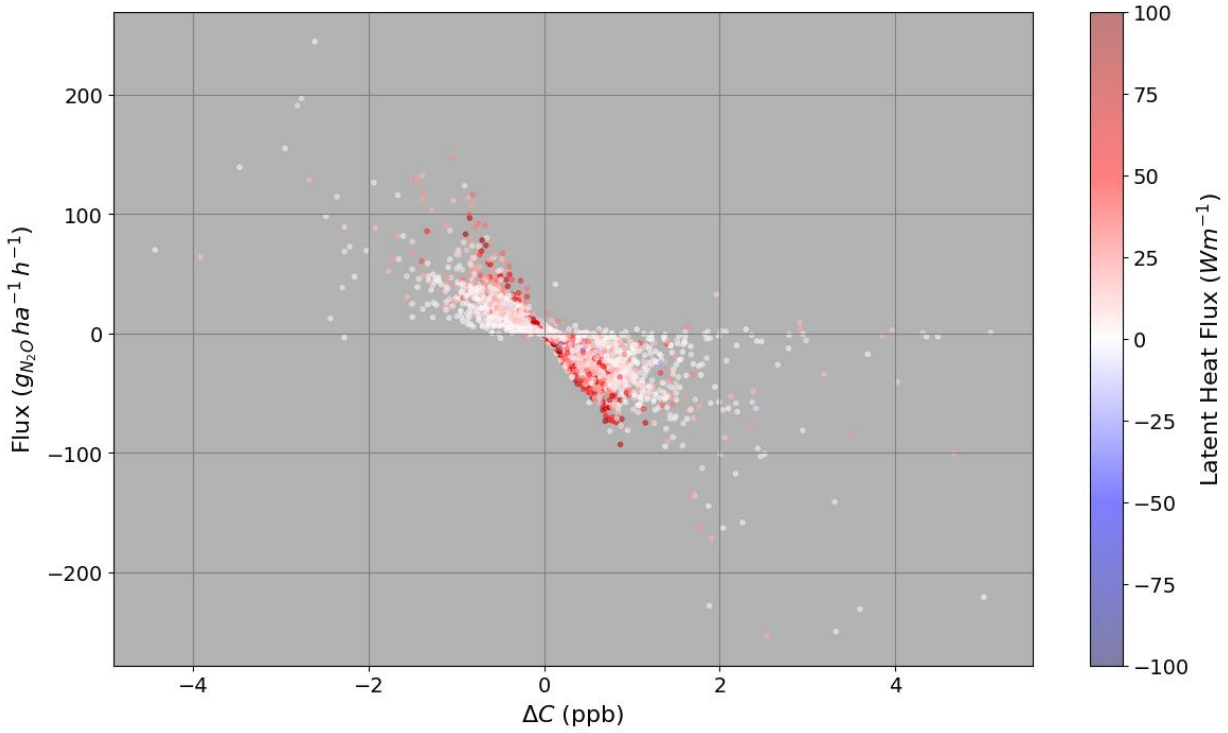

Figure 3-29: Figure 3-30: N_2O ocean-air flux plotted against the concentration difference, ΔC, with latent heat flux, L_e overlaid in colour. Postive L_e is out of ocean.

3.3.4. N_2O ocean source event case study

This section focuses on an event that was observed between December 15th and 17th 2020. Figure 3-31 and Figure 3-32 are an overview of several variables during the time of the event. In panel A, individual top and bottom path concentrations, IR signal levels, spectral fit RMS residuals from retrievals and ΔC are plotted as a function of time. These help identify any false signals that may have been missed by the filtering process. For example, if the signal levels are severely mis-matched, where one path dips below 0.1 while the other stays high, this will result in a false signal for ΔC. For this time range the signal of both paths tracks together very well and the December 19th to 21st period with signals differing by a maximum of ~0.25 does not show any sign of a false ΔC signal forming. The retrieval fit RMS residuals also track and are stable for both paths, confirming the retrieval process is not in a period of mis-fitting due to, e.g., too much beam extinction due to excessive atmospheric water vapour. N_2O concentrations for both paths are also reasonable and track together closely. All this to say that the December 16th event is a real environmental event and not an artifact of the OP-FTIR system.

Panel B shows the N_2O flux and further parameters to aid in the analysis of this event. The flux spike starting on December 15th and lasting until 12:00 noon on December 17th represents a total source of 2.00 $Kg_{N_2O}ha^{-1}$ released by the ocean surface. Precipitation data from two nearby weather stations is included (Windsor Park and Shearwater Jetty), as well as the sonic anemometers diagnostic flag, which corresponds to heavier rain events where droplets obstruct the transducers. Freshwater flux is of interest as a driver of flux outside of biological production/consumption of N_2O. Freshwater flux onto the ocean surface could affect gas solubility via reduced surface N_2O concentration to sub-saturated levels, effectively lowering the N_2O fluxes observed given a set amount of internal production. Alternatively, a lack of freshwater flux rules out this mechanism as a contributor to the observed fluxes. Unfortunately, we have not been able to witness such an effect as our instruments only function intermittently during heavy continuous rainfall. Two options were to look before and after rain events, or more interestingly, during heavy snow fall, which does not necessarily stop our instruments from recording useful data. Regardless, this N_2O ocean source event is not during heavy continuous rain, which is known even though the weather station data is intermittent because the sonic diagnostic flag is “on” only intermittently

meaning there was some intermittent rain but not heavy or long enough to affect the transducers continuously. There was no new snow reported during the event, however there may have been some snow melt of the previous snow fall.

A second mechanism that affects flux in addition to internal production/consumption is thermal changes of the ocean surface that could affect the storage capacity of N_2O. Thermal changes might influence flux via changes to the solubility of N_2O in seawater. Panel C shows some relevant weather measurements and tide levels. Of note is the drop in temperature and elevated u* during the N_2O source event. Panel D shows the wind direction and speed. The source event coincides with high wind speeds from the northwest. Winds from that direction during winter, over land and from the north, are usually cold compared to temperatures on the eastern coast of Nova Scotia.

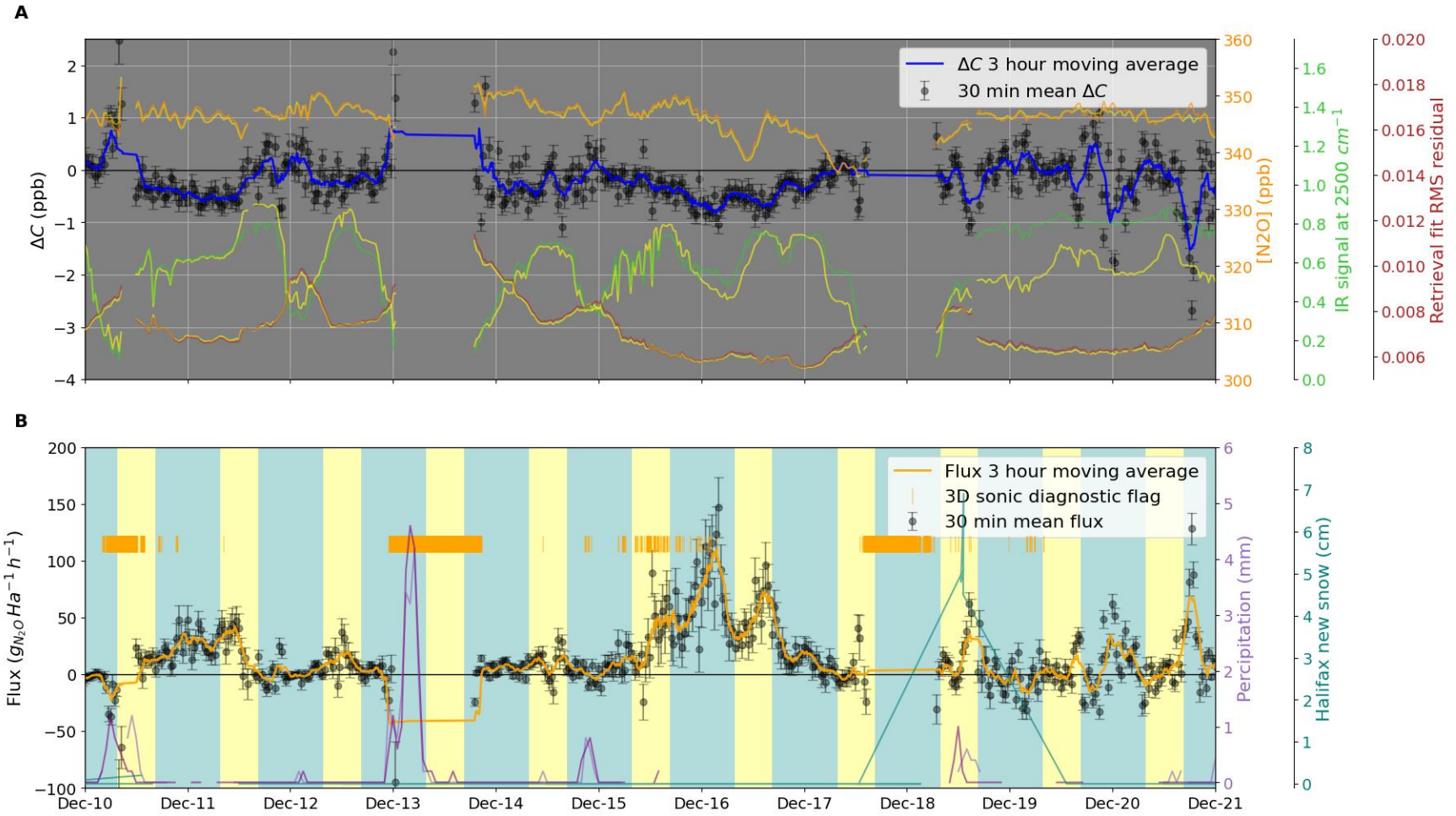

Figure 3-31: Ocean source event overview part 1. Panel A: 30-minute mean ΔC values in black, 3-hour moving average in blue. Individual path N_2O concentrations in orange and yellow (yellow is the top path in each color pair); IR signal level at 2500 cm-1 in green and yellow, and fit RMS residual from MALT in red and yellow. Panel B: Flux (black with orange moving average); precipitation data from two nearby weather stations (dark and light purple); new reported snow (teal); sonic diagnostic flag (orange).

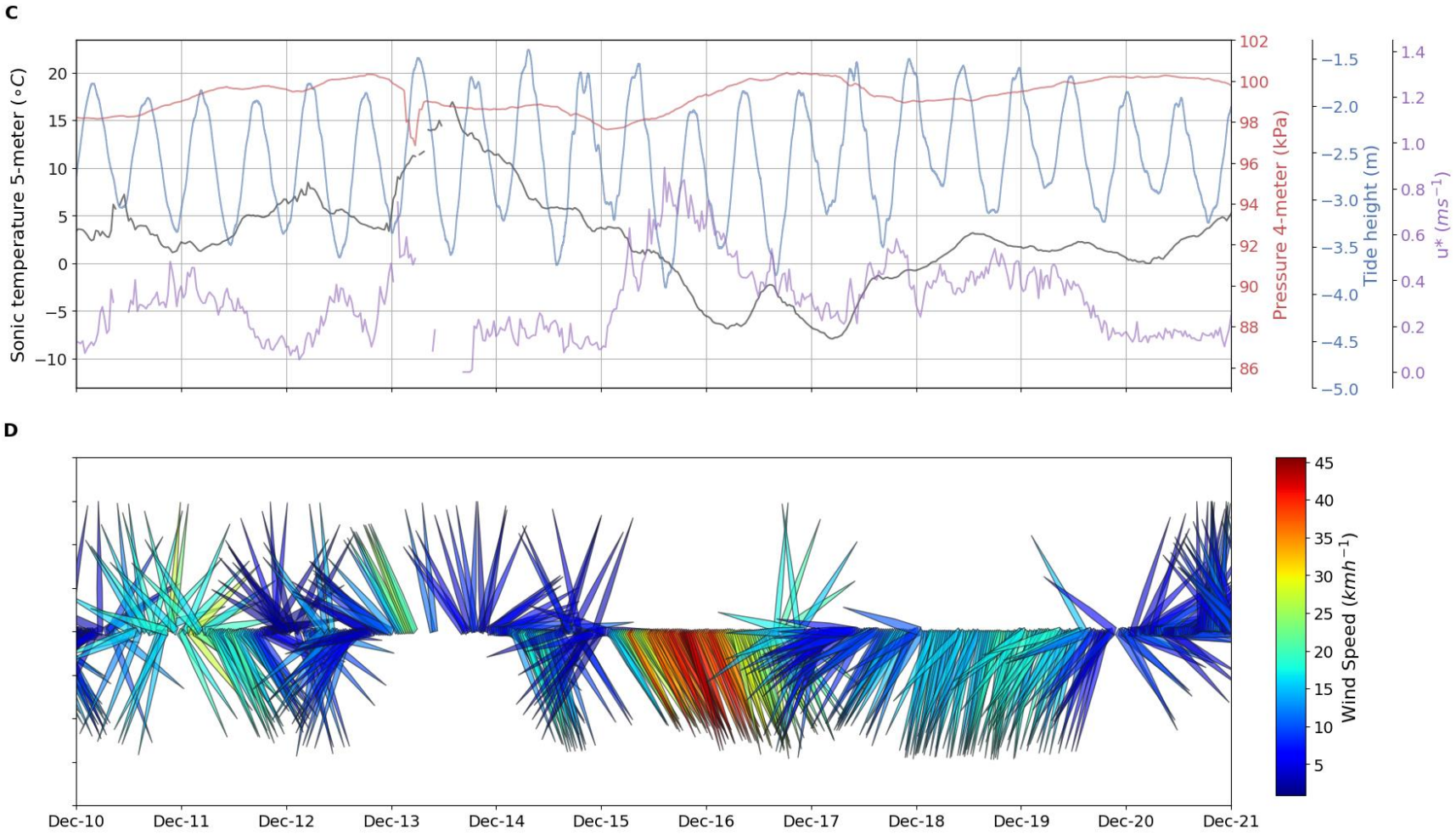

Figure 3-32: Ocean source event overview part 2. Panel C: Sonic temperature (black); gas analyzer sample cell pressure (red); tide height (blue); u* (purple) Panel D: Wind vectors (arrow points in the direction wind is travelling), and wind speed (color bar).

As a coupled measurement of wind and temperature covariance, heat flux is a parameter that clearly correlates well with the N_2O ocean source event as well as some smaller flux events during this time period. The sensible and latent heat fluxes are shown in Figure 3-33. Between December 15th and 12:00 noon on December 17th the total energy lost from the ocean surface was $37.24\ \mathrm{MJ\ m^{-2}}$, which is consistent with other measurements indicating a colder airmass flowing quickly over a warmer ocean. This heat loss is expected to cool the ocean and increase gas solubility, which creates conditions where N_2O is subsaturated and a negative flux of N_2O (into the ocean) is expected. In fact, a positive (out of ocean) N_2O flux was observed.

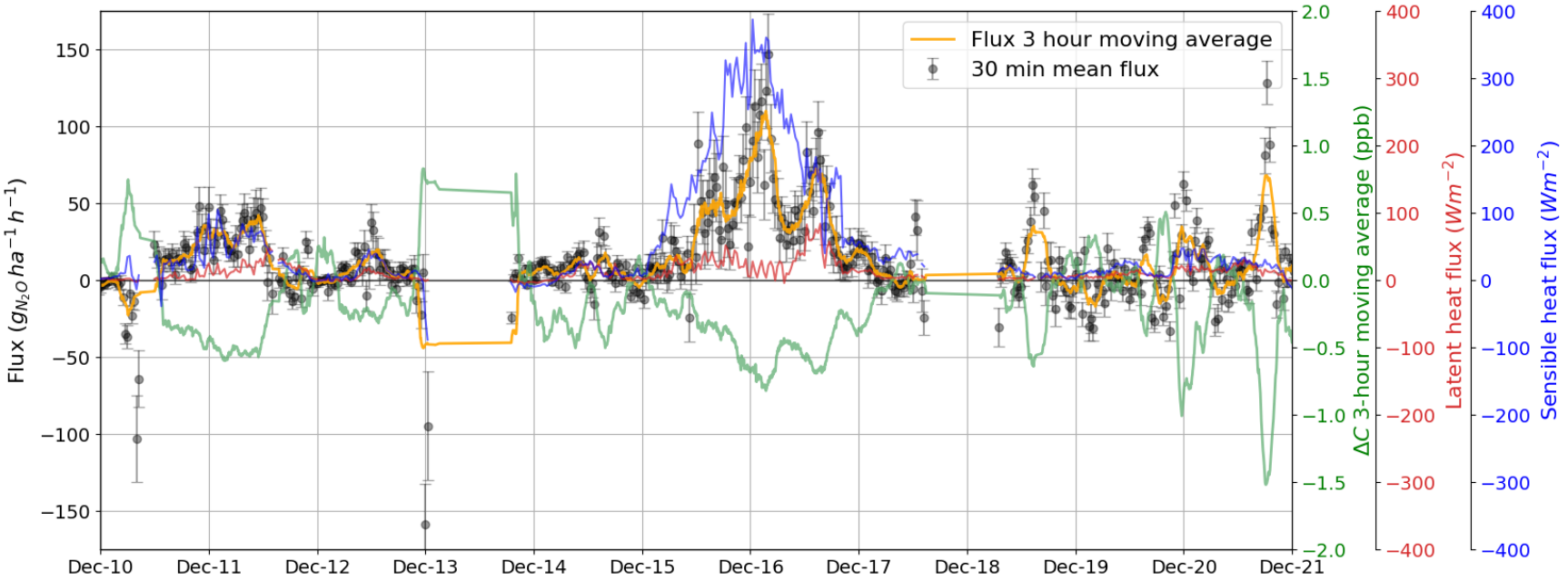

Figure 3-33: Top: N_2O ocean source event peaking on December 16th. Flux (black) correlates well with sensible (blue) and latent (red) heat flux. ΔC (green) also traces the shape of the flux peaks well.

Using the heat flux measurement from the 3-D sonic anemometer, an estimate of the ocean surface temperature change was calculated for a set of assumed mixed layer thicknesses being affected by the cooling. We assume all the heat moving away from the ocean surface is cooling a slab of the ocean to a fixed depth, d, so that the rate of temperature change is:

$$\Delta T_{slab} = \frac{-(H_s + L_e)(3600)(24)}{d * \rho_{slab} * Cp_{slab}},$$

where H_s and L_e are in units of Wm^{-2}, d is in meters and ΔT_{slab} is the sea surface cooling rate in $℃\,day^{-1}$. The sea surface specific heat, Cp_{slab}, was assumed to be $4000\,Jkg^{-1}K^{-1}$, and the density, ρ_{slab}, was assumed to be $1028\,kgm^{-3}$. As the extent of heat transfer to lower depths of the ocean was uncertain, we assumed a set of thicknesses being influenced by the strong surface cooling via wind-driven mixing and wave action. Figure 3-34 shows the estimated sea surface cooling for slab thicknesses of 0.01 m, 0.1 m, 1 m and 10 m. The 1-meter thickness shows cooling results (10°C / day) closest to the air temperature measurements from the jetty site and seems consistent with the order of magnitude expected for mixing depth with high winds (assuming no large-scale convective overturning). During the full length of the ocean source event, the mean cooling of the ocean surface for a 1-meter thickness was $-3.67\,℃\,day^{-1}$, and the total cooling during the event, which lasted 2.5 days, was -9.15 ℃. Assuming a surface salinity of around 30‰ at this time of year (Shi & Wallace, 2018), the solubility of N_2O during a sea surface cooling from 8 to -1 ℃ would increase from $3.511 \times 10^{-2}\ molkg^{-1}atm^{-1}$ to $4.989 \times 10^{-2}\ molkg^{-1}atm^{-1}$ (Weiss et al., 1980). A 42% increase in the solubility of N_2O in the ocean surface layer during this time suggests that the *different* cause of the N_2O ocean *source* event observed must indeed be very dominant over this solubility increase, which favours an ocean *sink*.

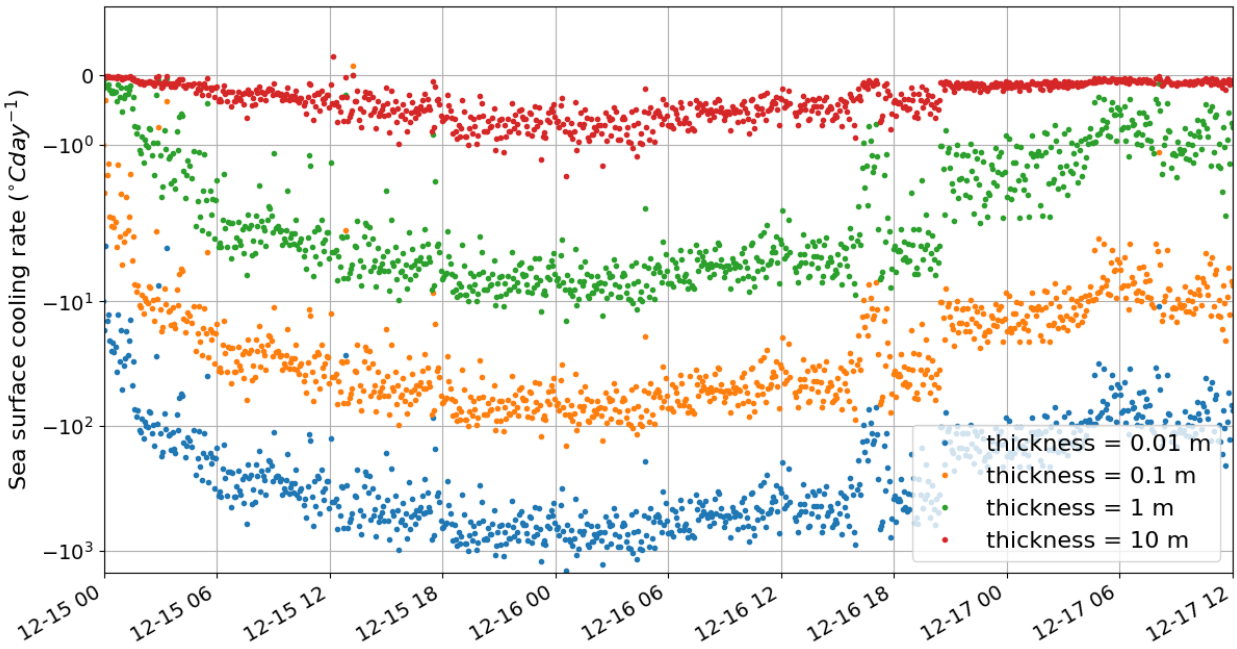

Figure 3-34: Estimated sea surface cooling rates for surface ocean slab thicknesses of 0.01 m, 0.1 m, 1 m and 10 m.

From Section 3.3.3 we saw that u* correlated well with the N_2O flux, with a possible explanation being that the limiting factor for gas transport from the surface is the aerodynamic resistance of the boundary layer (rather than the internal rate of gas production/consumption rate, or storage rate). Therefore, processes enhanced by high u* (possibly convection, buoyancy and/or surface waves) are a likely candidate for the driver of positive N_2O flux in Halifax Harbour during our observations. High wind inducing currents and mixing in the ocean surface could affect overturning of basin water and bring anoxic, N_2O-rich (N_2O supersaturated) waters to the surface. The rapid cooling of the ocean surface could also impact convection through buoyancy driven overturning of the slightly denser surface water (0.1% increased density for a 10℃ decrease in water temperature). Figure 3-35 shows a plot with N_2O flux, heat flux, and the concentration difference in the top panel, but for a different time period in spring 2021 (April 7th – April 13th), when buoy sea surface temperate (SST) data was available in Halifax Harbour (measured every hour). The bottom panel shows the sonic temperature, buoy SST as well as wind speed and u*. There are a series of smaller N_2O flux oscillations, there are negative (into ocean) dips that correlate well with wind speeds and u* as well as heat flux peaks (outlined in light blue on Figure 3-35). These dips also seem to correlate with diurnal peaks in air temperature which are also

somewhat visible in SST, though are lagged slightly later than the flux dips and wind peaks. These results motivate further analysis and study with regards to dynamical drivers of N_2O in the ocean surface, especially in a coastal environment. If wind is indeed a limiting factor of N_2O flux in Halifax Harbour, long-term continuous measurements with a high temporal frequency that captures short-term events will be needed to estimate annual totals. The ability to uncover information about subsurface production/consumption, whether measuring seasonal cycles or multi-year climate forcing effects, will also require high frequency measurements.

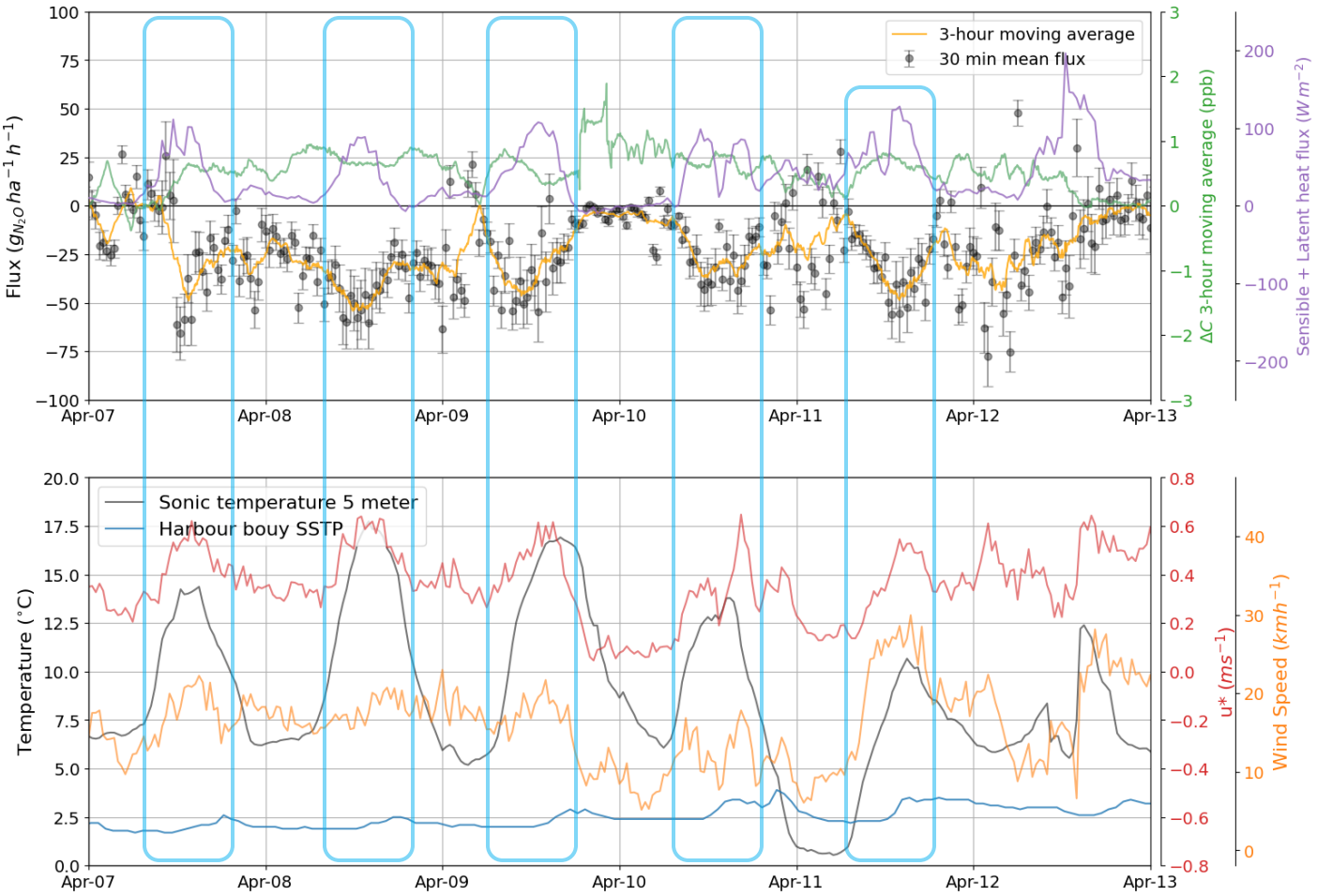

Figure 3-35: Top: N_2O flux (black), heat flux (purple) and ΔC (green). Bottom: Sonic temperature (black), Halifax Harbour buoy SST (blue), wind speed (orange) and u* (red). Peak features of interest are outlined (light blue).

4. Conclusion

4.1. Key results

In the course of this work, we derived N_2O fluxes using the flux-gradient approach, based on spectral FTIR gas measurements and 3-D sonic anemometer measurements in Halifax Harbour, spanning December 7th, 2020, to April 28th, 2021. The data completeness for the measurement period was 57% in 30-min observation bins, of which 69% revealed N_2O flux signals larger than their calculated uncertainties. During the observation period the ocean behaved as a net sink of N_2O and the sum of flux for the observed duration was $-10.81\ \mathrm{kg_{N_2O}ha^{-1}}$ (into ocean). The average N_2O flux was characterized by a similar magnitude and seasonal sign as the thermal N_2O flux component in a global ocean-atmosphere gas flux model of Manizza et al. (2012). Moreover, we found that powerful short-term emission and absorption events exist, which strongly motivate high frequency monitoring of gas flux. One such event was observed from December 15th to 17th 2020, when the ocean emitted $+2.00\ \mathrm{Kg_{N_2O}ha^{-1}}$ in the span of 2.5 days (a large portion of the total flux during the entire observation period). This ocean N_2O source event was shown to be consistent with high-frequency ocean surface dynamics, i.e., high winds cooling the harbour surface waters and driving the overturning of N_2O-saturated deeper waters in Bedford Basin. These types of events, if unobserved, appear to result in large errors in annual N_2O ocean emission totals, which reinforces the need for continuous monitoring in coastal environments. Finally, since physical processes will also be affected by rising temperatures and related climatic changes, this also motivates long-term observations to monitor the response of ocean-air N_2O exchange.

4.2. Achievements and reflections for improvements

The goal of this project was to demonstrate the performance of an OP-FTIR system used with the flux-gradient method to measure ocean-air fluxes of N_2O. This was accomplished and the process of doing so was very informative of what future work and further measurements may entail. Starting in September 2019, the OP-FTIR-FG method was first studied for application to ocean-air fluxes, focusing on preliminary data previously gathered in 2018 (without 3-D sonic measurements). I studied micrometeorological theory so as to be able to correctly adapt the instrumentation and flux formulation of Flesch et al. (2016) for the coastal location of Halifax Harbour. I tested for the optimal process to retrieve N_2O gas concentrations from spectra produced

by the OP-FTIR system. I also learned to use the 3-D sonic anemometer, customized the meteorological tower setup, and programmed the instrument for our experiment's particular requirements. In December 2020 we deployed the experiment for a fully-instrumented measurement campaign that lasted 5 months until the end of April 2021. I wrote extensive Python code and revised MATLAB code to analyze and reduce the concentration and wind data to produce reliable flux calculations, with rigorous uncertainties. From the data collected it is evident that the method's signal to noise ratio is sufficient to derive N_2O fluxes in Halifax Harbour. The results have given insight into the direction and magnitude of N_2O exchange at the ocean-atmosphere interface in this costal environment in winter and early spring.

We learned many details about the deployment of the equipment that can help future experiments run continuously and collect more complete data sets. We encountered frost heave in the ground below our spectrometer during extreme cold weather events. It is important to monitor for slowly degenerating IR signals in both paths (~12 h), which can be a sign of frost heave. Even on the waterfront, where the ocean regulates temperatures, there was enough shifting of shore structures due to ice to move our spectrometer out of alignment every few days in late winter. In future deployments it would be best to implement a regular schedule of alignment checks; it is worth exploring automation of the motorized tripod head's checking and centering of the beam on the highest return signal periodically. The usefulness of such automation would be applicable to many northern environments with freezing and thawing ground, as well as areas with significant erosion. For example, if our experiment were deployed to measure CH_4 fluxes on an Arctic coastline with melting permafrost, then the IR beam would likely need frequent re-aiming at the retroreflectors.

During analysis post experiment it became apparent that it would have been useful to collect two additional measurements that would be valuable in the future. The first is sea surface temperature at the measurement site. We had the capability to do this as we had an additional temperature probe, which in the end served a function that was not as useful as predicted in measuring temperature with a 3rd instrument at a lower height for approximating the temperature gradient. Sea surface temperature would have been much more valuable as it would have helped link the effects of gas solubility changes on gas fluxes due to sea surface cooling or heating (using the heat fluxes that we measured with the sonic anemometer). The second measurement that would be useful is a local log of weather, to help discern the amount of freshwater flux into the ocean;

this could include rain, snow or even snow melt, as snow-related parameters are not readily available from public sources – certainly not continuously nor co-located. In addition to a simple weather station like a Davis Vantage Pro Plus, which has a rain bucket, a well-positioned webcam could track snowfall as well as snow melt, although the measurement of surface salinity at the site (comprising a third useful measurement) would alleviate the complication of tracking and interpreting snow melt. While freshwater flux does influence gas solubility and therefore gas fluxes, the exact times of heavy rain are a blind spot when our instruments do not function. Therefore, the ability to flag alternative freshwater flux events (snow melt or post storm run-off) when the instruments do function could be an asset to future studies.

During my learning and use of the 3-D sonic anemometer I learned of further techniques that would help characterize the data, but these were not implemented due to time constraints. For eddy covariance measurements in urban locations with step changes in surface roughness it would be informative to model the footprint of the sonic instrument, or factor the step change itself into the calculations. In this project I only went as far as comparing sonic and flux results to wind direction and wind speed, as well as friction velocity, tide height and heat flux. Further insight may be gained using the high frequency sampling (10 Hz) of the sonic anemometer (as compared to the 4 m 19 s acquisition time of the spectrometer) to inverse-model the measurement fetch area for a better understanding of where the momentum flux is being measured and if obstructions could be interfering with flow. Another approach could be to model the surrounding structures and create CFD flow simulations for a set of regional wind directions and speeds. This would give an overview of where the flow is disturbed and no longer representative of the flow directly over water alone. It could also be possible to model the step change in surface roughness and, using measurements from a second anemometer tower in a different location, account for any perturbation to the flux calculation if one exists. For this project, where initial exploration was the goal, it was not feasible to dedicate the time or resources required to implement these ideas. Instead, a best guess for the deployment location of the sonic was made from visual observations on the jetty. However, for a future long-term experiment one, or a combination of these methods would ensure a truly optimal placement and processing of data from the instruments, safeguarding against discovering sampling bias issues after a lot of time and resources have been spent.

4.3. Future work

There are numerous paths to explore further with this project. The most obvious is a longer measurement period to capture both long-term trends and more short-term events. With setup details now familiar, the instruments could run continuously except during heavy rain and fog. A multi-year observation could have large implications for annual budgets and for predicting the effects of climate change on coastal N_2O flux.

OP-FTIR N_2O concentration difference data was also collected in September and October of 2018 and, as an extension to this measurement campaign, from May to December 2021 (albeit without the 3-D sonic anemometer). A method to approximately quantify the flux using available weather station data in the absence of a 3-D sonic anemometer was developed early in this work (Appendix B). This method is yet to be tested for accuracy using 2020/2021 sonic-instrumented data (when weather station data is also available) but could potentially be applied to the additional 2018 and 2021 (sonic-less) data.

There may be possibilities for simplifications to our experiment setup by sacrificing some accuracy and versatility that may lead to advantages such as ease of use, adoption in more locations, and redundancy when used along side OP-FTIR. The concentration difference, ΔC, was shown to be an excellent qualitative predictor of flux events. It could be worthwhile to look further into the data where ΔC and flux deviate from each other. Perhaps there is an approximation that could be used to roughly quantify flux in other measurement locations with simpler (non-sonic) instrumentation. The equipment could also be simplified if the target is only one specific gas, as opposed to the (multi-species) OP-FTIR measurement that requires complex spectral processing. For example, using two low-cost purpose built N_2O concentration sensors on a tower to get ΔC, would sacrifice the benefits of open path measurements but could then be deployed to more locations and potentially work in the rain as well. It may also be worth exploring different instruments for measuring the momentum flux, the vertical temperature profile and heat flux; perhaps a low cost 3-D anemometer or a tower of two cheap 2-D anemometers would do just as well for our needs as the Campbell Scientific 3-D sonic anemometer.

One major benefit of the data gathered with the OP-FTIR in this project has remained untapped, which is the ability to retroactively retrieve the concentrations for a variety of gasses encoded in the IR absorption spectra. Related to this, further retrievals of important interfering

species such as H_2O or even retrievals of temperature can in turn improve retrievals of N_2O. Methane (CH_4) is our next likely target for study using the data from the 2020/2021 campaign. After adjusting the parameters for retrieving methane and re-processing the spectra, CH_4 concentration differences can be used to calculate flux using the same sonic anemometer data. At the very least, this will answer what signal to noise ratio can be expected for methane fluxes derived using this setup, which would be useful for planning deployment to other locations, e.g., salt marshes. Successfully analyzing methane (and other gas fluxes) would also add to the understanding of mechanisms taking place in Bedford Basin.

Now that the air-side measurement of ocean-atmosphere N_2O flux is tested and demonstrated, a promising next step is to deploy our technique together with sea-side measurements. In fact, our work has already spurred further discussion with Dalhousie Oceanography about physical processes linking the atmospheric conditions to microbial communities in the depths of the Bedford basin, as well as provided motivation for further continual monitoring, in combination with expanded sea-side measurements by Dalhousie Oceanography. Through the design, deployment and analysis of this experiment, vital knowledge has been gained that will aid future measurement campaigns by reducing uncertainty around setup and expected results, while also flagging several pitfalls that can now be avoided.

References

Allen, S. K., Bindoff, N. L., France, F. B., Cubasch, U., Uk, M. R. A., France, O. B., Hesselbjerg, J., Denmark, C., France, P. C., Uk, M. C., Vasconcellos, V., & Feely, R. A. (2014). Technical Summary. *Climate Change 2013 - The Physical Science Basis*, 31–116. https://doi.org/10.1017/cbo9781107415324.005

Arévalo-Martínez, D. L., Steinhoff, T., Brandt, P., Körtzinger, A., Lamont, T., Rehder, G., & Bange, H. W. (2019). N2O Emissions From the Northern Benguela Upwelling System. *Geophysical Research Letters*, *46*(6), 3317–3326. https://doi.org/10.1029/2018GL081648

Arya, S. P. (2001). Introduction to micrometeorology. In R. Dmowska (Ed.), *Academic Press: International Geophysics Series* (2nd ed., Vol. 79). https://doi.org/10.1002/qj.49711649113

Bai, M., & Griffith, D. W. T. (2011). Methane Emissions from Livestock Measured by Novel Spectroscopic Techniques. *School Chemistry, Faculty of Science, PhD*, 293.

Bange, H., Freing, A., Kock, A., & LÖscher, C. (2010). Marine pathways to Nitrous Oxide. In *Nitrous Oxide and Climate Change* (pp. 36–62). Routledge. https://doi.org/10.4324/9781849775113

Bates, B. C. (Bryson C. ., Kundzewicz, Z., Wu, S., Palutikof, J., & Intergovernmental Panel on Climate Change. Working Group II. (2008). Climate change and water. In *Intergovernmental Panel on Climate Change. Working Group II*.

Cao, S., Zhang, J., & Su, W. (2018). Net Value of Wetland Ecosystem Services in China. *Earth's Future*, *6*(10), 1433–1441. https://doi.org/10.1029/2018EF000976

Capone, D. G., & Hutchins, D. A. (2013). Microbial biogeochemistry of coastal upwelling regimes in a changing ocean. *Nature Geoscience*, *6*(9), 711–717. https://doi.org/10.1038/ngeo1916

Diaz, R. J., & Rosenberg, R. (2008). Spreading dead zones and consequences for marine ecosystems. *Science*, *321*(5891), 926–929. https://doi.org/10.1126/science.1156401

Flesch, T. K., Baron, V. S., Wilson, J. D., Griffith, D. W. T., Basarab, J. A., & Carlson, P. J. (2016). Agricultural gas emissions during the spring thaw: Applying a new measurement technique. *Agricultural and Forest Meteorology*, *221*, 111–121. https://doi.org/10.1016/j.agrformet.2016.02.010

Flesch, T. K., McGinn, S. M., Chen, D., Wilson, J. D., & Desjardins, R. L. (2014). Data filtering for inverse dispersion emission calculations. *Agricultural and Forest Meteorology*, *198–*

199, 1–6. https://doi.org/10.1016/j.agrformet.2014.07.010

Flesch, T. K., Prueger, J. H., & Hatfield, J. L. (2002). Turbulent Schmidt number from a tracer experiment. *Agricultural and Forest Meteorology*, *111*(4), 299–307. https://doi.org/10.1016/S0168-1923(02)00025-4

Forster, G., Upstill-Goddard, R. C., Gist, N., Robinson, C., Uher, G., & Woodward, E. M. S. (2009). Nitrous oxide and methane in the Atlantic Ocean between 50°N and 52°S: Latitudinal distribution and sea-to-air flux. *Deep-Sea Research Part II: Topical Studies in Oceanography*, *56*(15), 964–976. https://doi.org/10.1016/j.dsr2.2008.12.002

Freing, A., Wallace, D. W. R., & Bange, H. W. (2012). Global oceanic production of nitrous oxide. *Philosophical Transactions of the Royal Society B: Biological Sciences*, *367*(1593), 1245–1255. https://doi.org/10.1098/rstb.2011.0360

Gordon, I. E., Rothman, L. S., Hill, C., Kochanov, R. V., Tan, Y., Bernath, P. F., Birk, M., Boudon, V., Campargue, A., Chance, K. V., Drouin, B. J., Flaud, J. M., Gamache, R. R., Hodges, J. T., Jacquemart, D., Perevalov, V. I., Perrin, A., Shine, K. P., Smith, M. A. H., … Zak, E. J. (2017). The HITRAN2016 molecular spectroscopic database. *Journal of Quantitative Spectroscopy and Radiative Transfer*, *203*, 3–69. https://doi.org/10.1016/j.jqsrt.2017.06.038

Griffith, D. W. T. (1996). Synthetic calibration and quantitative analysis of gas-phase FT-IR spectra. *Applied Spectroscopy*, *50*(1), 59–70. https://doi.org/10.1366/0003702963906627

Hershey, R. N., Bijoy Nandan, S., P.R., J., Vijay, A., K., N. V., & V., S. (2019). Nitrous oxide flux from a Tropical estuarine system (Cochin estuary, India). *Regional Studies in Marine Science*, *30*, 100725. https://doi.org/10.1016/j.rsma.2019.100725

IPCC. (2007). The Physical Science Basis. Contribution of Working Group I of the IPCC (Summary for Policymakers). *Cambridge University Press*.

IPCC. (2013). The Physical Science Basis. Contribution of Working Group I to the Fifth Assessment Report of the Intergovernmental Panel on Climate Change. *Cambridge University Press*. https://doi.org/10.1017/CBO9781107415324.Summary

Jones, E. P., & Smith, S. D. (1977). A first measurement of sea-air CO 2 flux by eddy correlation. *Journal of Geophysical Research*, *82*(37), 5990–5992. https://doi.org/10.1029/JC082i037p05990

Kumari, V. R., Sarma, V. V. S. S., Rao, G. D., Viswanadham, R., Navita, B., Srinivas, T. N. R.,

Krishna, M. S., & Reddy, N. P. C. (2019). Modifications in the trace gases flux by a very severe cyclonic storm, Hudhud, in the coastal Bay of Bengal. *Journal of Earth System Science*, *128*(5). https://doi.org/10.1007/s12040-019-1157-y

Laperriere, S. M., Nidzieko, N. J., Fox, R. J., Fisher, A. W., & Santoro, A. E. (2019). Observations of Variable Ammonia Oxidation and Nitrous Oxide Flux in a Eutrophic Estuary. *Estuaries and Coasts*, *42*(1), 33–44. https://doi.org/10.1007/s12237-018-0441-4

Manizza, M., Keeling, R. F., & Nevison, C. D. (2012). On the processes controlling the seasonal cycles of the air–sea fluxes of O 2 and N 2 O: A modelling study . *Tellus B: Chemical and Physical Meteorology*, *64*(1), 18429. https://doi.org/10.3402/tellusb.v64i0.18429

McLeod, E., Chmura, G. L., Bouillon, S., Salm, R., Björk, M., Duarte, C. M., Lovelock, C. E., Schlesinger, W. H., & Silliman, B. R. (2011). A blueprint for blue carbon: Toward an improved understanding of the role of vegetated coastal habitats in sequestering CO2. *Frontiers in Ecology and the Environment*, *9*(10), 552–560. https://doi.org/10.1890/110004

Oberle, F. K. J., Gibbs, A. E., Richmond, B. M., Erikson, L. H., Waldrop, M. P., & Swarzenski, P. W. (2019). Towards determining spatial methane distribution on Arctic permafrost bluffs with an unmanned aerial system. *SN Applied Sciences*, *1*(3). https://doi.org/10.1007/s42452-019-0242-9

Power, C., (2021). *On Path Length, Beam Divergence, and Retroreflector Size in Open Path FTIR Spectroscopy*. BSc.

Rebmann, C., Kolle, O., Heinesch, B., Queck, R., Ibrom, A., & Aubinet, M. (2012). Data Acquisition and Flux Calculations. In M. Aubinet, T. Vesala, & D. Papale (Eds.), *Eddy Covariance: A Practical Guide to Measurement and Data Analysis* (pp. 59–83). Springer Netherlands. https://doi.org/10.1007/978-94-007-2351-1_3

Ricaud, P., Attié, J. L., Chalinel, R., Pasternak, F., Léonard, J., Pison, I., Pattey, E., Thompson, R. L., Zelinger, Z., Lelieveld, J., Sciare, J., Saitoh, N., Warner, J., Fortems-Cheiney, A., Reynal, H., Vidot, J., Brooker, L., Berdeu, L., Saint-Pé, O., … Zwaaftink, C. G. (2021). The Monitoring Nitrous Oxide Sources (MIN2OS) satellite project. *Remote Sensing of Environment*, *266*(September). https://doi.org/10.1016/j.rse.2021.112688

Roland, S. (2006). 9 - The Atmospheric Boundary Layer. In J. M. Wallace & P. V Hobbs (Eds.), *Atmospheric Science (Second Edition)* (Second Edi, pp. 375–417). Academic Press. https://doi.org/https://doi.org/10.1016/B978-0-12-732951-2.50014-4

Shi, Q., & Wallace, D. (2018). A 3-year time series of volatile organic iodocarbons in Bedford Basin, Nova Scotia: A northwestern Atlantic fjord. *Ocean Science*, *14*(6), 1385–1403. https://doi.org/10.5194/os-14-1385-2018

Thomson, A. J., Giannopoulos, G., Pretty, J., Baggs, E. M., & Richardson, D. J. (2012). Biological sources and sinks of nitrous oxide and strategies to mitigate emissions. *Philosophical Transactions of the Royal Society B: Biological Sciences*, *367*(1593), 1157–1168. https://doi.org/10.1098/rstb.2011.0415

Voss, M., Bange, H. W., Dippner, J. W., Middelburg, J. J., Montoya, J. P., & Ward, B. (2013). The marine nitrogen cycle: Recent discoveries, uncertaintiesand the potential relevance of climate change. *Philosophical Transactions of the Royal Society B: Biological Sciences*, *368*(1621). https://doi.org/10.1098/rstb.2013.0121

Wanninkhof, R. (1992). Relationship between wind speed and gas exchange over the ocean. *Journal of Geophysical Research*, *97*(C5), 7373. https://doi.org/10.1029/92JC00188

Wanninkhof, R., Asher, W. E., Ho, D. T., Sweeney, C., & McGillis, W. R. (2009). Advances in Quantifying Air-Sea Gas Exchange and Environmental Forcing. *Annual Review of Marine Science*, *1*(1), 213–244. https://doi.org/10.1146/annurev.marine.010908.163742

Weiss, R. F., Price, B. A., Canada, E., Rochette, P., Hutchinson, G. L., Jayasundara, S., & Wagner-Riddle, C. (1980). N I T R O U S Oxide S O L U B I L I T Y in Water and Seawater. *Agricultural Systems*, *8*(47), 247–286.

Wiacek, A., Li, L., Tobin, K., & Mitchell, M. (2018). Characterization of trace gas emissions at an intermediate port. *Atmospheric Chemistry and Physics*, *18*(19), 13787–13812. https://doi.org/10.5194/acp-18-13787-2018

Wilson, S. T., Al-Haj, A. N., Bourbonnais, A., Frey, C., Fulweiler, R. W., Kessler, J. D., Marchant, H. K., Milucka, J., Ray, N. E., Suntharalingham, P., Thornton, B. F., Upstill-Goddard, R. C., Weber, T. S., Arévalo-Martínez, D. L., Bange, H. W., Benway, H. M., Bianchi, D., Borges, A. V., Chang, B. X., … Yurganov, L. N. (2020). Ideas and perspectives: A strategic assessment of methane and nitrous oxide measurements in the marine environment. *Biogeosciences*, *17*(22), 5809–5828. https://doi.org/10.5194/bg-17-5809-2020

Zhan, L., Wu, M., Chen, L., Zhang, J., Li, Y., & Liu, J. (2017). The air-sea nitrous oxide flux along cruise tracks to the Arctic ocean and Southern Ocean. *Atmosphere*, *8*(11).

https://doi.org/10.3390/atmos8110216

Appendix

A. Logs

A.1. Campaign Log - Martin

November 23rd.
-Retros and movirda built and ratchet secured
-mobile battery stored in shed
-Heavy SW winds
-Sonic position determined by walking the jetty and flow around obstruction principles

- Instead of putting it at one end facing the predominant wind direction a position near the middle of the jetty was chosen
- The furthest away from obstacles and edge effects of the end of the jetty

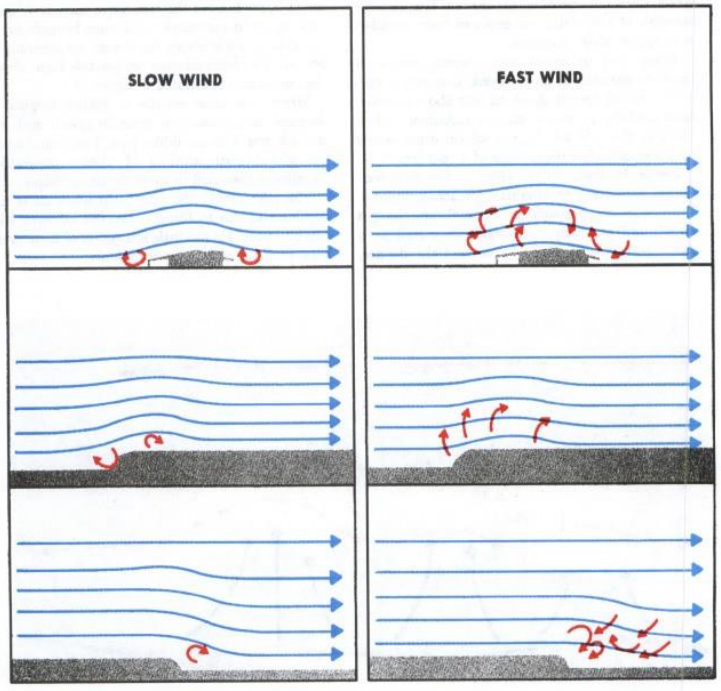

Nov 26
-Setup spectrometer at DND
-Need car pass and Padlock key to access
-Found retros are angled ~20 degrees away from container causing obstruction
-Measured offset and water level at two times

Dec 4
voltage at battery 116V

Dec 7 sonic running
-Water level at both sides at the same time
-offset to retros at jetty
-calculated path heights for instruments
-sonic orientation input 252deg W (true north setting)
- using phone, photos, building across the water and checked in maps

Dec 11

- Download 1
- Water jetty calibration level taken
- sonic time 1 hour ahead of pc time, not going to change it (laptop was in AST at this time in dec, so that would be AST +1, which is ADT, makes sense because I would have synced to laptop in November while getting the sonic ready and it was still ADT)
- retro moved between 12-2pm

Dec 16

- Download 2
- Temp probe discovered damaged and repaired temporarily (Martin July 20th, 2022: remember distinctly that the probe was hanging close to the ocean surface when found at low tide and at higher tide would have been underwater. Didn't seem important to mention until now.)
- Water level data downloaded caught up (ast+4 time zone)

Dec 18

- repaired/shortened temp probe mounting, bad temp data around 14:30
- moved retros at 15:30

Dec 22
download 3

dec 29
download 4 (one day late)

- noticing that irga also has errors when the weather is very bad, not outside the region where the sonic stops working though and works fine after, humidity related?
- found out FTS hasn't been running last 6 days
- weather has been SW to NW wind flips, weekly cycles, temps ranging up to 12C lots of rainfall to -5 on the flip with light flurries

jan5 download
Jan 11 download

- bent back temp probe shield (license plate)
- there are differences in the accuracy of temp sampling
    - the temp probe is exposed to sunlight in the morning and evening, and reflected sunlight all day
    - outdoor calibration run would be good
    - indoor calibration regardless

Jan 26 measure sonic ins heights from tidal offset point
temp probe: 0cm
gas cell: 148cm
sonic: 128+148 = 276

progress report to committee

- site photos/setup
    - paths/heights
- water level calibration
    - tidal data

- temperature readings
    - calibration notes measurement in same room
- u* findings
    - weather dropouts and ftir similarity
- stray light spectrum
- 2018 approx flux plot

Feb 2 download - something obstructed the ir path
Took images of the harbour

Feb 8,12 downloads without reset - hike in so kept it short so the laptop wouldn't be damaged in the cold

- This means that the record numbers will be continuous from feb 2nd
- I don’t think is an issue unless rec num gets too high, will keep an eye on it

Feb 18

- download
- pump filter has ice in it
- work crew on jetty

feb 24

- walked the jetty again 14:00-15:00
- NW winds steady winds 22km
- winds similar laminar and fast at both ends of the jetty
    - low pressure flow around the obstacles, possibly the less true option if so
- where the sonic is it is close but slightly lighter and more intermittent
    - could be dockside creating eddy
- not sure which is more representative of the water

Mar 04

- the gas analyzer signal level went below tolerance for a couple days
- at 1:45-2:15pm I turned the sonic off to clean the windows
- H2O signal increased from 0.78 to 0.89
    - cut off is 0.8

Mar 12

- 15:00 walked the jetty again
- dock is warmer than the water
- wind off the water is cold
- think I expect an upward component of the jetty
    - hand test over the edge
- and a turbulent component
- check
    - cfd simulations
    - recommended height of instruments over surface features

April 12

- download
- cone in front of lower retro

- likely obstruction by work crews past week

April 22

- short rain, intermittent sun, high wind
- transducer clear while raining could be an interesting time to look at

April 28

- look at temp grad vs sun
    - jetty will heat up faster than water
    - temp probe closest to water
    - sample cell closest too jetty
    - sonic furthest from both

Table 9: Download log

Datetime	Checked instrument (Cables, rigging secure, green lights)	transducers	Pump condition	Download and Backup: Laptop,USB,OneDrive	Check data table updated on laptop (dates)	Cleared program, table data	resend /run all, check pump flow (7), sonic az (252)	data gap	data notes
Dec 11, 10:30	y	clear	light debris, no water	y,y,y	y	y	y,y,y	10min	bad/no data on dec 10 6-15:00 due to weather rain and sleet snow, u* looks good for flux most of the time
Dec 16, 12:37	temp probe bashed off, cable intact, still measuring, it was hanging down about 1m so probably didn't touch water at high tide	clear	no change	y,y,y	y	y	y,y,y	15min	temp probe inverts with cell temp on dec 15 8:00am, might be when the probe fell down. Data loss 00:00 dec 13- 00:00 dec14 looks like a storm (high rains, snow, wind recently), high momentum flux on dec 15
Dec 22, 9:24	y	y	no change	y,y,y	y	y	y,y,y	12min	dec 21 11:00 brief diag irga, big sonic drop out dec 21 6:00 to dec 22 6:00
Dec 29 12:00	y, wood might be wearing but probe looks okay	y	no change	y,y,y	y	y	y,y,y	15	late download lost dec 22 10:14 to dec 23 12:59 (max records 8639), weather losses on dec 26 15-21:00, 29 7:30-9:30
Jan 5 13:00	y,floats higher than probe but no damage	y	no change	y,y,y	y	y	y,y,y	15	weather drop outs 12:00 dec 31, 12:00 jan2 to 12:00 jan3, missed 12hours on dec 29 due to late back up
Jan 11 11:00	y	y	no change	y,y,y	y	y	y,y,y	12	light intermittent losses, 1400 jan 5, 00:00-03:00 jan 7
Jan 15 11:30	y	y	no change	y,y,y	y	y	y,y,y	15	rain event jan 14 16:00 to 15 10:00
Jan 21	y	y	no change	y,y,y	y	y	y,y,y	15	

Jan 27 11:45	y	y	no change	y,y,y	y	y	y,y,y	15	
Feb 2 14:00	heavy weather not checked	heavy rain	no opened	y,y,y	y	y	yyy	15	White caps in harbour, heavy wind and rain
Feb 8	y	y	no change	y,y,y	y	n	n,y,y	0	hiked in due to snow, kept time short so laptop wasnt damaged by cold
Feb 12	y	y	no change	y,y,y	y	n	n,y,y	0	hiked in due to snow, kept time short so laptop wasnt damaged by cold
Feb 18	y	y	ice build up	y,y,y	y	y	y,y,y	15	workers on jetty, potential blocked signal intermittent, weather drop out feb 10,14
Feb 24	y	y	ice decreased	y,y,y	y	y	yyy	15	steady data, co flux corr with rain events too?
Mar 3	y	y	ice still there, maybe less?	y,y,y	y	y	yyy	15	h2o signal too low, window cleaning needed
Mar 12	y	y	a small amount of ice left	yyy	y	y	yyy	15	
Mar 22	y	y	no change	y,y,y	y	y	yyy	15	
Mar 29	y	n rain	not checked	yyy	y	y	yyy	15	rainy, sonic diag 1,9
Apr 6 13:56	y	y	little water ice	yyy	y	y	yyy	15	miss days due to holiday, sonic cable cut
Apr 12 2:13 PM	y	y	less water	yyy	y	y	yyy	10	time is back to the station time, 30 sec ahead of pc server
Apr 16 12:13	y	y	not checked	yyy	y	y	yyy	10	
Apr 22 14:38	y	y	no change	yyy	y	y	yyy	10	
Apr 28 11:47	y	y	clear of water	yytodo	y	y	yyy	10	

Table 10: Water Level Log

Date DND	Time DND	dnd (cm)	Date Jetty	Time jetty	jetty		
offset	offset	spect:+150	offset	offset	bott:+26	top:+303	
Nov 26	11:30	245					
Nov 26	14:27	208					
Dec 4	10:39	103	Dec 4	10:39	188	sonic 182	sonic alt offest = -6
			Dec11	13:13	311		
Dec 18	16:15	222	Dec 18	14:42	276		
			Dec22	9:40	277		
			Dec 29	11:46	305		
			Jan 5	12:42	160		
			Jan 11	10:49	310		
			Jan 15	11:12	205		
			Jan 27	12:23	308		
			feb 2 too wavy				
			Feb 12	14:51	344		
			Feb 18	15:00	246		
			Mar 4	14:24	229		
			Apr 6	14:35	237		~240 slipping tape measure end

B. Flux approximation for 2018 data

Measurements in 2018 were done with dedicated wind measurements at a 2-meter height. Later we were able to source measurements at 10 meters for the time period from a nearby METOC station at CFB Halifax. Allowing for the same assumptions as above K_m can be approximated as follows. The first step is finding the gradient Richardson number using the following equation from (Arya, 2001).

$$Ri_m = \frac{g}{T_0}\frac{\Delta\Theta z_m}{(\Delta U)^2}\ln\frac{z_2}{z_1}$$

This is at the geometric mean height $z_m = \sqrt{z_1 z_2}$ which in this case is 4.5 meters. Ri is related to the M-O stability parameter as,

$$\zeta = Ri \qquad Ri < 0$$

$$\zeta = \frac{Ri}{1 - 5Ri} \qquad 0 \le Ri \le 0.2\ .$$

These relations are only valid for a moderate stability range for example: $-2 < \zeta < 0.2$. The Obukhov Length is then $L = z/\zeta$. From which the M-O flux profile similarity relation for momentum is found as,

$$\phi_m = (1 - 15\zeta)^{-1/2} \qquad \zeta < 0$$

$$\phi_m = 1 + 5\zeta \qquad \zeta \ge 0\ .$$

Which can then be used to find the friction velocity u_*:

$$u_* = {k_v \Delta U}\Big/{\left(\phi_m \ln\frac{z_2}{z_1}\right)}\ .$$

The eddy diffusivity of momentum is then:

$$\frac{K_m}{k_v z u_*} = \begin{cases} (1 - 15Ri)^{1/4} & Ri < 0 \\ 1 - 5Ri & 0 \le Ri \le 0.2 \end{cases}.$$

Which can be input into the flux gradient equations.

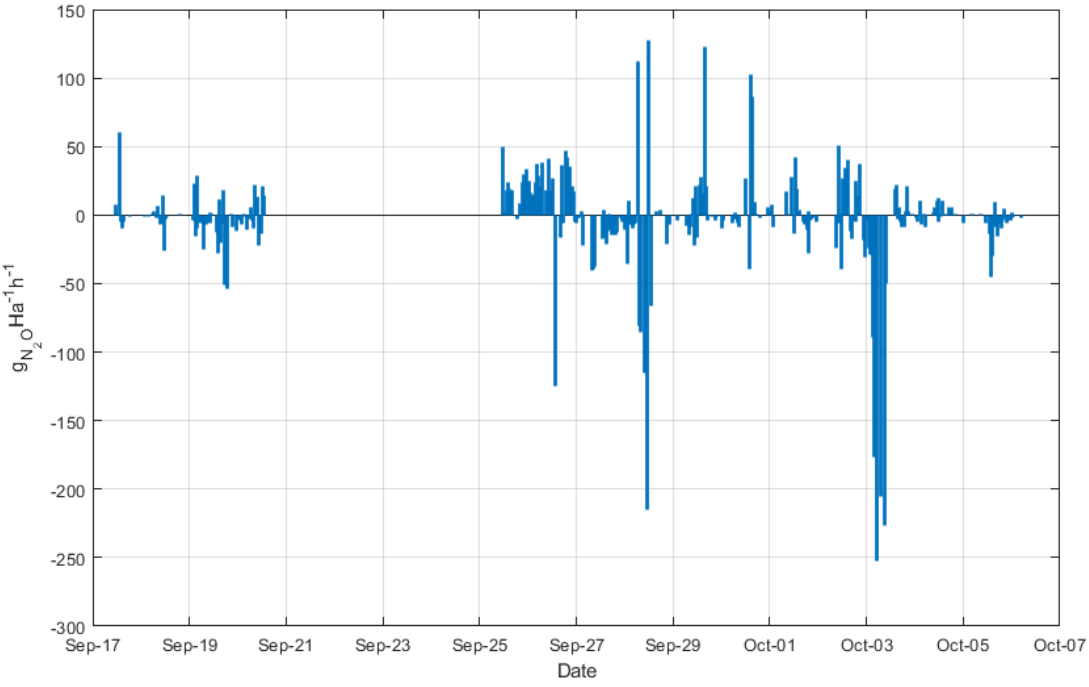

A preliminary estimate of N_2O flux for the 2018 measurements using the derivation above.

C. Additional Retrieval Sensitivity Testing

C.1. Retrieval test with O_3 component

Additional figures from the test retrievals performed including O_3.

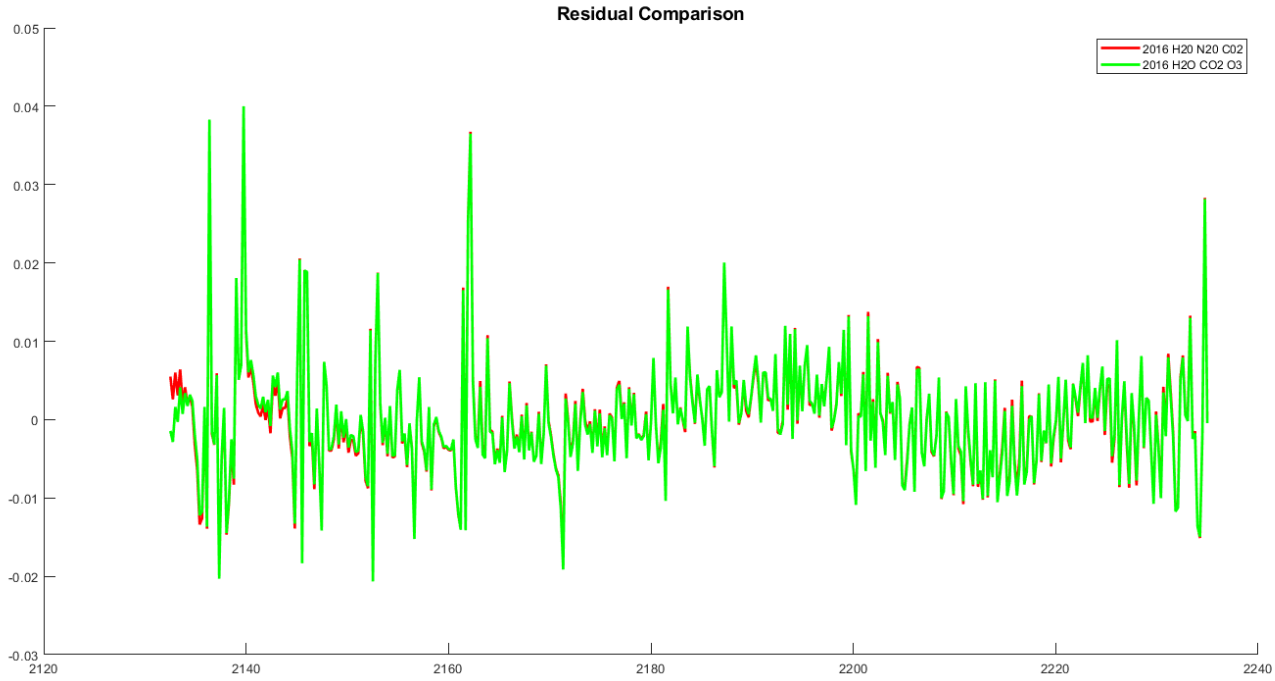

Effect on residuals of adding O3 and extending the retrieval window.

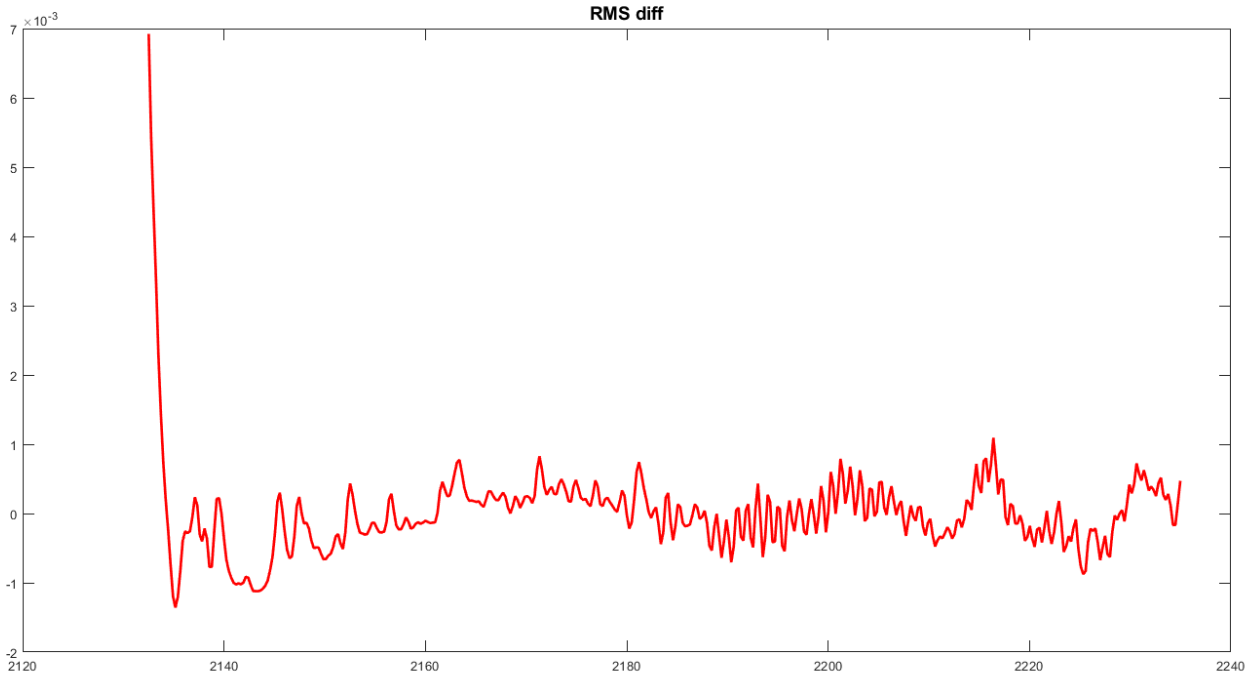

Effect on residual difference of adding O3 and extending the retrieval window.

C.2. Retrieval sensitivity to H_2O

From retrievals for the date range of August 2 to September 14, 2018 the fit RMS was also found previously. These dates are from the longest phase of the campaign before the setup was changed to accommodate the vertically separated retroreflectors for two measurement paths. I did several investigations using fit RMS to understand if different conditions affected the retrievals in anyway. I compared all of instrument's parameters and retrieved gasses to fit RMS as well as N_2O concentration from another instrument. One result of this was that the retrievals in the selected window are affected by the presence of H_2O. With higher humidity conditions reducing fit accuracy by up to 15%.

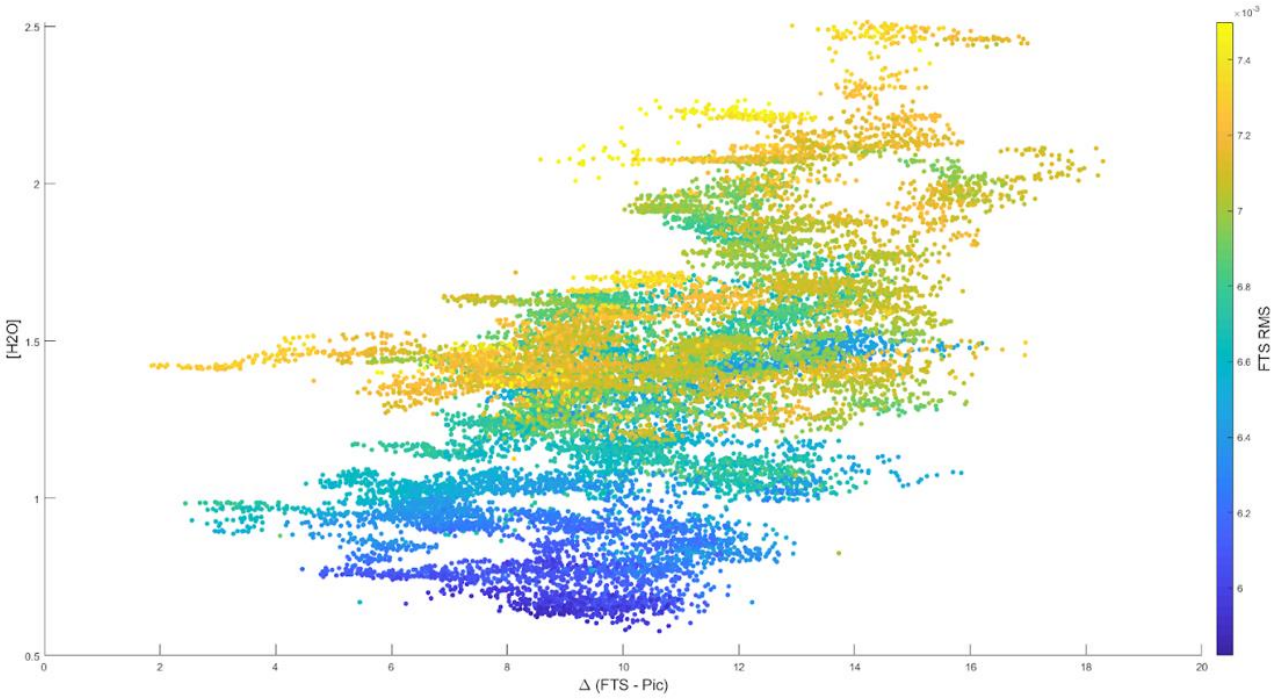

Show the relation between H_2O concentration (y axis) the difference between our OP-FTIR instrument (FTS) and another collocated instrument (Picaro) measuring the point concentration of N_2O (x axis). The colour axis represents Fit RMS.

Another potentially useful discovery is that the fit RMS drops to as much as 50% of the typical value when compared to the later vertical campaign phase. Figure 2-16 shows the rms vs time for the single path campaign. Some clumped date ranges jump between fit RMS values of 0.07, 0.1 and 0.14. In the later vertical campaign fit RMS values for all dates are ~ 0.14. These clumps also show up in

different windows being used for the retrieval of other species. I compared every parameter individually against these clumps, but none could explain the step changes seen in rms at these times. There are two paths of investigation yet to be attempted that could help understand why this is happening and if future measurements could be improved by controlling for the cause of these events. Looking at the correlation between fit parameters to see if any co-varying relationships explain the step changes. Separating the fit RMS calculation to use two sub-windows to see if the fit RMS from one absorption line group has more significance to these events than the other.

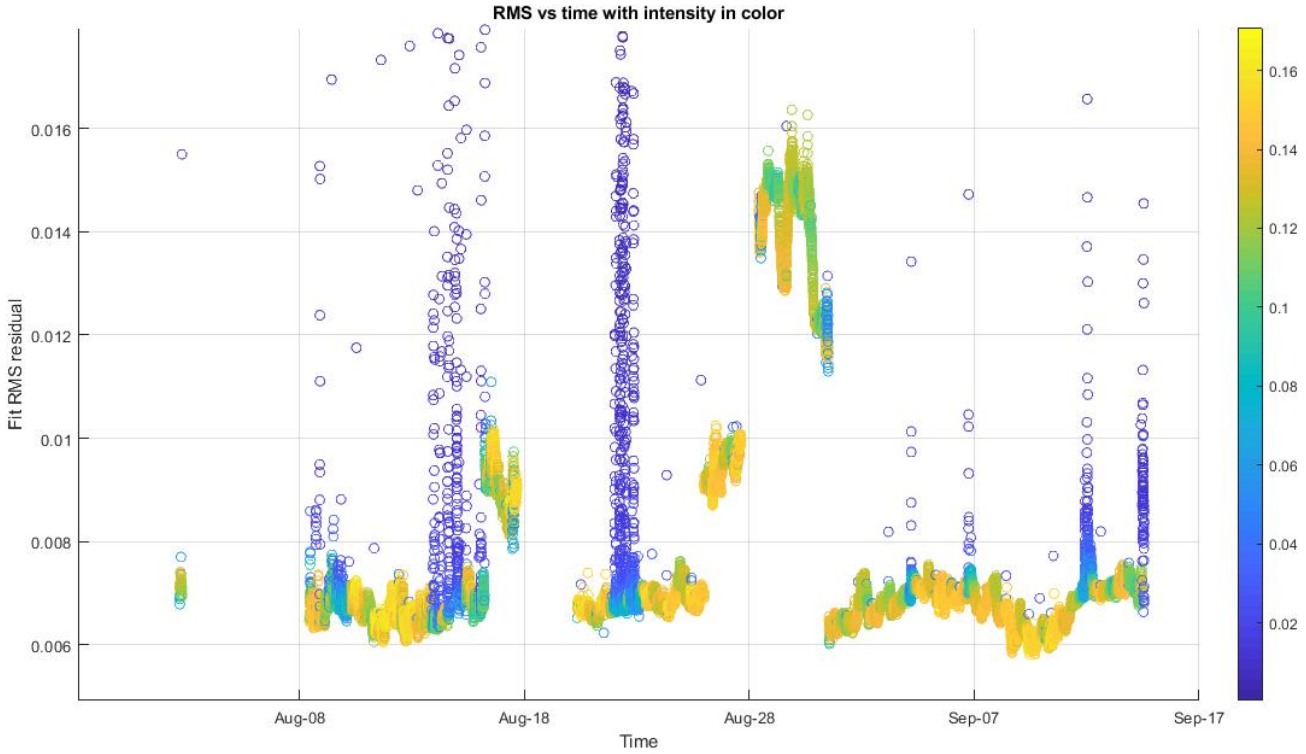

Fit RMS over time with signal strength at the 2500 cm^{-1} line. High RMS can be explained by low signal most of the time. However, for certain date ranges, such as around August 28, there is a step change where the Fit RMS doubles and signal strength remains unchanged.

C.3. FOV simulation

In the process of retrieving the vertical concentration difference I also investigated the retrieval method. The goal was to get familiar with all the factors involved, to check that the method was appropriate and find out if there are improvements that could be made. I simulated spectra to check the sensitivity of the retrievals to varying parameters. An example is shown in **Error! Reference source not found.** and 10 where I was looking at an instrument parameter called field of view (FOV). The question here was whether small inaccuracies in FOV could affect the gas spectra

fitting accuracy and weather fitting that parameter would be effective. Since the derived concentration of the gas would not change, even with much larger inaccuracies in FOV than are possible, it was decided that fitting this parameter would be an inefficient use of the parameter space.

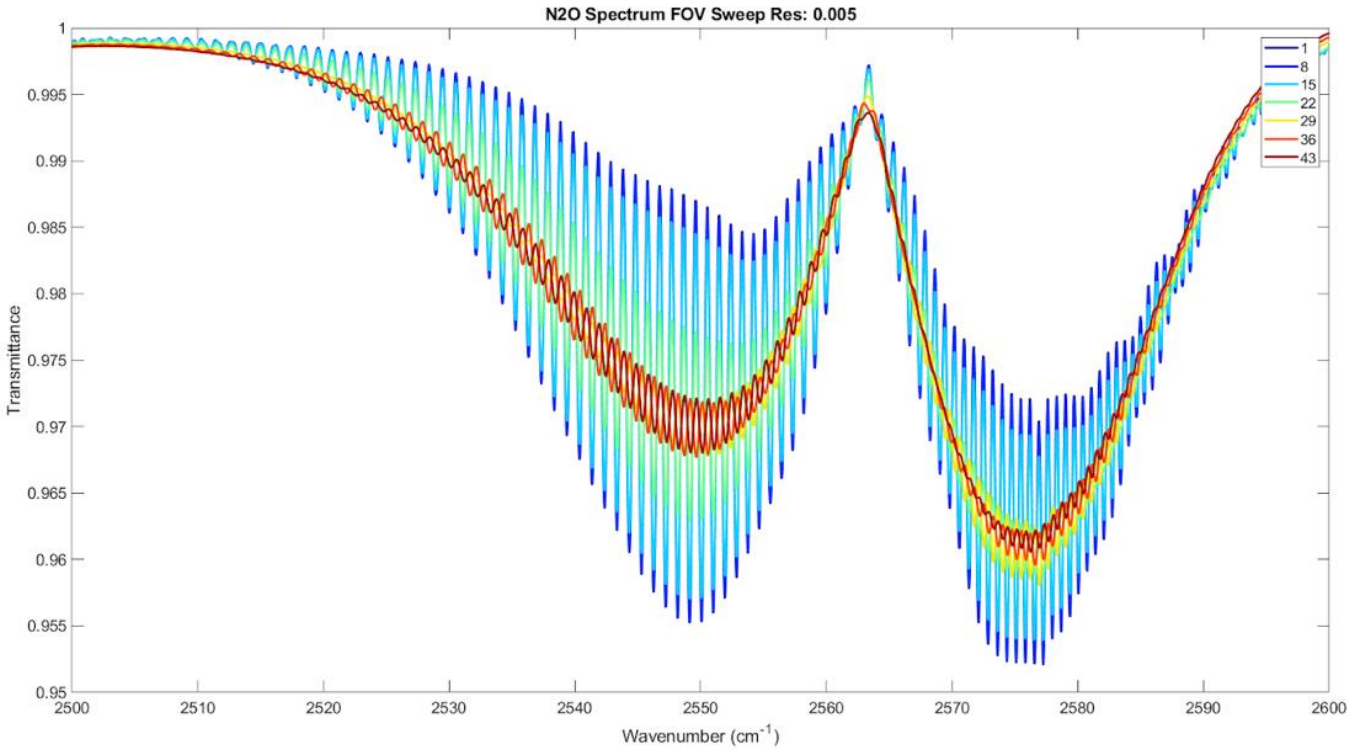

The simulated spectrum of N_2O for varying values of FOV (1,8,15,22,29,35,43). The discrepancy between fitted FOV and the calculated FOV for the instrument was of the order 0.1.

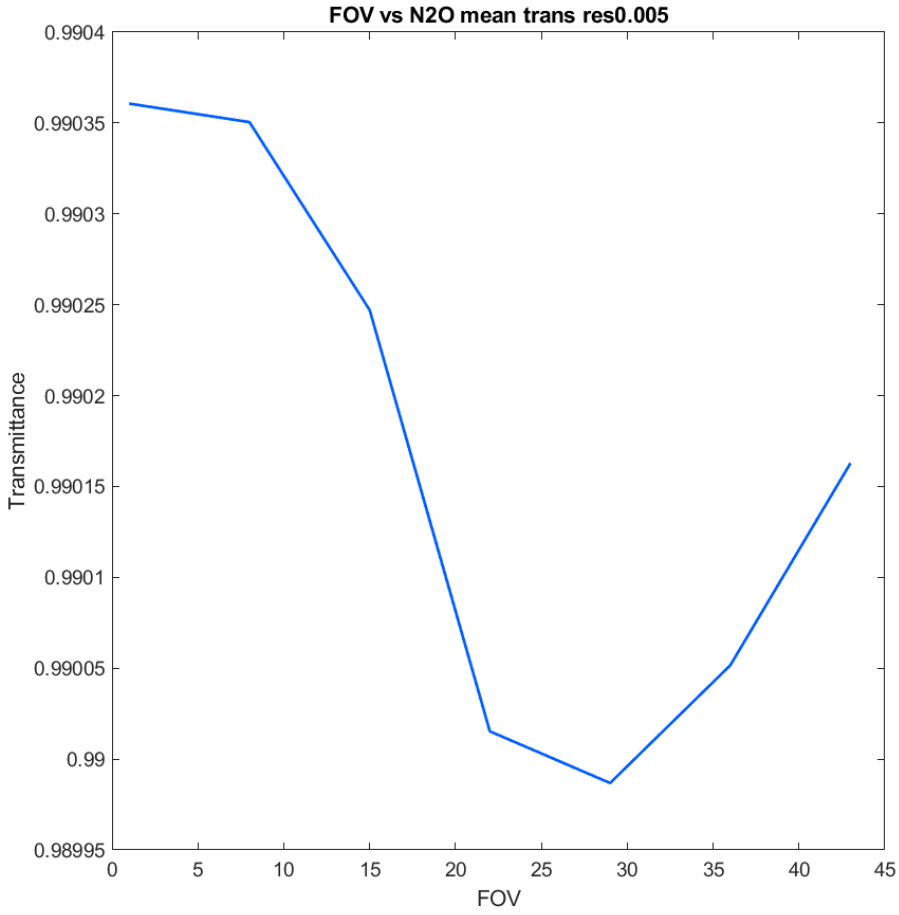

The mean transmittance is proportional to area under the spectrum and the concentration of N_2O. It changes an insignificant amount over a large range of FOV.

D. Note on temperature probe during the December 16th event

The high winds and wind waves during this event damaged the mounting for a temperature probe at the 3-D sonic anemometer tower site. Originally the probe was at the same height as the jetty, however during the period between 7:00 am on December 15th and 12:30 pm on December 16th the probe was hanging near the water surface and likely experienced some sea spray. A picture of the jetty edge on the same day as the source event is shown in the photo below during a site visit when it was discovered that the probe had fallen off and was retrieved. On the figure below the temperature of the probe, sample cell and 3-D sonic are compared. The probe is thought to have fallen close to the water on 7:00 am on December 15th because its temperature reading, which is lower than the other two instruments, suddenly became higher, again dropping lower after the mounting was repaired at 12:30 pm on December 16th. During the time when the probe was

dangling above the water, its temperature drops at the same rate as the air temperature. This accident has gives a small clue that rapid cooling was taking place even very close to the sea surface. During this time of year the average ocean surface temperature in the Bedford Basin is around 10℃ (Shi & Wallace, 2018). During the source event the probe temperature starts at ~10℃ only 24 hours before reaching a minimum of ~-7.5℃.

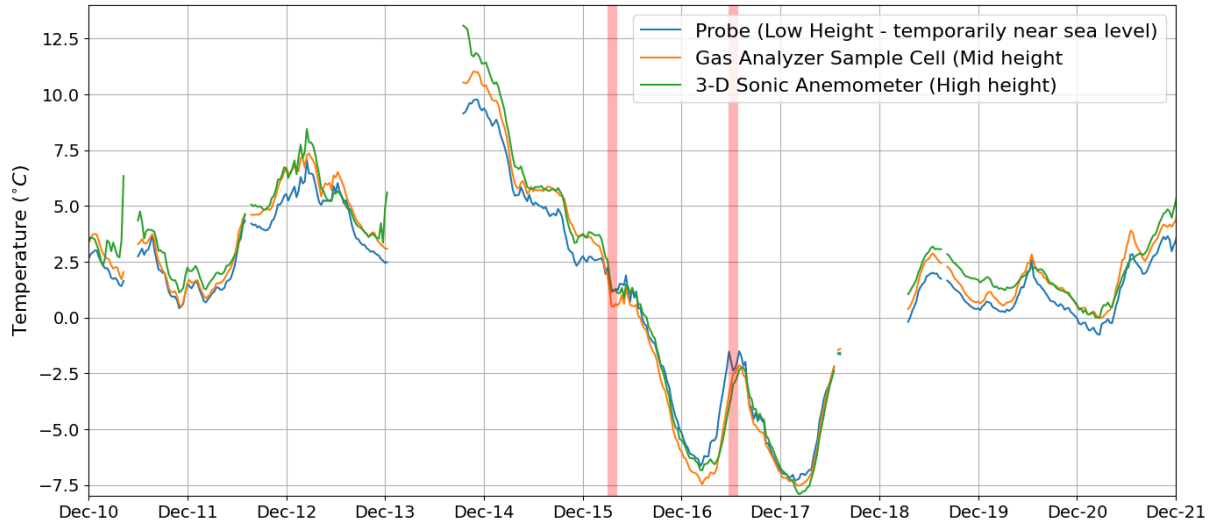

Temperature probe (blue), sample cell (orange) and 3-D sonic (green) are compared. Red lines show when the probe is thought to have fallen from its mounting at 7:00 am on December 15th and when the probe was retrieved from near the water surface (during low tide) at 12:30 pm on December 16th.

Photo from December 16th at 1:05 pm, sunny mid-day, in between the two main flux peaks in the N_2O source event. A temperature probe was originally mounted at the end of the 2x4' plank with approximately 1.8 meters of slack on the cable. It is thought to have been knocked from the mounting by the floating fence bobbing in the water. High tides reached 1.57 m below the jetty during this time. The probe likely experienced sea spray after it came loose and dangled near the water surface at 7:00 am on December 15th. At 12:30 pm on December 15th the probe was pulled up, its functioning inspected, and taped back on the 2x4' and later fixed more permanently at 2:30 pm on December 18th.

E. Note on L and potential virtual temperature

Regarding the L and T(z) formulas which are dealing with different temperature measures in the various calculations. In the strict definition of L, the temperature is a "potential virtual temperature", which we assume is reasonably well represented by the "acoustic temperature" (from the sonic). These are both different from the standard air temperature (maybe a few degrees). So, there were several temperatures to choose for FTIR retrieval input along with the option to correct the acoustic temperature using our H_2O concentration measurement. I opted to follow the method of Flesch et al. (2016)

which uses the acoustic temperature, Ts, uncorrected. I did some testing and a symmetrical temperature offset of 2℃ (top and bottom values offset in the same direction), i.e., a calibration offset between different instruments, had negligible effect on the retrieved concentration gradient. It is worth exploring if correcting Ts for water vapour improves the retrieval quality though this would have required more equipment that was not available for our experiment. We only had water concentration measurements from the retrieval process itself and an iterative analysis would have used too much computing time. If the CPEC200 eddy covariance kit is used in the future the gas capsules for zero and span may be a useful addition so that the entire kit is operational allowing for H_2O concentration measurements. However, that is only at one height in which case the correction would likely be cancelled out in the retrieved concentration difference.